

Syracuse University

SURFACE

Dissertations - ALL

SURFACE

8-2014

Rigidity and Fluidity in Living and Nonliving Matter

Jorge Hernan Lopez
Syracuse University

Follow this and additional works at: <https://surface.syr.edu/etd>



Part of the [Physics Commons](#)

Recommended Citation

Lopez, Jorge Hernan, "Rigidity and Fluidity in Living and Nonliving Matter" (2014). *Dissertations - ALL*. 157.

<https://surface.syr.edu/etd/157>

This Dissertation is brought to you for free and open access by the SURFACE at SURFACE. It has been accepted for inclusion in Dissertations - ALL by an authorized administrator of SURFACE. For more information, please contact surface@syr.edu.

Abstract

Many of the standard equilibrium statistical mechanics techniques do not readily apply to nonequilibrium phase transitions such as the fluid-to-disordered solid transition found in repulsive particulate systems. Examples of repulsive particulate systems are sand grains and colloids. The first part of this thesis contributes to methods beyond equilibrium statistical mechanics to ultimately understand the nature of the fluid-to-disordered solid transition, or jamming, from a microscopic basis.

In Chapter 2 we revisit the concept of minimal rigidity as applied to frictionless, repulsive soft sphere packings in two dimensions with the introduction of the jamming graph. Minimal rigidity is a purely combinatorial property encoded via Laman's theorem in two dimensions. It constrains the global, average coordination number of the graph, for instance. Minimal rigidity, however, does not address the geometry of local mechanical stability. The jamming graph contains both properties of global mechanical stability at the onset of jamming and local mechanical stability. We demonstrate how jamming graphs can be constructed using local rules via the Henneberg construction such that these graphs are of the constraint percolation type, where percolation is the study of connected structures in disordered networks. We then probe how jamming graphs destabilize, or become fluid-like, by deleting an edge/contact in the graph and computing the resulting rigid cluster distribution. We also uncover a new potentially diverging lengthscale associated with the random deletion of contacts.

In Chapter 3 we study several constraint percolation models, such as k -core percolation and counter-balance percolation, on hyperbolic lattices to better understand the role of loops in such models. The constraints in these percolation models incorporate aspects of local mechanical rigidity found in jammed systems. The expectation is that since these models are indeed easier to analyze than the more complicated problem of jamming, we will gain insight into which constraints affect the nature of the jamming transition and which do not. We find that $k = 3$ -core percolation on the hyperbolic lattice remains a continuous phase transition despite the fact that the loop structure of hyperbolic lattices is different from Euclidean lattices. We also contribute towards numerical techniques for analyzing percolation on hyperbolic lattices.

In Chapters 4 and 5 we turn to living matter, which is also nonequilibrium in a very local way in that each constituent has its own internal energy supply. In Chapter 4 we study the fluidity of a cell moving through a confluent tissue, i.e. a group of cells with no gaps between them, via T1 transitions. A T1 transition allows for an edge swap so that a cell can come into contact with new neighbors. Cell migration is then generated by a sequence of such swaps. In a simple four cell system we compute the energy barriers associated with this transition. We then find that the energy barriers in a larger system are rather similar to the four cell case. The many cell case, however, more easily allows for the collection of statistics of these energy barriers given the disordered packings of cell observed in experiments. We find that the energy barriers are exponentially distributed. Such a finding implies that glassy dynamics is possible in a confluent tissue.

Finally, in chapter 5 we turn to single cell migration in the extracellular matrix, another native environment of a cell. Experiments suggest that the migration of some cells in the three-dimensional extra cellular matrix bears strong resemblance to one-dimensional cell migration. Motivated by this observation, we construct and study a minimal one-dimensional model cell made of two beads and an active spring moving along a rigid track. The active spring models the stress fibers with their myosin-driven contractility and alpha-actinin-driven extendability, while the friction coefficients of the two beads describe the catch/slip bond behavior of the integrins in focal adhesions. Net motion arises from an interplay between active contractility (and passive extendability) of the stress fibers and an asymmetry between the front and back of the cell due to catch bond behavior of integrins at the front of the cell and slip bond behavior of integrins at the back. We obtain reasonable cell speeds with independently estimated parameters. Our model highlights the role of alpha-actinin in three-dimensional cell motility and does not require Arp2/3 actin filament nucleation for net motion.

Rigidity and Fluidity in Living and Nonliving Matter

by

Jorge H. Lopez

B.S. Universidad de Antioquia, Colombia 2003

M.S. Universidad Nacional de Colombia, 2007

DISSERTATION

Submitted in partial fulfillment of the requirements for the
degree of Doctor of Philosophy in Physics
in the Graduate School of Syracuse University

August 2014

Copyright 2014 Jorge H. Lopez

All rights reserved

Dedication

To my parents, Gustavo and Maria Eugenia. To my brother, David, and my sister,
Lina.

Acknowledgements

I want to thank to Jennifer Schwarz by her tremendous encouragement in this journey, her constant support and time dedication. Her energy and passion are an example. I thank to the rest of my committee, Profs. Cristian Armendariz-Picon, Thomas P. Fondy, Matthew LaHaye, M. Lisa Manning, and Liviu Movileanu. And most importantly, I want to thank to my Lord and savior Jesus Christ who transformed my life and gave me a vision in this city of Syracuse.

Contents

1	Introduction	1
1.1	Jamming	3
1.2	Constraint counting	6
1.3	Percolation	9
1.4	Constraint percolation	12
1.5	Hyperbolic Geometry	14
1.6	Glassy dynamics and cell motility	17
1.7	Nonglassy dynamics and cell motility	21
2	Jamming graphs: A local approach to global mechanical rigidity	27
2.1	Contact geometry of frictionless, repulsive soft spheres at the onset of rigidity	30
2.2	Algorithm for building jamming graphs	33
2.2.1	Henneberg construction	33
2.2.2	Hilbert stability	35
2.2.3	Pseudocode	35
2.3	Perturbing jamming graphs	40
2.3.1	One random bond deletion	40
2.3.2	Hyperstatic: Randomly adding and deleting more than one bond	48
2.4	Discussion	51

3	Constraint Percolation on Hyperbolic lattices	55
3.1	Introduction	55
3.2	Model and methods	57
3.3	Theoretical proof of $p_c < 1$ for some hyperbolic tilings	60
3.4	Results	64
3.4.1	Crossing probability	65
3.4.2	Order Parameter	67
3.4.3	Cluster sizes	69
3.4.4	Culling time	71
3.4.5	Debate about p_u	72
3.5	Discussion	75
4	Cell motion in densely packed tissues	78
4.1	Introduction	78
4.2	Model and Methods	80
4.3	Results	84
4.3.1	$N = 4$ cells	84
4.3.2	Many cells	89
4.4	Discussion	92
5	Active elastic dimers: Cells crawling along rigid tracks	97
5.1	A minimal model	100
5.1.1	Stress fibers as active springs with two equilibrium lengths	101
5.1.2	Focal adhesions provide an elastic friction	105
5.1.3	Equations of motion	106
5.2	Estimation of parameters	106
5.2.1	Active spring parameters	107
5.2.2	Friction parameters	108
5.3	Results	110

CONTENTS	x
5.4 Discussion	118
6 Future directions	122
Bibliography	124

List of Figures

1.1	Photoelastic image of a disordered disk packing. The intensity of the light indicates the strength of the forces between the disks. Image from Ref. 2.	4
1.2	(a) The simplest Laman graph. (b) The second simplest Laman graph. (c) The graph is not Laman. The square can be deformed with no cost in energy (distances between points remains fixed but shape does not).	8
1.3	(a) Each color denotes a cluster. The boundary conditions are fixed. The yellow cluster percolates the system. (b) Clusters on a square lattice of a much larger size. The aqua-colored cluster spans the system.	10
1.4	For the square lattice (red dashed curve), P_∞ , the probability that a bond is in the spanning cluster, scales as $(p - 0.5)^{5/36}$ just above the transition and for the Bethe lattice with $z = 3$ (blue solid curve) P_∞ scales as $(p - 0.5)$ just above the transition. It is just coincidence that the transition probability is the same ($p = 0.5$) for these two types of lattices.	11
1.5	A Bethe lattice with $z = 3$, where z is the coordination number. Note the absence of loops. The numbers indicate the level, or layer, number.	12

1.6	An example k -core culling for $k = 3$ on the square lattice. Each picture represents one iteration of the culling process. For this particular initial configuration, nothing remains. This is because no finite k -core clusters can exist for this particular lattice and value of k . Therefore $p_c = 1$ for 3 - core on the square lattice.	13
1.7	Euclidean tessellations of the plane.	15
1.8	(a) A $\{4, 7\}$ hyperbolic tessellation. (b) A $\{7, 4\}$ hyperbolic tessellation.	16
1.9	The famous bat picture drawn by M. C. Escher.	17
1.10	A typical trajectory of a colloidal particle at 56 percent packing fraction for 100 minutes. The colloids spend most of their time confined in cages formed by their neighbors and moved significant distances only during quick, rare cage rearrangements. Image from Ref. 31.	18
1.11	Simplified depiction of energy barriers in state space.	19
1.12	MCDK cells within a confluent monolayer. The scale bar is 100 microns. Image from Ref. 35.	20
1.13	Depiction of a T1 transition in a model confluent tissue.	21
1.14	Birdseye view of cell motion. Both cells are moving upwards. (a) Fluorescence image of keratocyte cell. Image from Ref. 42. (b) Confocal reflection contrast image of a MV3 melanoma cell. The scale bar is 18 microns. Image from Ref. 136.	22
1.15	Side-view schematic of a cell crawling on a surface.	23
1.16	(a) Schematic of an actin filament. The diameter of a single actin monomer is roughly 5.4 nm. (b) A schematic of a cell interacting with a surface via focal adhesions with the integrins denoted in red. (c) A schematic of a sarcomere, the unit that is repeated in striated muscle. The length of a sarcomere is typically 2 microns.	26

2.1	A jammed, bidisperse (i.e. with two different radius) particle packing with $N = 1024$ and packing fraction $\phi = 0.841$. The colors denote the local coordination number, z , with light blue denoting $z = 0$, magenta denoting $z = 3$, red denoting $z = 4$, blue denoting $z = 5$, orange depicting $z = 6$, and purple denoting $z = 7$, which is possible for the 1.4 diameter ratio for the bidisperse system.	31
2.2	(a) The center particle is not mechanically stable (for the other two particles fixed). (b) The center particle is mechanically stable.	32
2.3	(i) Graph before Henneberg step. (ii) Type I step with the new bonds denoted with dashed lines. (iii) Type II step.	34
2.4	Illustration for checking if a particle enclosed by a triangle.	35
2.5	Left: An uncounter-balanced vertex p with at least three neighbors n_1, n_2, n_3 , is counter-balanced by creating bond \overline{px} and deleting bond $\overline{pn_3}$. Likewise, x is counter-balanced by finding z such that x is inside triangle $\triangle zpn_3$, consequently creating bond \overline{xz} . Right: An illustration of different positions to choose an appropriate neighbor x for uncounter-balanced vertex p . Values of β are chosen so that most of the space contained in the angle determined by vectors $\overrightarrow{pn_1}$ and $\overrightarrow{pn_2}$ is scanned.	37
2.6	Uncounter-balanced vertex p is counter-balanced by finding two connected vertices a and b such that the creation of vertex x and bonds $\overline{xp}, \overline{xa}$, and \overline{xb} causes x to be counter-balanced. Also, bond \overline{ab} is deleted.	38
2.7	Left: Many small rigid clusters identified via color after the deletion of one bond/contact, namely the bond between vertices 1 and 41 as numbered. The black dashed lines indicate bonds that are not rigid with respect to any other bond. Right: A “macroscopic” rigid cluster (in blue) along with a few small ones after the deletion of the bond connecting vertices 12 and 30.	41

2.8	Plot of $Prob(s)$, the probability for a bond to participate in a rigid cluster of size s after one bond is deleted from the jamming graph. The different graphs represent different system sizes.	43
2.9	Plot of the peak area for the macroscopic rigid cluster sizes, $a^\#$, as a function of N initial vertices. The dashed line is merely a guide for the eye.	44
2.10	Example graph where removal of the red, dashed line leads to all remaining bonds not rigid with respect to each other (case (1) in page 42). The removal of any one blue line affects only its neighboring blue bond. The rest of the graph is unaffected (case (2) in page 42). The three black circles denote repetition of the blue hinge bonds.	45
2.11	Plot of $Prob(s)$, the probability for a bond to participate in a rigid cluster of size s after one bond is deleted from the minimally rigid graphs generated by Henneberg Type I moves only. The different graphs represent different system sizes.	47
2.12	Plot of $Prob(z)$, the probability for a site to have z neighbors, for the jamming graphs (left) and the graphs generated using Henneberg Type I moves (right). For both plots, $N = 40$	47
2.13	Plot of $Prob(s)$, the probability for a bond to participate in a rigid cluster of size s after A bonds are randomly added to the jamming graph and then D bonds are randomly deleted. Two different system sizes are shown.	50
2.14	Left: Plot of the gap size $s^\#$ as a function of N for fixed $\epsilon = \frac{A}{N}$. Right: Plot of $s^\#$ as a function of ϵ for different system sizes. The inset is a finite-scaling scaling collapse obtained with $\nu = \frac{1}{3}$ and $\rho = \frac{1}{2}$. All dashed lines are guides for the eye.	51
3.1	$\{3, 7\}$ tessellation on the Poincare disk.	58
3.2	$\{3, 7\}$ tessellation on the Poincare disk with the four boundary regions.	60

3.3	Impossibility of building a tree of connectivity $z = 6$ on the $\{3, 8\}$ tessellation due to the lack of space	61
3.4	Tessellation $\{4, 8\}$ enables the construction of trees of connectivity $z = 6$	62
3.5	Tree construction on the hyperbolic tessellations	63
3.6	Illustration of all the possible cases of occupation for a 4-core cluster on a tree of connectivity $z = 5$	64
3.7	Crossing probability on $\{3, 7\}$ tessellation and different percolation models. counter-balance model apparently is discontinuous which is confirmed by the extrapolating the value of the slope with $1/l$	66
3.8	Inverse slope of Crossing probability, $1/M$, tendency on $1/l$ for different models on the $\{3, 7\}$ lattice. For 1-core model $1/M$ tends to 0.240, for 2-core to 223, for 3-core to 0.131, and for counter-balance (CB) to -0.036 indicating M is tending to ∞ as l tends to ∞	67
3.9	The order parameter for the different models on the $\{3, 7\}$ lattice. . .	68
3.10	The inverse of the maximum slope of the order parameter as a function of ℓ for the different models on the $\{3, 7\}$ lattice.	69
3.11	Cluster size histograms (as opposed to distributions) for different models and the $\{3, 7\}$ lattice. 10000 samples were implemented for each data set.	70
3.12	Culling time for the different constraint percolation models for the $\{3, 7\}$ lattice. Each data set was averaged over 50,000 samples.	72
3.13	Ratio $S2/S1$ for different models and for Tessellation $\{3, 7\}$	73
3.14	Crossing Probability results for different models and for Tessellation $\{3, 7\}$	75
4.1	Illustration of an active T1 transition in a model confluent tissue. Cells $E1$ and $E2$ share an edge before the transition and become disjointed after the transition, while $S1$ and $S2$ are disjointed before the transition and share an edge after the transition.	83

4.2	(a) The initial $N = 4$ cell configuration. (b) The length of the center horizontal edge (colored green) decreases. (c) The $N = 4$ cell configuration after the active T1 transition is applied, and the now vertical center edge is expanded.	85
4.3	The total energy of the $N = 4$ cell system with $p_0 = 3.0$. The energy barrier is denoted by $\Delta\varepsilon$. Points A and B correspond to Fig. 4.2(a) and Fig. 4.2(b) respectively. The negative lengths correspond to before the T1 transition and the positive correspond to after.	86
4.4	The energy barrier as a function of p_0 ranging from 3 to 4 varying the number of refinements, NR . In Surface Evolver, each refinement bisects an edge to double the number of vertices. There is a rigid-to-fluid transition (the vanishing of the energy barrier) around $p_0 = 3.72$	87
4.5	Schematic for quantities used in the analytical calculation. The quantity S is the area of the triangle enclosing it.	88
4.6	(a) Energy trace for active T1 transition for $p_0 = 3$ from the analytical calculation. (b) Energy barrier as a function of p_0 from the analytical calculation.	88
4.7	Schematic depicting the parameter x used in the calculation. The blue circles denote added vertices that are pinned before the active T1 transition.	89
4.8	Energy barrier traces for different x s for $p_0 = 3.0$	90
4.9	(a) Energy barrier as a function of x for different numbers of refinements (NR) and (b) for different precision levels for the energy (SE). The precision level is set to 10^{-5} unless stated otherwise.	91
4.10	$\Delta\varepsilon$ for $p_0 = 3$, $\kappa = 1$ for all four cells and different γ_1 for the migrating cell (initially the leftmost cell), where γ_1 is a dimensionless parameter multiplying the area term in the energy.	92

4.11	An $N = 64$ amorphous, confluent cell packing. See. Ref. 39.	93
4.12	Typical energy barrier traces from the $N = 64$ cell simulation. The EB stands for energy barrier. (a) After the active T1 transition, without extra relaxation of the edges by unpinning blue vertices, the energy is a global minimum. (b) After the active T1 transition, the energy does reach a local minimum, but after edge relaxation to black vertices, can reach a global minimum. (c) The energy continues to rise after the active T1 transition, without relaxation, no energy barrier is observed. With relaxation of all the edges in the system, a lower energy state can be found. So the energy barrier required for the active T1 transition is higher than the energy required to the perform the active T1 transition, which means the transition will not occur. See Ref. 39.	94
4.13	(a) The average $\Delta\varepsilon$ as a function of p_0 for different κ s. The circle and the diamond denote the perimeters of a circle and a circle respectively (both with area fixed at unity). (b) The average energy barrier dependence on κ is simple and can be scaled out. (c) The distribution of energy barriers in active T1 transistions. (d) The rigid-to-fluid transition in the $N = 64$ cell system. See Ref. 39. Also note that $\bar{\Delta\varepsilon} = \varepsilon_0$	95
5.1	Side-view schematic of a two-bead-spring model of a cell crawling along a narrow track.	100
5.2	Schematic of contractile units in a stress fiber in extended mode (top) and contracted mode (bottom). The blue filaments represent actin filaments, red rectangles, alpha-actinin, and the green shapes, myosin minifilaments. For simplicity, we have not shown any contractile units in parallel, only three units in series.	104

5.3	Left (a): Plot of the equilibrium spring length x_{eq} as a function of $x_1 - x_2$. Right (b): Plot of friction coefficient γ_1 as a function of $x_1 - x_2$. The parameters used are listed in Table I.	107
5.4	(a) Plot of cell length $x = x_1 - x_2$ as a function of time for the parameters given in Table I. (b) Plot of position of the center of mass, x_{cm} , as a function of time. (c) Plot of velocity of the center of mass, v_{cm} , as a function of time.	114
5.5	Left: Plot of center of mass for cell as a function of time for different spring constants k . The parameters are from Table I (unless stated otherwise).	115
5.6	Left: Plot of $\bar{v}_{cm}(w)$. Left Inset: Plot of $x_{cm}(t)$ for different widths. Right: Plot of $\bar{v}_{cm}(h)$ for $w = 0.5 \mu m$. Right Inset: Plot of $x_{cm}(t)$ for different heights of hysteresis loop.	116
5.7	Left: Plot of $x_{cm}(t)$ for different friction coefficients. Right: Plot of $\bar{v}_{cm}(\gamma_{11})$	116
5.8	Plot of $x_{cm}(t)$ for different values of the noise with $A = A_1 = A_2$	117
5.9	Plot of $\langle v_{cm} \rangle (A)$ for finite slope case with a slope of 5/2. Inset: Plot of $\langle x_{cm} \rangle (t)$ for $A = 0$ and $A = 0.01 nN^2s$	118

Chapter 1

Introduction

It is the job of a condensed matter physicist to identify and classify the various phases of matter that are more dense than gases (hence “condensed”) and the associated transitions between them. The prominent theoretical machinery used to accomplish this mission has been equilibrium statistical mechanics, which provides a probabilistic framework to interpolate between the microscopic description of interactions between particles and the average macroscopic behavior of a large collection of such particles [1]. In more recent years, the condensed matter physicist’s mission has extended beyond equilibrium systems to include non-equilibrium systems, where the machinery of equilibrium statistical mechanics does not readily apply. An example of such a system is a disordered granular solid—yes, an amorphous packing of sand that resists compression when compressed. (Amorphous here means the lack of any orientational order that one finds in a crystalline solid.) Given the energy scales in the system, the temperature is effectively zero so that thermal averaging over all possible states of the system, as is done in equilibrium statistical mechanics, is not possible. In even more recent years, the definition of condensed matter has widened yet again to include matter in which energy is inputted at the level of individual particles, or active matter, to drive the system out of equilibrium. The expectation is that active matter describes living systems, such as a collection of cells each with its own internal

energy, or a collection of motors within a cells each with their own internal energy.

So the “to-do” list of a condensed matter physicist has certainly grown in recent years from equilibrium systems to nonequilibrium systems to systems driven out of equilibrium at the local level, or active systems to describe living matter amongst other things. And while the list of systems in question has grown, the machinery used to analyze such systems has not grown as readily. This thesis documents several new theoretical approaches to characterize the phase transition between a fluid and a mechanically rigid amorphous state (or solid), otherwise known as a jammed state at zero temperature. This zero-temperature *jamming* transition is a hallmark example of a non-equilibrium transition since, again, the system lacks the thermal averaging which is at the heart of equilibrium statistical mechanics, but is certainly in need of averaging due to the many possible disordered arrangements of packings. In Chapter 2, I introduce the notion of a jamming graph—a graph that captures the connectivity of a disordered granular packing at the boundary of this transition. In Chapter 3, I develop techniques to analyze phase transitions in constraint percolation in hyperbolic geometries, which will turn out to be minimal models of jamming. Discussion of these approaches in Chapters 2 and 3 constitute the nonliving matter aspect of this thesis. In Chapters 3 and 4, I turn to analysis of rigidity and fluidity in living matter. If one considers a monolayer of foam that is confluent -i.e. no gaps between the bubbles-, the bubbles cannot move (unless enough external force is supplied). In a living system, however, such as a monolayer of epithelial cells, the cells can shape change due to internal processing. One can then look for potential fluidity of an individual cell in a dense medium of surrounding cells, which is a native environment for a crawling cell. In Chapter 4, I introduce a new model for a single cell moving in another native environment, namely the extracellular matrix. The collectivity in this model is at the level of molecular motors, namely myosin, that act to bring about an active rigidity, which coupled with an asymmetry, can lead to motion of a cell along a fiber of the extra-cellular matrix.

Given the range of topics presented in this thesis, I will use the introduction to discuss the necessary background and terminology for each subsequent chapter. This should help the reader appreciate the consequences of my results. Do not hesitate to return to the introduction when going through the meat of the thesis to remind yourself of various concepts.

1.1 Jamming

Let us begin with sand. Sand is a notoriously difficult material to understand. Even though the grains are of millimeter size, visible to the naked eye, it is not immediately obvious as to whether sand will behave like a solid and resist compression or behave like liquid and flow as a result of some perturbation. In both the rigid and the fluid phases, the sand grains are arranged in a disordered (amorphous) arrangement, unlike a crystalline solid, where there are symmetry transformation from one grain (atom) to another. Figure 1.1 depicts an amorphous packing of deformable disks (model sand grains) [2]. To determine whether or not the sand is a solid or a liquid, one can perturb it. Take for example sand on an inclining plane. As you tilt the incline of the plane (the perturbation), sand will eventually begin to flow, but it will only be some fraction of the sand furthest away from the plane (the “top” layers). So there is still no clear cut answer in this experiment as to the phase of sand.

Perhaps a more clear cut answer emerges when considering the following parameter, the density, or packing fraction, of sand. When sand is loosely packed, it behaves as a liquid, flowing in response to applied shear. When sand is more densely packed, it behaves as a solid with some non-zero shear modulus even in the long time limit. One might say that there is a phase transition from a fluid to a solid as the packing fraction of sand (to air) increases. Since this granular system is effectively zero-temperature, how does one construct an ensemble of various possible states given the many possible amorphous arrangements? Well, there exist ideas about extending statistical

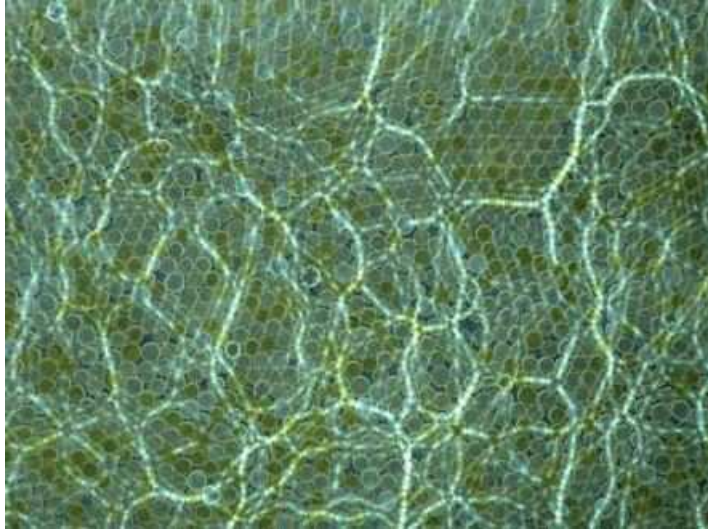


Figure 1.1: Photoelastic image of a disordered disk packing. The intensity of the light indicates the strength of the forces between the disks. Image from Ref. 2.

mechanics to collections of sand grains and colloids and other granular-like materials via an effective temperature [3]. We will not address these here as debate still rages on about them.

One can instead take a more straightforward approach and develop a simulation to study this fluid to amorphous solid transition, which is called the jamming transition. With such a simulation, one can study properties of the transition and perhaps be inspired to develop a theoretical model that captures the properties of the transition. To give you a concrete example of such a simulation, over the past twenty years or so, scientists have been simulating sand grains and foams and colloids as purely repulsive soft spheres [4, 5, 6]. The purely repulsive potential is of the form

$$V(r_{ij}) = \frac{\varepsilon}{\alpha}(1 - r_{ij}/\sigma_{ij})^\alpha \text{ for } r_{ij} \leq \sigma_{ij}; \quad V(r_{ij}) = 0 \text{ for } r_{ij} > \sigma_{ij}, \quad (1.1)$$

where ε is the characteristic energy scale of the interaction, r_{ij} is the distance between centers of the particles i and j , and σ_{ij} is the sum of the radii of i and j particles. The α parameter determines the type of potential used. The most common values studied are the repulsive harmonic potential for $\alpha = 2$, the nonlinear spring for $\alpha = 3/2$

which is harder than harmonic potential, and the repulsive Hertzian potential for $\alpha = 5/2$. The Hertzian potential captures the interaction between sand grains [7]. Also the spring potential has been reported for the interaction between bubbles [8]. It is important to note that when particles do not overlap ($r_{ij} \geq \sigma_{ij}$) the potential is zero for all the cases.

If you randomly place N such particles in a box with periodic boundary conditions and locate the nearest energy minimum via your favorite minimization routine, there is indeed a packing fraction below which the infinite-time shear modulus vanishes and above which it does not, i.e. a jamming transition [9, 10, 11]. When viewed from the context of phase transitions in equilibrium systems, the transition is a bit strange in that it possesses aspects of continuous phase transitions and aspects of discontinuous phase transitions. In equilibrium phase transitions, the system is either one or the other. What are continuous phase transitions and discontinuous phase transitions? Both types of transitions are indicated by an order parameter—a measure that is zero in one phase and non-zero in the other—that goes from zero to non-zero continuously or discontinuously as some tuning parameter is changed.

As for differences, it turns out that continuous phase transitions are characterized by a set of critical exponents, i.e. a universality class. Near the transition, several physical quantities, such as the order parameter, the free energy, specific heat, a correlation length, and others depending on the system; are described as power-law expressions of the reduced tuning parameter $\tau = (T - T_c)/T_c$, for $\tau \ll 1$. In other words, a physical quantity χ , is expressed as $\chi(r) \sim r^\nu$ for r tending to 0. Here ν is called the critical exponent associated with χ . One of the most important parameters to describe the physical behavior close to a critical point is the correlation length, ξ . The correlation length indicates how far microscopic particles of the system are correlated. Accordingly, a particle will be physically related with the particles that are at distance less than ξ . ξ is then a measure of the order of the system. At the transition, the correlation length diverges.

Discontinuous phase transitions, on the other hand, are driven by nucleation. Think back to the van der Waals equation and the gas-to-liquid phase transition analysis. There is no diverging length scale. A typical length scale is set by the critical size of the nucleation bubble. Once a bubble of one phase becomes large enough, that phase will dominate the system.

If one regards the average number of contacts $\langle Z \rangle$ in a system of purely repulsive soft spheres as the order parameter, then in the fluid phase $\langle Z \rangle = 0$ and in the rigid phase $\langle Z \rangle > 0$. It turns out that this order jumps discontinuously from zero to > 0 at the transition, suggesting a discontinuous transition [5, 6]. Simulations, however, indicate a diverging correlation length, which would point to a continuous transition [5, 6]. Much effort has been put into numerical measurements of such exponents with the hope that we would understand the nature of the jamming transition from a microscopic level. This knowledge would then help us ultimately understand experiments with sand and other athermal, disordered particle systems. Not only have we failed in this task, arguments have been brewing over the existence of a linear regime in such systems, etc. [12, 13]. In other words, I think that the nature of the complications of even this simplified repulsive soft sphere system have at least become more clear over the years.

So while I will not delve into the complications for the sake of brevity, let us take a step back from the problem and go back to the time of Maxwell, yes, *the* Maxwell, who thought about the nature of forces in sand piles among other things.

1.2 Constraint counting

To understand how a disordered network of springs, or a frame, becomes rigid, Maxwell estimated how many springs would one need to constrain the system such that all independent motions of the individual joints (between springs), each under some given external force, are frozen out, i.e. become rigid with respect to each

other [14]. In other words, Maxwell correctly pointed out that a system with more degrees of freedom than those necessary to constraint local rotations and translations is able to "flow" in some way. Therefore, a "fluid" of joints becomes a "solid" when its joints are constrained enough to constrain all the degrees of freedom (except for global translations and rotations). Accordingly, a system of N joints in d dimensions has Nd degrees of freedom as one joint has d degrees of freedom in space. So when the number of constraints, is $dN - d(d + 1)/2$, where the second term represents the number of global (trivial) translations and rotations, the system is at the rigidity boundary. To understand the second global contribution, a two-dimensional system has 3 global degrees of freedom, two corresponding to the translation of all objects in the network and one more for rotations. In three dimensions, there are 6 global degrees of freedom, 3 account for translations and 3 more for rotations. In general, it can be shown that for a joint in d dimensions it will have $d(d + 1)/2$ global degrees of freedom, corresponding to d translations and $d(d - 1)/2$ rotations.

How does one determine the number of constraints on a joint? The number of constraint of a joint is determined by its neighboring springs. If $\langle Z \rangle$ is the average number of springs per joint then the entire amorphous spring network contains $\frac{N \langle Z \rangle}{2}$ constraints. The $1/2$ factor comes from the fact that each spring is counted twice, as it is shared by two joints. Consequently, the system is at the boundary of the fluid-rigid transition when $Nd = \frac{N \langle Z \rangle}{2}$, that is when the average coordination number satisfies $\langle Z \rangle = 2d$. Notice that we have neglected the global translations and rotations as the number is negligible for $N \gg 1$. When $\langle Z \rangle < 2d$, the system is a fluid, i.e. not rigid.

Maxwell constraint counting approach was put on more rigorous footing more than one hundred years later by Laman [15]. Maxwell assumed that each degree of freedom was not spatially correlated with another. Is this assumption valid? It turns out not to be in several explicit examples where Maxwell constraint counting would incorrectly imply a rigid graph. To address this short-coming, Laman constructed a

two-dimensional graph that is minimally rigid, which means that the graph is rigid in that there is only one rigid cluster. The removal of just one edge results in at least two rigid clusters so that the graph is not rigid as a whole. Minimally rigid graphs satisfy precisely the Maxwell constraint counting including the trivial rotations and translations degrees of freedom. Therefore, the number of edges is exactly $2N - 3$, where N is the number of vertices, as we demand the number of constraints be equal to the number of degrees of freedom $2N$ minus the trivial translations and rotations, that is 3. But then Laman went on further to investigate the minimal rigidity of all subgraphs, which is why minimally rigid graphs in two dimensions are called Laman graphs. Explicitly, Laman stated that a graph with N vertices is minimally rigid if and only if, for all l , every l -vertex subgraph has at most $2l-3$ edges, and the whole graph has exactly $2N-3$ edges. Some examples of the simplest Laman graphs are given in Fig. 1.2, as well as an example of a graph that is not Laman.

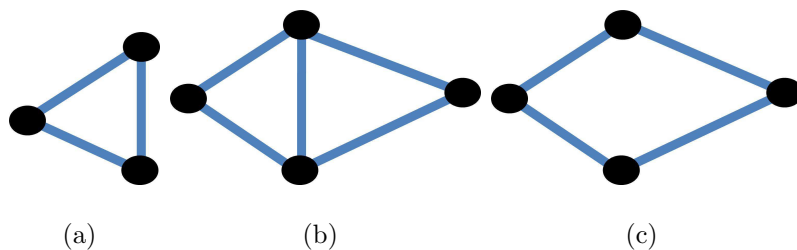


Figure 1.2: (a) The simplest Laman graph. (b) The second simplest Laman graph. (c) The graph is not Laman. The square can be deformed with no cost in energy (distances between points remains fixed but shape does not).

In chapter 2 we are going to extract the rigid clusters of a flexible graph. To determine the rigid clusters, I use the practical algorithm called the *pebble game*. The pebble game [16] is a mathematical game that uses *pebbles* that are moved on a directed graph, i.e. a graph where direction is assigned to its edges. The pebbles go over the vertices of the graph according to some rules, and depending on the final result it can be told if the graph is minimally rigid or not. Also by this algorithm it

can be determined overconstrained regions that bear stress and rigid components of the graph that do not bear stress.

While Laman's approach holds in two dimensions, it applies to systems with fixed connectivity, such as spring networks. To begin to deal with purely repulsive particles, we introduce the *jamming graph*. In a particle system, unlike a bar-joint network, the particles can come in and out of contact, i.e. the connectivity is not fixed. And in mechanically stable packings for purely repulsive particles, each particle must be locally mechanically stable. This local mechanical stability criterion in two dimensions, turns out to be the property that each particle must be enclosed in a triangle by at least three of its contacting particles. The jamming graph incorporates both Laman's nonlocal, or global, minimal rigidity criterion *and* local mechanical stability. It is presented in Chapter 2 of the thesis and has been published in Physical Review E last year [17]

1.3 Percolation

Given the complicated nature of jamming, let us take a step back and consider the simplest phase transition in a disordered system, namely *percolation*. The standard percolation model can be stated in this way: Given a lattice, occupy each site independently and at random with occupation probability p . Since p is a probability, $0 \leq p \leq 1$. When $p = 0$, the lattice is empty, i.e. no occupied sites. When $p = 1$, the lattice is fully occupied. As p is increased from zero, clusters start to emerge (see Fig. 1.3(a)). Two neighboring occupied sites on the lattice are part of the same cluster. In other words, neighboring occupied sites form clusters where any occupied site in the cluster can be reached from any other occupied site in the cluster through a series of neighboring occupied sites. As p grows these clusters grow in size. A cluster is called percolating if it spans the lattice in any direction. For example, in Figs. 1.3(a) and 1.3(b) there is a percolating cluster.

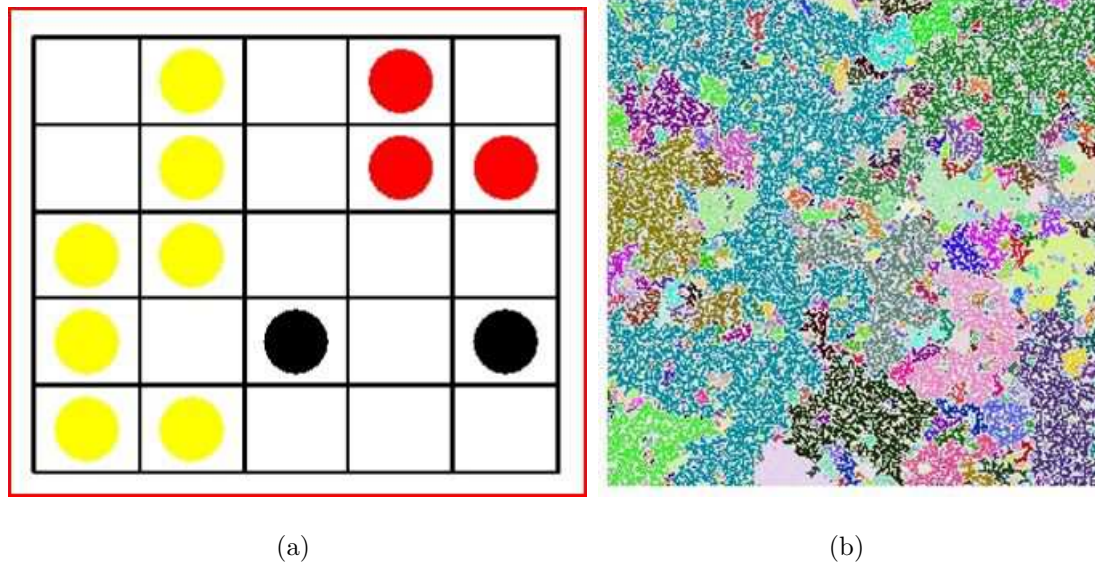


Figure 1.3: (a) Each color denotes a cluster. The boundary conditions are fixed. The yellow cluster percolates the system. (b) Clusters on a square lattice of a much larger size. The aqua-colored cluster spans the system.

It has been shown that there exists a critical probability p_c such that for $p < p_c$ there is no percolating cluster and for $p > p_c$ there is always such type of cluster. What happens at $p = p_c$ is actually a phase transition between the state of not having a percolating cluster and the state of having one that percolates the lattice. So tuning the occupation probability allows one to go from a system with no spanning (or percolating) cluster, which is one phase, to a system with a percolating cluster, which is another phase, such that a phase transition in the connectivity has occurred. In other words, the tuning parameter for this system is the occupation probability. In addition to a tuning parameter, one also defines an order parameter, as mentioned previously. A convenient order parameter is zero in one phase and non-zero in the other. The typical order parameter for percolation is the probability that an occupied site is part of the spanning cluster, P_∞ . In the non-percolating phase, $P_\infty = 0$ because there is no spanning cluster. Even at the transition, $P_\infty = 0$ since it so happens that

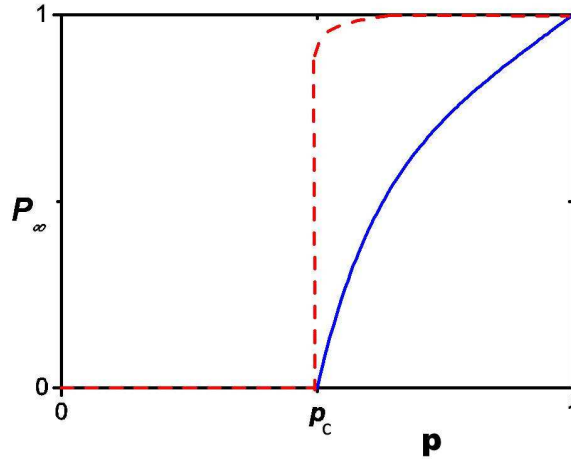


Figure 1.4: For the square lattice (red dashed curve), P_∞ , the probability that a bond is in the spanning cluster, scales as $(p - 0.5)^{5/36}$ just above the transition and for the Bethe lattice with $z = 3$ (blue solid curve) P_∞ scales as $(p - 0.5)$ just above the transition. It is just coincidence that the transition probability is the same ($p = 0.5$) for these two types of lattices.

the spanning cluster is fractal such that in the infinite system limit the fraction of occupied sites containing the spanning cluster vanishes [18]. For $p > p_c$, $P_\infty > 0$. More precisely, $P_\infty \sim (p - p_c)^\beta$ just above the transition ($p - p_c \ll 1$) with P_∞ eventually becoming unity when $p = 1$. See Fig. 1.4. Note that this transition is a continuous one because the order parameter is a continuous function of p . Of course, it is not an analytic function of p given the discontinuity in the derivative.

While there is definitely more to be said about this phase transition in connect- edness in percolation, I will emphasize two more relevant points before moving on to constraint percolation. Our beginning discussion of the fluid-to-amorphous solid transition is relevant here as percolation was initially conceived in the context of gelation, the chemical process by which a solution of polymers cross-link to form a gel—an amorphous solid [19]. In a bond formulation of percolation, occupied bonds denote chemical crosslinks between two polymers. So percolation was motivated by

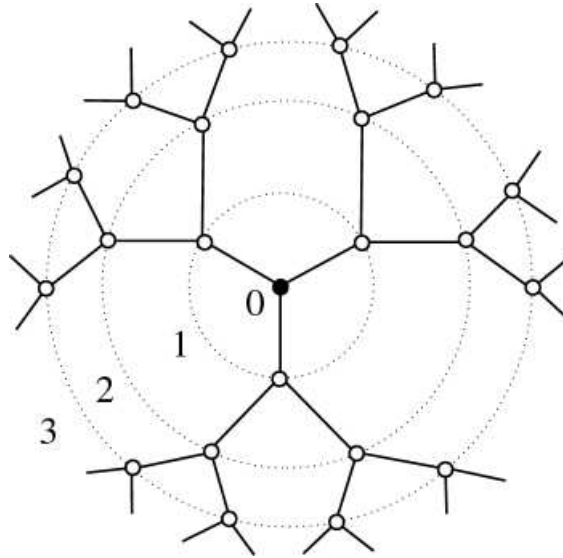


Figure 1.5: A Bethe lattice with $z = 3$, where z is the coordination number. Note the absence of loops. The numbers indicate the level, or layer, number.

this transition back in the 1940s [19]. As for the second point, the order parameter exponent β mentioned in the previous paragraph depends, to some extent, on the nature of the underlying lattice. On what is known as the Bethe lattice, which is a tree structure with no loops, $\beta = 1$. See Fig. 1.5 for a depiction of a Bethe lattice with coordination number z . On a square, or even triangular, lattice, $\beta = 5/36$. On the latter two lattices, there are many loops, loops on all scales in fact. It is this no loops versus loops that modifies the order parameter exponent so dramatically. Even so, the phase transition still remains continuous in either case.

1.4 Constraint percolation

In percolating systems such as gelation [19] the development of crosslinks, or connectivity, is random. In jamming, however, the connectivity, or contacts between particles, is constrained. For a system of frictionless, spherical particles to be mechanically stable, there must be $d + 1$ contacts per particle and the forces must

balance. How does one implement these constraints in a percolation model to work towards understanding of the jamming transition? Well, the *constraint percolation* model known as k -core percolation implements the $d+1$ contacts per particle [20]. To define k -core percolation, occupy the sites of an empty lattice with probability p as before. Occupied sites that have less than k occupied neighboring sites are recursively removed until all occupied sites satisfy the clustering constraint at which the removal stops. Cluster statistics analysis is performed on the remaining k -core clusters. See Fig. 1.6 for an example.

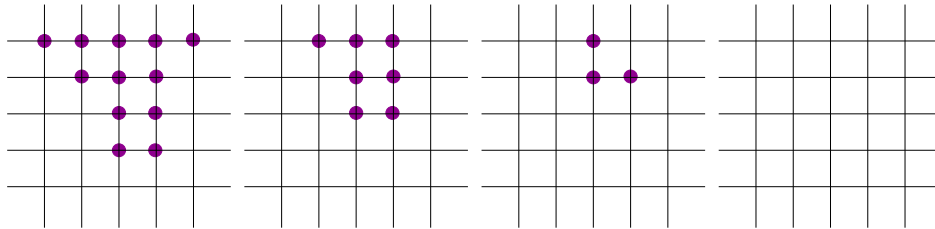


Figure 1.6: An example k -core culling for $k = 3$ on the square lattice. Each picture represents one iteration of the culling process. For this particular initial configuration, nothing remains. This is because no finite k -core clusters can exist for this particular lattice and value of k . Therefore $p_c = 1$ for 3-core on the square lattice.

Even though with k -core percolation only some of the granular physics is captured, in fact a minimal amount, there is quantitative agreement between mean field $k \geq 3$ -core exponents, k -core percolation studied on a Bethe lattice, and the exponents measured in the jamming transitions (in two and three dimensions). Furthermore, despite the existence of critical behavior in terms of diverging length scales, for both $k \geq 3$ -core and jamming, the order parameter, the fraction of sites making up the jamming or the spanning k -core cluster, jumps discontinuously at the transition. However, unlike ordinary discontinuous phase transitions where any further increase in the tuning parameter produces a proportional change in the order parameter, an increase in p here produces a response which scales as a square root. Therefore, the $k \geq 3$ -core transition is of a mixed nature where the order parameter is discontinu-

ous but the susceptibility diverges just as observed near in the jamming transition. This behavior is very different from unconstrained percolation where the transition is continuous [18].

What is known about k -core on other lattices besides the Bethe lattice? For the k -core models studied so far on the triangular lattice or the cubic lattice the transition appears to be continuous and in the same universality class of unconstrained percolation, or the transition does not occur until $p_c = 1$, i.e. no site is in the k -core cluster except when $p = 1$. Examples of the first type of behavior are $k = 3$ on the triangular lattice [21] and $k = 3$ on the cubic lattice [22]. Examples of the latter are $k = 4$ on the triangular and $k = 4$ on the cubic lattice [23]. So why when going from the Bethe lattice with no loops to Euclidean lattices with loops at all scales, does the nature of the k -core percolation transition change? This is the question I would like to address in Chapter 2 of the thesis. To do so, I must first introduce the notion of *hyperbolic lattices*.

1.5 Hyperbolic Geometry

A geometry is a mathematical construction that is based on a set of postulates that are assumed to be true and cannot be deduced from another hypothesis. The most intuitive geometry is Euclidean geometry that is extensively applicable in the sciences. One of the most remarkable postulates in Euclidean geometry is the so-called fifth postulate. The fifth postulate states that parallel to a straight line there is one and only one straight line parallel to it and passing through a given point A . For around two thousand years leading up to the eighteenth century, various geometers tried to demonstrate the internal consistency of Euclidean geometry from the other four postulates and neglecting the fifth one, but they always reached a contradiction. In the eighteenth century, however, it was proven that the negation of the fifth postulate along with the other four postulates results in a new kind of geometry that is called

hyperbolic geometry. This proof was done by Felix Klein in 1871 [24]. This new geometry has some different implications as compared to the Euclidean geometry. For example, the internal angles in a triangle sums to less than 180 degrees, the circumference of a circle of radius r is greater than $2\pi r$, and the Pythagorean theorem is no longer satisfied. One of the most interesting facts of the hyperbolic geometry is that it enables one to model geometric objects with properties that resemble those on the Bethe lattice. The quotient between the perimeter and the area of a polygon in Euclidean space is negligible when the polygon becomes sufficiently large, meanwhile, on the Bethe lattice, the perimeter grows at rate comparable to, or greater than, the area or volume. This property also holds for hyperbolic lattices.

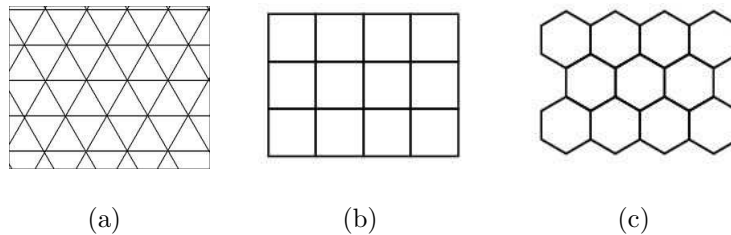


Figure 1.7: Euclidean tessellations of the plane.

A very interesting implication is that hyperbolic geometry enables more tessellations than Euclidean geometry. A tessellation of a plane is a tiling of the plane by regular polygons. The Euclidean plane just admits 3 tessellations, by triangles, squares, and hexagons. See Figure 1.7. We use the standard *Schlaflti* $\{P, Q\}$ symbol to denote a tessellation of the plane that at every vertex Q polygons of P sides meet. Consequently, tessellations admitted by the Euclidean plane are $\{3, 6\}$, $\{4, 4\}$, and $\{6, 3\}$. The hyperbolic plane admits any tessellation $\{P, Q\}$ such that $(P - 2)(Q - 2) > 4$. Note that the tessellations admitted by the Euclidean plane satisfy $(P - 2)(Q - 2) = 4$. Therefore, there are an infinite number of tessellations that can be built on the hyperbolic plane. The hyperbolic plane admits several representations, one of the most common is the *Poincare disk*. This is the open disk of radius one with its boundary

representing infinity. The metric is such that two points at a Euclidean fixed distance $d < 1$ will be more distant as they get closer to the boundary. Examples of tessellations on the hyperbolic plane are shown in Figure 1.8. The famous artist M. C. Escher, who was interested in the idea of depicting the infinite, and after correspondence with the mathematician H. S. M. Coxeter, made the famous representation illustrated in Figure 1.9.

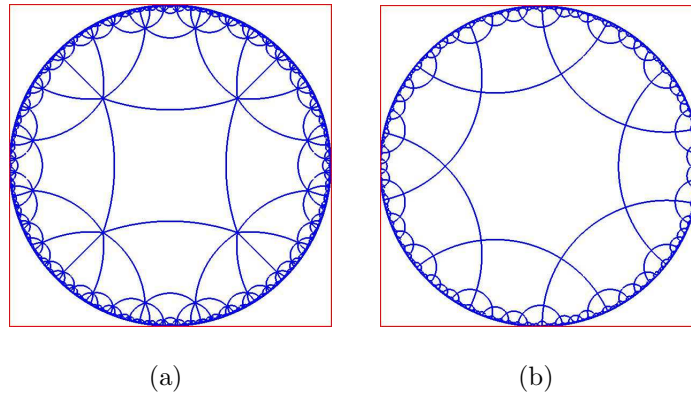


Figure 1.8: (a) A $\{4, 7\}$ hyperbolic tessellation. (b) A $\{7, 4\}$ hyperbolic tessellation.

Condensed matter physicists have become more interested in hyperbolic geometry as of late. For instance, there is the description of the thermodynamics of a fluid embedded in the hyperbolic plane [25] and the study of the Ising model on the hyperbolic plane [26]. My reason for investigating, as you will see, k -core percolation on hyperbolic lattices is to get at this question of why k -core percolation behaves differently on Bethe lattices versus Euclidean lattices. Hyperbolic lattices interpolate between the two in that the ratio of perimeter to area does not vanish in the infinite system limit and the farther away one goes from the center of a hyperbolic lattice, it is more difficult to return to the center, i.e. loops are not as prevalent as on the Euclidean lattice. This investigation is presented in Chapter 3 and is being prepared for submission [17].



Figure 1.9: The famous bat picture drawn by M. C. Escher. All M.C. Escher works © 2014 by The M.C. Escher Company - the Netherlands. All rights reserved. Used by permission. Please see www.mcescher.com.

1.6 Glassy dynamics and cell motility

A glass can be formed by cooling a viscous liquid at high enough rates so that it avoids crystallization via nucleation [27]. This is the so-called glass transition and has been very related to zero-temperature jamming transition via the jamming phase diagram [28]. In this rapidly cooling liquid, it has been conjectured that the constituent particles, now molecules, become trapped in cages by their neighboring particles. A particle can leave its cage if it has enough energy to overcome the associated energy barrier potential. It is this caging that increases the viscosity of the liquid by orders of magnitude and may eventually freeze out the degrees of freedom in the system as the glass transition is approached. These cages were initially conjectured to occur in molecular glasses [29]. With the study of athermal systems such as sand grains and colloids, where the size of the constituent particles are larger than molecules by orders of magnitude, caging has been directly observed [30, 31]. See Fig. 1.10. As one approaches a jamming-type transition, the number of particles involved in the uncaging event becomes larger such that particle rearrangement becomes increasingly collective. Eventually, as the temperature is lowered further, no particle can escape their respective cage.

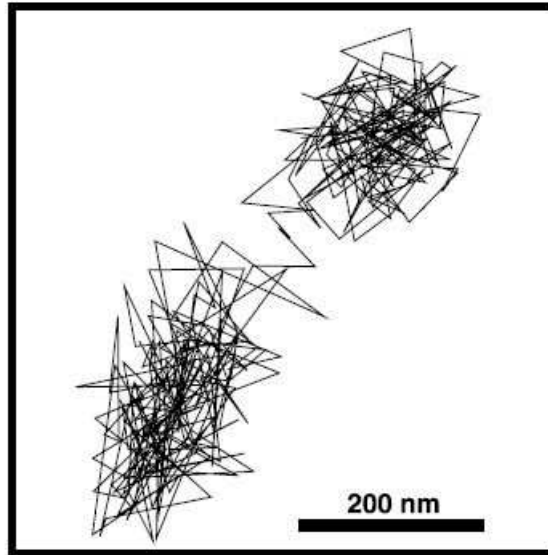


Figure 1.10: A typical trajectory of a colloidal particle at 56 percent packing fraction for 100 minutes. The colloids spend most of their time confined in cages formed by their neighbors and moved significant distances only during quick, rare cage rearrangements. Image from Ref. 31.

In the case of glasses, the energy barrier to overcome caging can be overcome mainly via thermal fluctuations. In the case of foams, the energy barrier is overcome if there is sufficient external force applied to the boundaries. Due to the disordered nature of the system, there is a distribution of energy barriers. See Fig. 1.11. It is useful to think of these energy barriers as transitions from one metastable state to another. These states represent mechanically stable arrangements of sand grains, for example. So as particle rearrangements occur the system goes from one metastable to another in some complex potential energy landscape, where the minima represent metastable states and the saddles represent transition paths that connect the various minima [32].

The standard expression for the transition rate R over a barrier between two energy minima A and B in a thermal system is given by an expression of the form

$$R = \omega_0 e^{-\Delta E/k_B T} \quad (1.2)$$

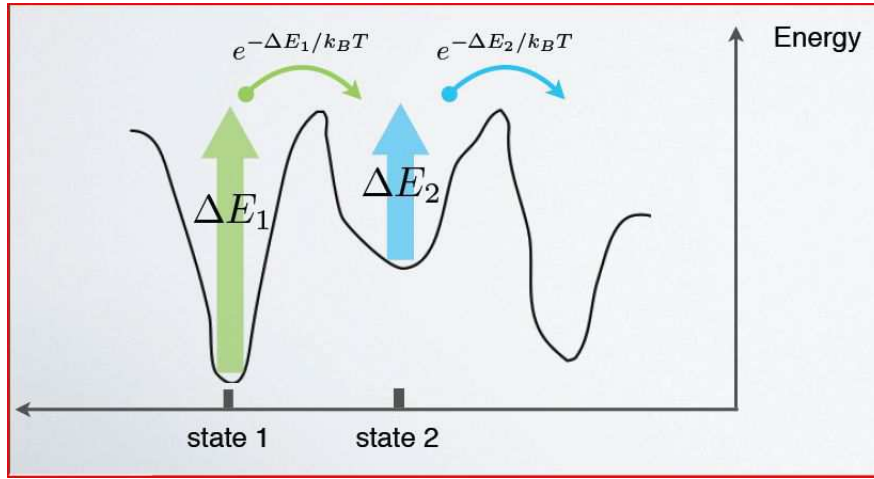


Figure 1.11: Simplified depiction of energy barriers in state space.

where R is the attempt frequency, k_B is the Boltzmann constant, T is a temperature of the system, and ΔE is the associated energy barrier. This equation is called the Arrhenius equation. This rate can be calculated using a first passage time approach. This rate is for one individual transition. In the complex potential energy landscape there are many energy barriers.

Dynamical consequences of this distribution of energy barriers can be obtained using a trap model or a soft glass rheology model where the statistics of the energy barriers are taken into account [33, 34]. I will not delve into the details of such calculations here. Instead, I will tell you that the consequences of this energy barrier distribution may lead to *anomalous diffusion* and dynamical heterogeneities. In a typical diffusion process the mean squared displacement, denoted by $\langle x^2(t) \rangle$, of a particle is a linear function of time. Anomalous diffusion is a diffusion process where $\langle x^2 \rangle \sim Dt^\mu$, where D is the diffusion coefficient and t is the time. For an anomalous diffusion process μ is different from one. Anomalous diffusion processes with $\mu > 1$ are called super-diffusive and those with $\mu < 1$ sub-diffusive. Dynamical heterogeneities refer to the nontrivial spatiotemporal fluctuations that accompany the temporary formation of rigid amorphous structures in glasses and granular ma-

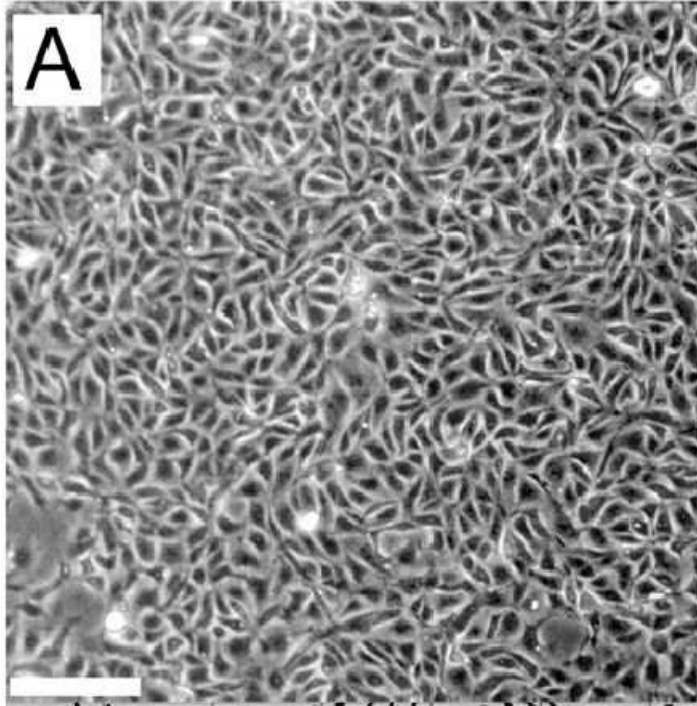


Figure 1.12: MCDK cells within a confluent monolayer. The scale bar is 100 microns. Image from Ref. 35.

terials. For example, the relaxation times span a very broad range and are strongly nonexponential.

And now we finally arrive at living matter. All of the above on glassy dynamics was first thought of in the context of dead matter. And yet, when one studies dynamics in confluent tissues—a collection of cells with no gaps between the cells—(see Fig. 1.12 for an image of a confluent tissue) one finds caging, anomalous diffusion, and dynamical heterogeneities [35, 36, 37]. From a physicist’s perspective, one major similarity between particle systems and cellular systems is that it costs energy to deform either particles or cells. Cells are, well, viscoelastic objects at the ten micron size scale. A tissue is a collection of such objects. While, indeed the mechanics of each cell is more complicated than a repulsive soft sphere, perhaps some of the *collective* mechanical and dynamical behavior carries over from the dead systems. What details

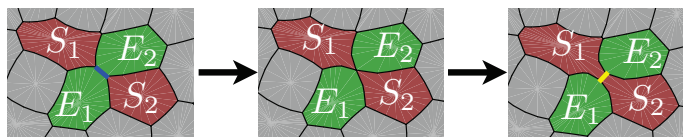


Figure 1.13: Depiction of a T1 transition in a model confluent tissue.

are important for determining such properties and what details are not? From a physicist’s perspective, one major difference between nonliving and living matter in the context of the complex potential energy landscape is that an individual cell can overcome an energy barrier by consuming its internal energy sources. Cells are active material. It is not clear how this difference would change collective mechanical and dynamical properties.

Unlike nonliving particles, even though the packing fraction of the confluent tissue is unity, the cells can change shape and squeeze past their neighbors in the absence of any applied force [38]. The cells do so via what is called a *T1 transition*, which is simply a topological process that interchanges neighbors as illustrated in Figure 1.13. Therefore, the analysis of the energy barriers a cell can potentially overcome in the process of migration in a confluent tissue can be studied via these T1 transformations. This work is presented in Chapter 4 and has been published [39] with a longer paper in preparation [40].

1.7 Nonglassy dynamics and cell motility

In Chapter 5 of the thesis, I go back to the simpler problem of single cell migration. Most quantitative understanding of single cell motility pertains to cells crawling on synthesized surfaces coated with extracellular matrix (ECM) proteins [41, 42]. And while progress has certainly been made in terms of being able to, for example, predict cell shape based on its speed, is a smooth surface an environment native to an *in vivo* crawling cell? The answer is typically no. Epithelial cells, when not in a confluent

tissue, must crawl through the three-dimensional ECM to heal a wound. The ECM consists mostly of fibrous collagen with a pore size that can range up to the order of the cell size (tens of microns). How does this type of environment affect single cell motility in terms of speed, overall direction of migration, and sensitivity or robustness to changes in the environment?

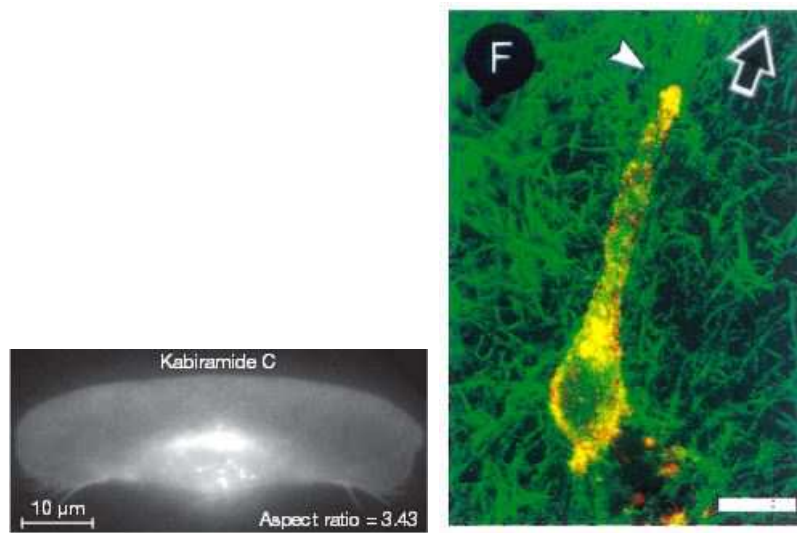


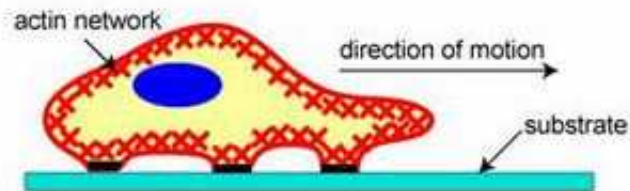
Figure 1.14: Birdseye view of cell motion. Both cells are moving upwards. (a) Fluorescence image of keratocyte cell. Image from Ref. 42. (b) Confocal reflection contrast image of a MV3 melanoma cell. The scale bar is 18 microns. Image from Ref. 136.

Experiments clearly demonstrate that cells crawling through the ECM can take on a very different shape from the ones crawling on two-dimensional surfaces, namely they mimic the fibrous environment of the ECM by elongating as they traverse along fibers [43]. An elongated shape is very different from the fan-like cell shapes observed in two dimensions such that new approaches to quantitative modeling are needed. Figure 1.14 illustrates the difference in cell shape between the two cases.

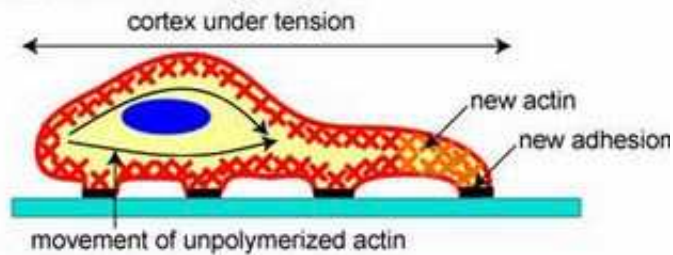
To give context to my work, let me review qualitatively cell crawling on two-dimensional surfaces (see Fig. 1.15). The cell first extends its front via *actin filament* polymerization and nucleation. Actin filaments are one of the three types of filaments making up the cellular cytoskeleton (see Fig. 1.16(a)). An actin filament is a polar

homopolymer filament with a plus, or barbed, end where G-actin monomers are added and a minus, or pointed, end where depolymerization occurs. Due to a difference in the off/on rates between the two ends, a phenomenon known as treadmilling can occur where there is net motion of the center of mass of the filament via just polymerization and depolymerization. The typical lengths of actin filaments range from 1 micron to 100 nanometers.

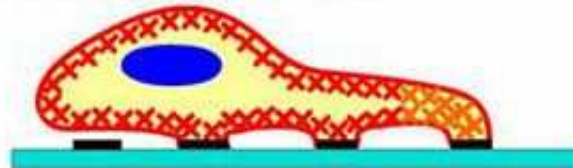
1) Protrusion of the Leading Edge



2) Adhesion at the Leading Edge



Deadhesion at the Trailing Edge



3) Movement of the Cell Body

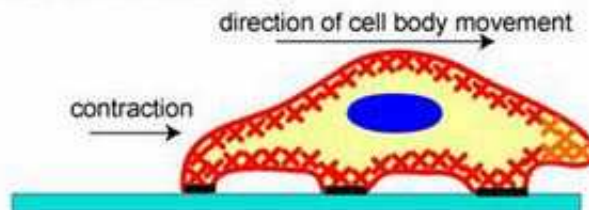


Figure 1.15: Side-view schematic of a cell crawling on a surface.

As actin nucleation and polymerization occurs extending the cell front in a particular direction, the cell is also creating focal adhesions under this new extension. Focal adhesions are large macromolecular assemblies that attach the cell to the underlying substrate (see Fig. 1.16(b)). One of the dominant proteins in focal adhesions is *integrin*. Meanwhile, focal adhesions are disassembled near the rear of the cell so that the rear can retract to catch up with the front, which has continued to extend. The retraction is myosin-driven since the use of blebbistatin suppresses motility of a cell [44], though leading edge cell fragments can continue to move via actin-treadmilling [45]. *Myosin II* is one of ATP-dependent motor proteins and is probably best known for its role in muscle contraction. Individual myosin motors contain two heads and walk along actin filaments towards the plus end. Myosin can aggregate to form myofilaments with one part of the myofilament cluster attaching to one actin filament and the other part attaching to another actin filament, etc. See Fig. 1.16(c) for an illustration from muscle where the action of the myosin contracts the sarcomere. The plus ends of the actin filaments are located near each Z-disc in the figure. In the cytoskeleton, where the actin filaments are disordered, a similar contraction and, therefore, retraction can occur so that the rear of the cell can catch up with the front.

In this cell crawling on surfaces scenario, actin filament nucleation is driven by the branching agent, Arp2/3 [46]. Arp2/3 nucleates branched filaments at a reasonably regular angle of 70 degree from the polymerizing end of actin filaments and, therefore, helps set the lateral extent of the leading edge of the crawling cell. This extent can be broad for crawling on two-dimensional substrates, resulting in fan-like shapes at the leading edge. This fan-like shape is very different from those cells crawling along ECM fibers. In Chapter 5, we propose a cell crawling model where Arp2/3 is not necessary for migration. Instead, the important components are the stress fibers and the focal adhesions. Stress fibers are similar to the organization of muscle, but more disordered, and they extend across the cell as it moves. Focal adhesions mediate the interaction between the cell and the ECM fiber. And while there is no fluid-to-amorphous solid

transition in Chapter 5, the matter is living and the rigidity/elasticity of the stress fibers is active. The work presented in Chapter 5 is currently under review [47].

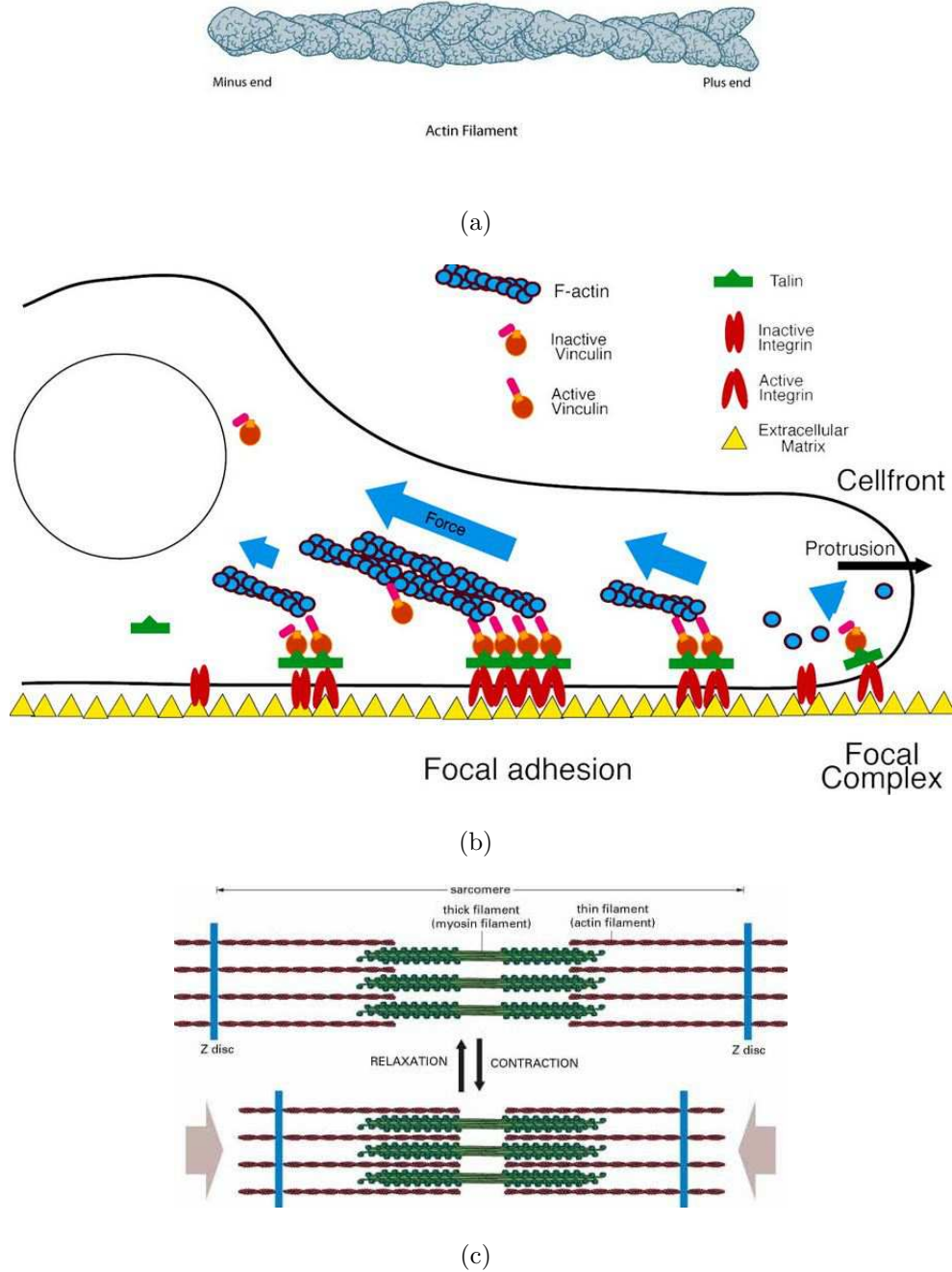


Figure 1.16: (a) Schematic of an actin filament. The diameter of a single actin monomer is roughly 5.4 nm . (b) A schematic of a cell interacting with a surface via focal adhesions with the integrins denoted in red. (c) A schematic of a sarcomere, the unit that is repeated in striated muscle. The length of a sarcomere is typically 2 microns.

Chapter 2

Jamming graphs: A local approach to global mechanical rigidity

A model system for understanding the onset of rigidity in disordered particle packings is a d -dimensional collection of frictionless, repulsive soft spheres at zero temperature [5, 6, 9, 10, 11]. At small packing densities, minimal energy configurations are those with no contacts between particles. As the packing density is increased, the contact geometry abruptly changes from nonexistent to one where the average coordination number equals $2d$ [6]. Moreover, the local coordination number for each particle must be at least $d + 1$ in accordance with the Hilbert stability condition, or local mechanical stability [48]. As the packing density is increased even further, the average coordination number exceeds $2d$ with each particle still obeying the Hilbert stability criterion.

The abrupt jump in contact geometry indeed has the flavor of a phase transition even though no symmetries in the positions of the particles are broken [6, 9, 10]. Continuous transitions are typically accompanied with at least one diverging lengthscale at the transition, such as connectivity percolation [18]. Discontinuous transitions, however, are not typically characterized by any diverging lengthscales. And yet, Wyart and collaborators [49, 50] identified a diverging lengthscale in the disordered

solid phase, denoted as l^* , such that the combination of the discontinuous jump in the average contact number and the diverging lengthscale suggests a more exotic mixed transition, such as the found in k -core percolation [20].

This lengthscale, l^* , can be determined by finding a cut-out subsystem of some length below which there exists extended zero energy modes, i.e. modes of vibration that do not cost energy, within the subsystem and above which there does not. At the transition, extended zero-energy modes proliferate due to the absence of redundant contacts, and l^* is of order the system size. As the system solidifies further with added redundant contacts, l^* decreases since such contacts make it less likely for zero-energy modes to extend across the subsystem. In practice, this lengthscale l^* is inferred from numerical measurements of the frequency at which the density of states deviates from the plateau region emerging at low frequencies. Very recently however, a new construction of l^* via rigid clusters results in a direct numerical measurement [51]. Another lengthscale associated with subsystems with fixed boundaries (as opposed to cut/free boundaries) has been recently identified and scales similarly with l^* [52, 53, 54], though corrections to scaling are discussed [52, 53].

While the focus on identifying a diverging lengthscale has been on the competition between bulk and boundary effects when cutting out a subsystem and probing for extended zero energy modes, little work has been done to search for a lengthscale associated with a change in the zero-energy mode structure in response to the breaking of one or several contacts, for example. After all, when searching for diverging lengthscales in systems undergoing phase transitions, one typically perturbs the system and computes the lengthscale over which the system responds to that perturbation. And while prior focus on cut-out subsystems has certainly proved useful, we ask what can be learned from removing one or two contacts and looking for a lengthscale over which the perturbation affects the mode structure? Point perturbations have been performed when investigating the force network of the particle packing above jamming [55, 56] and on phonon modes in floppy networks, i.e. below jamming [57].

Here, we explore random bond deletion effects on the structure of zero-energy modes via the study of rigid clusters and ask "does some diverging lengthscale fall out of such computations?" If so, is this lengthscale similar to l^* , or not?

To begin to answer such questions, we first present a novel way to build the contact geometry of polydisperse, frictionless, repulsive soft discs in two dimensions at the onset of rigidity. We do so with vertices representing particles and bonds representing contacts between particles. After all, at the transition there are no forces, i.e. the particles are in contact but not overlapping, so one does not necessarily need to rely on forces explicitly to generate the packing. This jamming graph algorithm uses spatially local rules to generate the contact geometry in two dimensions—local rules that encode the global rule of minimal rigidity. Interestingly, the percolation transition, with its local rules, can be described by a field theory [58]. If the abrupt changes in contact geometry in the frictionless, repulsive soft sphere system can also be characterized by local rules, can such a system be described by a field theory? After introducing our algorithm, we then perturb the contact geometry of the jamming graph and study the resulting rigid cluster distributions.

The study of rigid clusters has its roots in rigidity percolation [59, 60, 61]. In rigidity percolation, one demands that the cluster spanning a system of randomly diluted bonds on a lattice be rigid in the sense that if each bond were associated with, for example, a spring, then there would be a finite energy cost to deforming the cluster. In two dimensions, numerical studies suggest that the onset of rigidity is a continuous phase transition [62, 63, 64]. Rigidity percolation differs from jamming in that jamming occurs in a particulate system, where particles can come in and out of contact, i.e. the connectivity is not fixed. Rigidity percolation also differs from both jamming and the jamming graph in that there are local constraints on the geometry to take into account local mechanical stability in the presence of purely repulsive forces.

This chapter is organized as follows. Section II discusses the local and global

properties of the contact geometry of frictionless, repulsive soft spheres. Section III presents the algorithm for building a jamming graph, Section IV addresses perturbations of the jamming graph, and Section V discusses the implications of our results.

2.1 Contact geometry of frictionless, repulsive soft spheres at the onset of rigidity

The initial link between contact geometry and the onset of rigidity in mechanical networks with fixed connectivity is due to Maxwell via the Maxwell constraint counting condition [14]. This condition is a necessary (but not sufficient) for mechanical rigidity. It does so by counting the number of zero-energy, also known as floppy, modes in the network, N_f , which depends on the number of independent constraints, N_c , and the local degrees of freedom for each particle. For mechanical networks with particles interacting via central forces,

$$N_f = Nd - N_c, \tag{2.1}$$

where N is the number of particles in the network. The onset of rigidity, or minimal rigidity, occurs when N_f equals the number of global degrees of freedom of the network, N_g . When $N_f = N_g$, the network is minimally rigid and the removal of just one edge in the network makes it flexible. In mean-field, one can replace N_c with $\langle z \rangle \frac{N}{2}$, where $\langle z \rangle$ is the average coordination number such that the minimally rigid condition in the large N limit becomes $\langle z \rangle = 2d$, i.e. isostaticity. Numerical simulations indicate that the onset of mechanical rigidity for soft repulsive, frictionless spheres corresponds to the isostatic condition even though the connectivity of the system is not fixed [6].

In two dimensions, one can extend the above necessary condition for minimal rigidity in central-force fixed connectivity networks, such as the ones studied in rigidity percolation, to necessary and sufficient using Laman's theorem [15]: *A network*

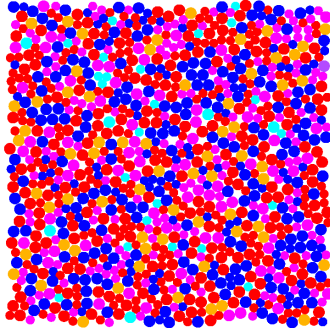


Figure 2.1: A jammed, bidisperse (i.e. with two different radius) particle packing with $N = 1024$ and packing fraction $\phi = 0.841$. The colors denote the local coordination number, z , with light blue denoting $z = 0$, magenta denoting $z = 3$, red denoting $z = 4$, blue denoting $z = 5$, orange depicting $z = 6$, and purple denoting $z = 7$, which is possible for the 1.4 diameter ratio for the bidisperse system.

with N vertices is generically, minimally rigid in two dimensions if and only if it has $2N - 3$ bonds and no subgraph of n vertices has more than $2n - 3$ bonds. Laman's theorem is global (or spatially nonlocal) in the sense that it involves all possible subgraphs. However, we will present a construction of the Laman graph implemented via spatially local rules involving both the addition and deletion of bonds developed earlier by Henneberg [65]. Such an algorithm falls under the jurisdiction of correlated percolation where there are constraints on the occupation of bonds as the graph is constructed. Note that for Laman's theorem, $N_g = 3$. Moreover, a recent generalization of Laman's theorem to $kN - N_g$ extends the concept of minimal rigidity [66].

Fixed connectivity central-force networks from rigidity percolation and soft, repulsive discs differ from each other in the following two ways. In the particulate system, the contacts are not fixed. These contacts break/rearrange as the system minimizes its energy or responds to perturbations. Additionally, there are only repulsive forces in the particulate system in contrast to central-force networks, which are typically spring networks exhibiting both attractive and repulsive forces. Do these differences have

any implications for characterizing the contact geometry of the particulate system at the onset of rigidity, or jamming? Indeed, they do. At the transition, in addition to the system being minimally rigid, each particle must be locally mechanically stable in the presence of purely repulsive forces. Otherwise, an infinitesimal perturbation can break a contact and the system becomes flexible.

What does local mechanical stability mean in terms of constraints on the contact geometry? In two dimensions, a particle must have at least three contacts and those contacts must be organized in such a way the particle cannot escape its local environment via a perturbation. More precisely, any particle should have at least three neighbors, i.e. it is 3 – *core*, and the particle should be inside a triangle determined by at least three of its neighbors [48]. This local geometric condition is known as the Hilbert stability condition and is illustrated in Fig. 2.2. If this local condition is not obeyed, then the entire packing can go unstable due to an infinitesimal, local perturbation.

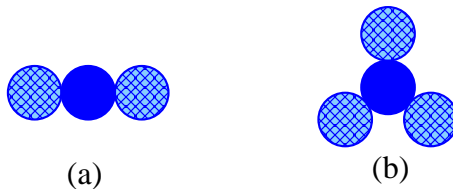


Figure 2.2: (a) The center particle is not mechanically stable (for the other two particles fixed). (b) The center particle is mechanically stable.

Therefore, just as S. Alexander [48] argued that the concept of geometrical rigidity for spring networks, when extended to particle networks, needs to incorporate the breaking of contacts, the rigidity transition for frictionless, repulsive soft discs in two dimensions is characterized by a spanning, planar graph obeying both the Laman condition *and* by the principle of local mechanical stability (Hilbert stability). We call this graph a “jamming graph”. The vertices in the graph represent the particles and since the bonds represent particle contacts, the graph must be planar.

We would like to understand how such graphs obeying both global and local rules

of mechanical stability are constructed in practice. It turns out that we will be able to do so using an algorithm with spatially local moves. This is because one can build a Laman graph via an algorithm called the Henneberg construction [65]. The algorithm will be presented in the following section. Therefore, we now explore the notion of minimal rigidity in particle packings in two dimensions, where the connectivity is not fixed and the forces exerted above jamming are purely repulsive, by imposing *both* types of mechanical stability.

2.2 Algorithm for building jamming graphs

2.2.1 Henneberg construction

Let us review the Henneberg construction [65]. For constructing a Laman graph, we begin with a triangle and then add a vertex and connect it to prior vertices using the Henneberg steps Type I and Type II defined below:

- Type I step: Add a vertex and join it to two prior vertices via two new bonds;
- Type II step: Add a vertex and join it to three prior vertices with at least one bond in between the three bonds. Remove a prior bond between the three connecting prior vertices.

See Fig. 2.3 for an illustration of the Henneberg construction.

A graph constructed using the Henneberg construction is Laman [15]. We can see this via induction. Suppose the current graph G is Laman with N vertices and $2N - 3$ bonds.

For the Type I step: Add vertex x . Graph G now contains $N + 1$ vertices and $2N - 3 + 2 = 2(N + 1) - 3$ bonds. For any subgraph with n vertices, if it does not include x , by the induction hypothesis, there are at most $2n - 3$ bonds. If the subgraph includes x , for the other $n - 1$ vertices, there are at most $2(n - 1) - 3$ bonds between them, so in total there are at most $2(n - 1) - 3 + 2 = 2n - 3$ bonds.

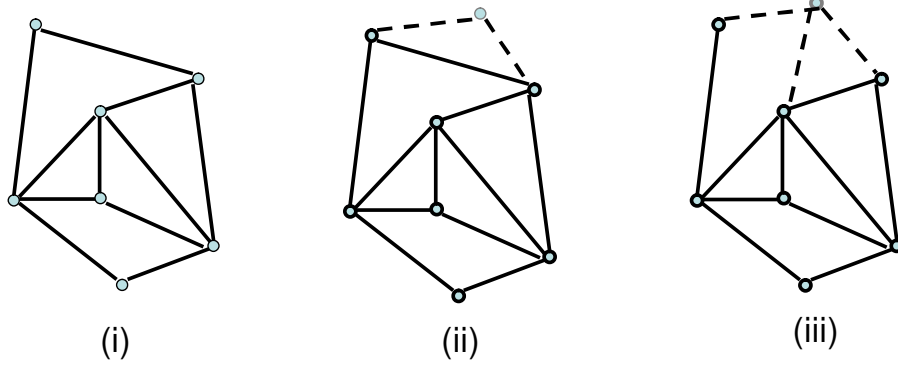


Figure 2.3: (i) Graph before Henneberg step. (ii) Type I step with the new bonds denoted with dashed lines. (iii) Type II step.

For the Type II step: Add vertex x and connect it to a, b, c . Graph G now contains $N + 1$ vertices and $2N - 3 + 3 - 1 = 2(N + 1) - 3$ bonds. For any subgraph with n vertices, if it does not include x , by the induction hypothesis, there are at most $2n - 3$ bonds. If any subgraph includes x , for the other $n - 1$ nodes, there are at most

1. $2(n - 1) - 3$ bonds, if not all of a, b, c are included.
2. $2(n - 1) - 4$ bonds, if a, b, c are all included.

In case 1, there are at most $2(n - 1) - 3 + 2 = 2n - 3$ bonds. In case 2, there are at most $2(n - 1) - 4 + 3 = 2n - 3$ bonds. Thus, the Laman condition is satisfied. One can also show that every Laman graph can be decomposed into a Henneberg construction.

The Henneberg construction (and the corresponding Laman's theorem) is purely combinatorial. It only deals with adjacency and not where the neighbors are located spatially. Because bonds in the jamming graph represent contacts between particles, we impose a planarity, or no-crossing condition, on the bonds. Moreover, if $N_g = 2$, as opposed to $N_g = 3$, the above Henneberg construction is unchanged.

2.2.2 Hilbert stability

We also invoke the local Hilbert stability condition for two-dimensional packings, which states that any vertex should have at least three neighbors, i.e. it is *3-core*, and the vertex should be inside a triangle determined by at least three of its neighbors [48]. To determine whether or not a vertex is enclosed in a triangle by at least three of its neighbors, we implement an algorithm based on the Jordan Curve Theorem [67]. It consists of drawing a horizontal line from the vertex and determining how many crossings the horizontal line makes with the enclosed triangle. If there are an odd number of crossings, then the vertex is inside the polygon as illustrated in Fig. 2.4.

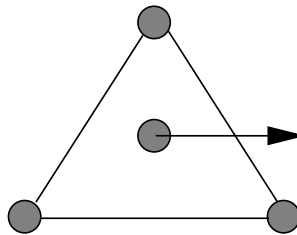


Figure 2.4: Illustration for checking if a particle enclosed by a triangle.

2.2.3 Pseudocode

Graphs built by using Henneberg type II steps have typically more counter-balanced vertices since the new vertex has more neighbors in comparison to Type I. So we build a jamming graph implementing Henneberg type II steps only. The graph must be planar and we implement periodic boundary conditions on a square of length unity. We then enforce the Hilbert stability condition on each vertex. Here is the pseudocode of our algorithm.

- Create a triangle. The length of the bonds is chosen randomly from the uniform distribution on the interval $[r_{min}, r_{max}]$, where $r_{min} < r_{max} < 0.5$. The triangle is a minimally rigid $k = 3$, $N_g = 3$ structure.

- Create a new vertex with random coordinates with the constraint that no vertex be less than a distance r_{min} or greater than a distance r_{max} from any other vertex and establish its neighbors according to the Type II Henneberg step. This creation is succesful if the new bonds are not overlapping any of the surviving prior bonds (keeping in mind that a Type II Henneberg move implies the deletion of a prior bond).
- Repeat the above step $N - 4$ times to create a planar Laman graph with N vertices.
- Check for those vertices that are not counter-balanced.
- For each vertex that is not yet counter-balanced, impose the following set of strategies to enforce counter-balance. The strategies differ depending on whether an uncounter-balanced vertex has at least two neighbors or at least three.
- **Counter-balance strategies for a vertex with at least three neighbors:** Suppose uncounter-balanced vertex p has neighbors n_1 , n_2 , and n_3 , as shown in Figure 2.5. If p has more than three neighbors, we apply the following strategy to each set of the three diferent neighbors of p . Choose n_2 such that $\overrightarrow{pn_2}$ is inside the angle $\widehat{n_1pn_3}$. Then choose a vertex x such that

$$\overrightarrow{xp} = \overrightarrow{pn} + \frac{\overrightarrow{np}}{\|\overrightarrow{pn}\|}\alpha; \quad \overrightarrow{pn} = \beta\overrightarrow{pn_1} + (1 - \beta)\overrightarrow{pn_2}, \quad (2.2)$$

where α is equal to one half the distance from p to its closest neighbor and $0 < \beta < 1$. To counterbalance p so that it belongs to the triangle $\triangle n_1n_2x$, x should be in the angle determined by the vectors $\overrightarrow{n_1p}$ and $\overrightarrow{n_2p}$. By choosing particular values for β , for example $\beta = \frac{1}{10}, \frac{1}{2}, \frac{9}{10}$, most of the region containing the angle is scanned as illustrated in Figure 2.5.

New bonds \overline{xp} , $\overline{xn_3}$, \overline{xz} are created and the prior bond $\overline{pn_3}$ is deleted. Note that the new bonds cannot cross any of the prior ones. Then, a prior vertex z is

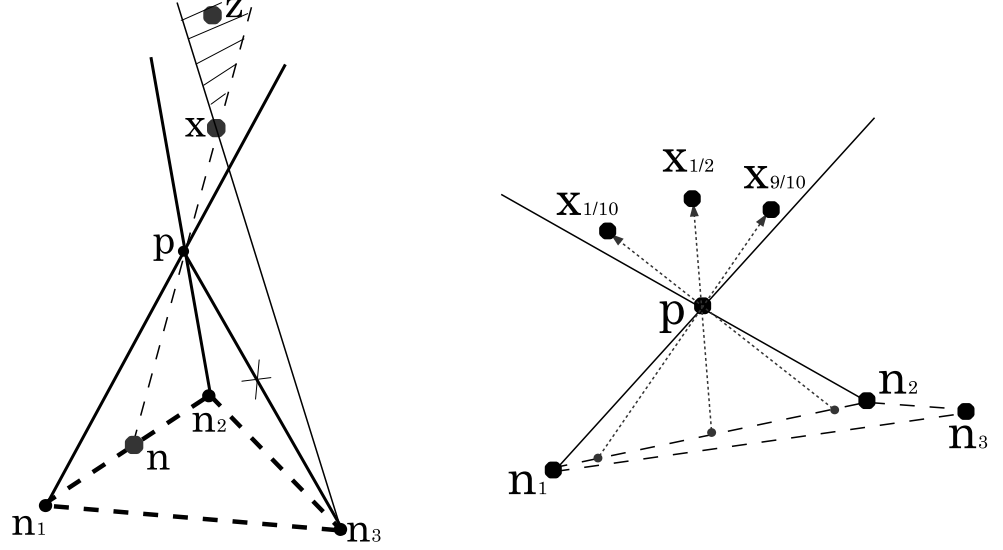


Figure 2.5: Left: An uncounter-balanced vertex p with at least three neighbors n_1, n_2, n_3 , is counter-balanced by creating bond \overline{px} and deleting bond $\overline{pn_3}$. Likewise, x is counter-balanced by finding z such that x is inside triangle $\triangle zpn_3$, consequently creating bond \overline{xz} . Right: An illustration of different positions to choose an appropriate neighbor x for uncounter-balanced vertex p . Values of β are chosen so that most of the space contained in the angle determined by vectors $\overline{pn_1}$ and $\overline{pn_2}$ is scanned.

chosen such that x is counter-balanced, which means it should be in the striped region in Figure 2.5. If the above counter-balance strategy does not work, move p towards n_2 by a fraction of the length $\|\overline{pn_2}\|$. Once p is moved, the above strategy is tried again. If this particular construction does not work, choose n to be between n_2 and n_3 .

- **Counter-balance strategy for a vertex with at least two neighbors:**

Assume the situation depicted in Figure 2.6, where p is an uncounter-balanced vertex with neighbors n_1 and n_2 . In this case, create a new vertex x such that

$$\vec{x} = \frac{\vec{np}}{\|\vec{pn}\|} \alpha; \quad \vec{n} = \frac{1}{2} (\vec{n}_1 + \vec{n}_2). \quad (2.3)$$

Then find two connected vertices a and b and create bonds \overline{xp} , \overline{xa} , \overline{xb} and delete the prior bond \overline{ab} . This strategy is successful if the new bonds do *not*

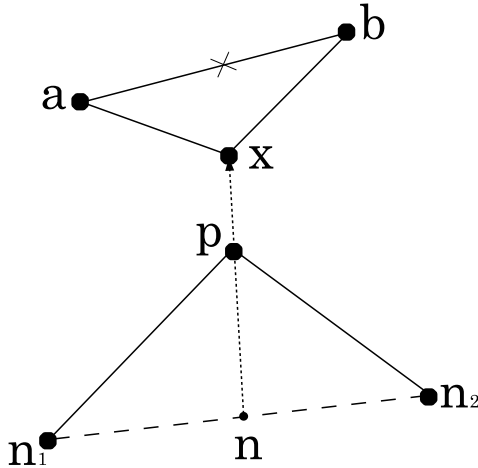


Figure 2.6: Uncounter-balanced vertex p is counter-balanced by finding two connected vertices a and b such that the creation of vertex x and bonds \overline{xp} , \overline{xa} , and \overline{xb} causes x to be counter-balanced. Also, bond \overline{ab} is deleted.

cross any of the prior ones and if either vertex a or b remain counter-balanced after deleting the bond connecting them. It is important to note that one can apply this strategy for a vertex with more than just two neighbors.

A few comments on the algorithm are in order. (0) The use of r_{min} and r_{max} set the local neighborhood from which vertices are connected. It is in this sense that the algorithm is local spatially. (1) We did not impose counter-balance during the Laman construction because Type II Henneberg steps delete bonds so that a counter-balanced vertex at one point during the graph construction may not be counter-balanced at some later point in the construction. Of course, Type I Henneberg steps do not delete bonds, but then a sizeable fraction of uncounter-balanced vertices emerge, approximately 75 percent, as compared to jamming graphs constructed using the Type II Henneberg steps, where approximately 50 percent of the bonds are counter-balanced automatically. (2) The algorithm begins with a triangle, which is a $2N - 3$ minimally rigid structure. While periodic boundary conditions imply $N_g = 2$, local

structures that are the equivalent of $2N - 2$ minimally rigid structure do not include single-bonded triangles. More precisely, for $N = 3$, one connection between two vertices must have a double bond. Since we begin the algorithm with a local structure and build up the graph from there with specific boundary conditions imposed for some fraction of connections that decreases as N increases, we implement $N_g = 3$. The $N_g = 2$ versus $N_g = 3$ for periodic particle packings presumably accounts for why an extra contact is needed a positive bulk modulus. (3) The jamming graph is one connected structure, i.e. there are no rattlers. Rattlers are usually removed by hand when studying elastic properties, for example, since they do not contribute to the network. (4) New vertices may be added to the jamming graph to enforce the counter-balance property. We use N to denote the number of vertices before counter-balance is enforced such that the approximate number of final vertices is $\frac{3}{2}N$.

To compare the jamming graph algorithm with other algorithms generating minimally rigid particle packings, such particle-based algorithms range from minimization methods [6] to adaptive network methods [68] to molecular dynamics [69, 70] to event-driven molecular dynamics [71]. When using these approaches, the transition point, defined by the packing fraction or the average pressure, can be protocol-dependent [72, 73, 74]. Moreover, convergence issues exist [51]. Our algorithm uses purely contact geometry to concretely define the onset of jamming in frictionless spheres. Indeed, there exist algorithms to generate generic disordered minimally rigid graphs via a matching algorithm [75, 76], where generic means that the vertex coordinates are not related by any symmetry. These graphs are not planar nor is local mechanical stability enforced. And finally, there exists a hybrid approach where high density particle packings are used to generate a disordered hyperstatic graph [77]. Then, bonds are then randomly deleted from the graph until, for example, $\langle z \rangle = 4$ is obtained. There is a constraint on the random deletion, however, where a bond is not deleted if the local coordination number of either of the two associated vertices goes below 3, otherwise known as the k -core condition [20]. However, both latter

algorithms do not necessarily enforce the geometry of local mechanical stability.

2.3 Perturbing jamming graphs

Now that we have an algorithm to construct jamming graphs, we perturb these graphs to determine how the system destabilizes (and restabilizes) mechanically. The destabilization is studied via the identification of rigid clusters. A rigid cluster defines those bonds that are rigid with respect to each other. A rigid cluster is defined on the bonds, as opposed to the vertices, because a vertex can belong to two different rigid clusters, while bonds can be identified with only one rigid cluster. The rigid cluster size s is defined as the total number of bonds belonging to a rigid cluster. We then use the powerful pebble game algorithm [16] to identify rigid clusters via an additional test bond. By construction, the jamming graph is one minimally rigid cluster. We now investigate how the jamming graph destabilizes with the removal of one bond. Note that the size of rigid clusters is measured in terms of bonds and not vertices.

2.3.1 One random bond deletion

The removal of one bond/contact creates exactly one floppy mode such that every bond is no longer rigid with respect to every other bond in the graph. In other words, there must be at least two rigid clusters in the graph. In fact, one can prove that there must be an even number of rigid clusters. So, precisely how many pairs of rigid clusters are there after one bond is randomly deleted: "Many microscopic rigid clusters with no rigid cluster of order the system size, or at least one rigid cluster of order the system size coexisting with microscopic sized rigid clusters?" We define a rigid cluster occupying some large fraction of the bonds in the system and to scale with the system size to be a macroscopic rigid cluster. This macroscopic rigid cluster need not necessarily span the system, though since it scales with the system size,

then it is likely too. Microscopic rigid clusters, on the other hand, do not scale with the number of bonds in the system. The smallest minimally rigid cluster is a triangle. It turns out that both scenarios are observed. See Figure 2.7. And while both scenarios occur, it turns out that the most common scenario is the absence of at least one macroscopic rigid cluster when one bond is deleted.

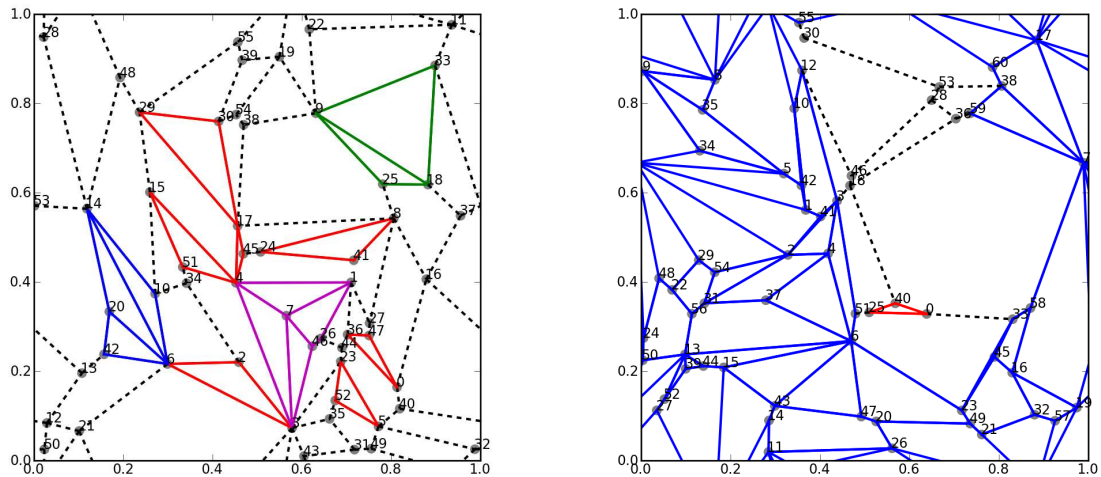


Figure 2.7: Left: Many small rigid clusters identified via color after the deletion of one bond/contact, namely the bond between vertices 1 and 41 as numbered. The black dashed lines indicate bonds that are not rigid with respect to any other bond. Right: A “macroscopic” rigid cluster (in blue) along with a few small ones after the deletion of the bond connecting vertices 12 and 30.

And while the survival of macroscopic rigid clusters after one bond deletion is apparent in the systems studied, do they persist in the large system limit? Figure 2.8 depicts the resulting rigid cluster size probability distribution, $Prob(s)$ for $N = 40, 80, 160,$ and 320 . Note that the rigid cluster size is in terms of bonds such that the rigid cluster sizes can be larger than the initial vertex number N . Indeed, the probability of observing a macroscopic rigid cluster after one bond deletion decreases with increasing system size. To obtain a systematic measurement, we compute the area under the characteristic peak at the macroscopic rigid cluster sizes s , $a^\#$. See

Figure 2.9. While the trend is not clearly power-law nor exponential, the area, $a^\#$, is decreasing with N , suggesting that macroscopic rigid clusters after one bond deletion vanish in the infinite system limit. This possibility, while not as likely as the many, microscopic rigid clusters scenario, cannot yet be completely ruled out in the infinite system limit, i.e. there is no mathematical proof.

For the sake of argument, consider the graph in Figure 2.10 [78]. Removal of the red dashed bond corresponds to each bond not being rigid with respect to any other, or many rigid clusters of size one. However, removal of one of the blue bonds leaves the rest of the rigid structure unchanged (except for the one neighboring bond that is no longer rigid with respect to any other bond). Depending on the bond that is deleted, either scenario holds in the infinite system limit. And while the specificity of this graph may not be useful for understanding the generic case, extensions of such examples may indeed be.

In the system sizes studied, the two scenarios—(1) many microscopic rigid clusters with no macroscopic rigid cluster and (2) at least one macroscopic, rigid cluster—can be related to two different floppy modes. In the many microscopic rigid clusters scenario, there is widespread break-up of the system. For bonds between individual rigid clusters, there is zero-energy cost to deforming those bonds such that if they are replaced by springs as is typically done when determining vibrational modes, these bonds contribute to any zero-energy modes. If these bonds extend across the system, as they do in the case of many microscopic rigid clusters, then the zero-energy mode is an extended one. In contrast, the presence of at least one macroscopic rigid cluster translates to a more localized zero-mode since the deforming bonds within the macroscopic rigid cluster will result in some energy cost.

Our finding is presumably related to the recent finding of two kinds of instabilities due to the breaking of contacts in a repulsive, frictionless particle packing at the onset of rigidity [79]. In this work, two particles in contact are pulled apart, i.e. a bond is deleted, and particle rearrangements driven by instabilities are identified. There

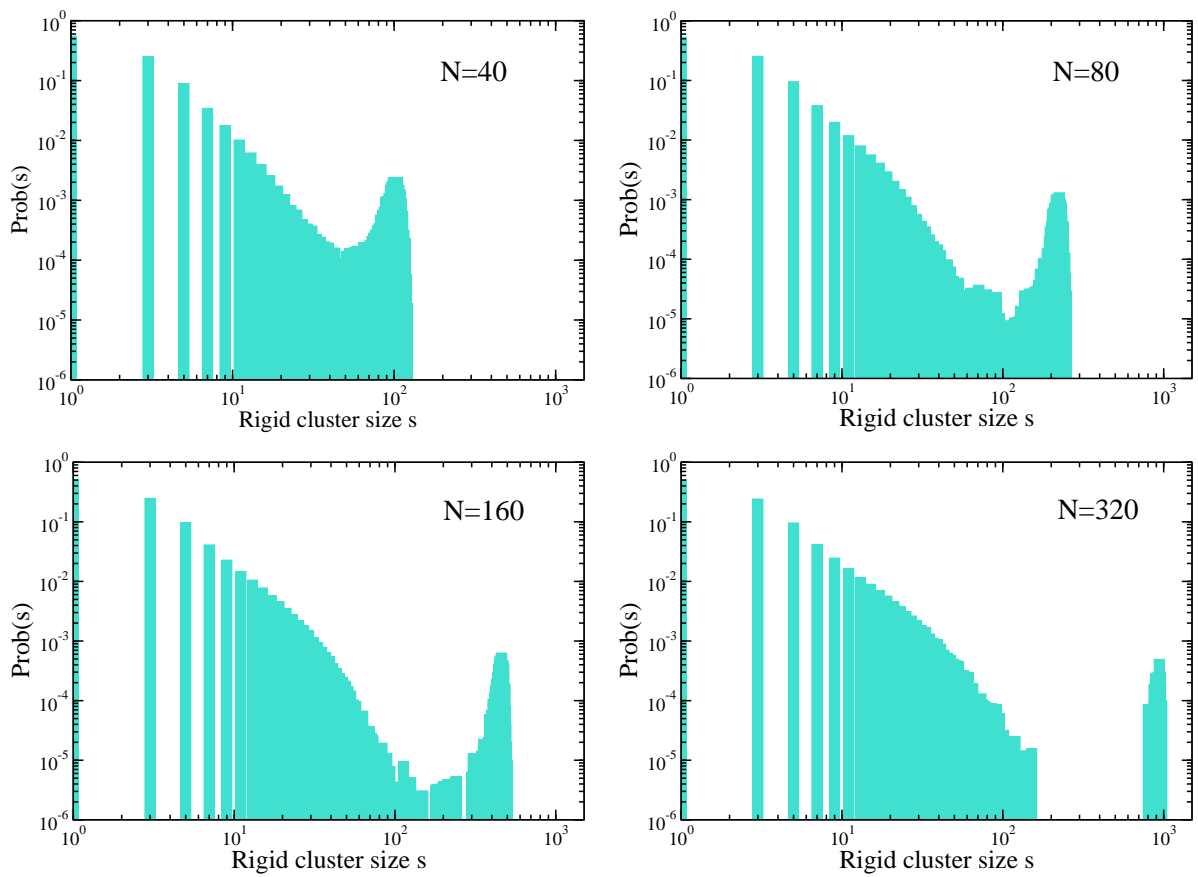


Figure 2.8: Plot of $Prob(s)$, the probability for a bond to participate in a rigid cluster of size s after one bond is deleted from the jamming graph. The different graphs represent different system sizes.

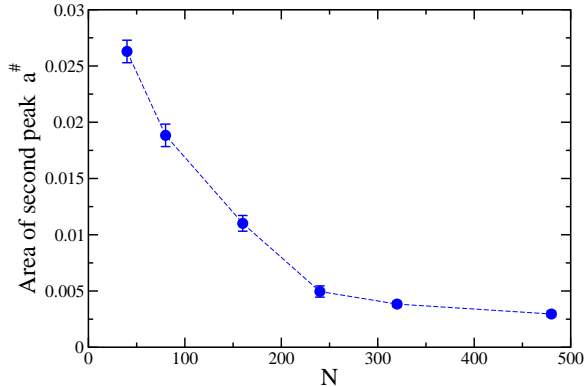


Figure 2.9: Plot of the peak area for the macroscopic rigid cluster sizes, $a^\#$, as a function of N initial vertices. The dashed line is merely a guide for the eye.

appear to be two kinds of instabilities—one extended and the other localized. While force information is assumed in this study, our work only uses contact information.

In addition to the decrease in $a^\#$ with increasing N , there is another trend in the probability distribution of rigid cluster sizes as the system size increases. There is a suppression of intermediate cluster sizes that starts to emerge, i.e. a gap between the microscopic and macroscopic rigid clusters emerges. There exists an upper bound on the small rigid clusters that does not change with increasing system size. Interestingly, Ref. [51] argued for the absence of intermediate rigid cluster sizes when introducing a surface of cut bonds into the system based on a necessary, but not sufficient, condition for rigidity.

What does a system size-independent upper bound on the microscopic rigid cluster sizes imply about length scales? Should the macroscopic rigid cluster scenario vanish in the infinite system limit, a diverging lengthscale emerges in the sense that going from one macroscopic rigid cluster to many microscopic rigid clusters in the infinite system limit corresponds to an infinite length associated with catastrophic break-up of the one minimally rigid cluster.

How does our destabilization results for the jamming graph compare with other minimally rigid graphs, ones where local mechanical stability need *not* be obeyed as with typical rigidity percolation models? To answer this question, we generated

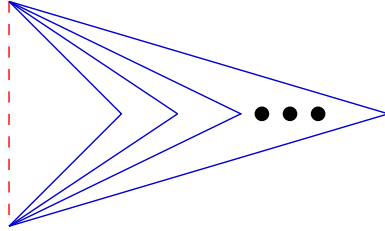


Figure 2.10: Example graph where removal of the red, dashed line leads to all remaining bonds not rigid with respect to each other (case (1) in page 42). The removal of any one blue line affects only its neighboring blue bond. The rest of the graph is unaffected (case (2) in page 42). The three black circles denote repetition of the blue hinge bonds.

minimally rigid graphs using the Henneberg Type I move (see Fig. 3) and did not enforce local mechanical stability (counter-balance) for each vertex. Therefore, we call these graphs Type I graphs. We then delete one bond randomly and compute the resulting rigid cluster probability distribution. See Figure 2.11. As with jamming graphs, the resulting rigid cluster distribution exhibits two scenarios—one with many microscopic rigid clusters (and no macroscopic rigid cluster) and another less typical scenario with at least one macroscopic rigid cluster—demonstrating a similar trend to the jamming graph case. These results, again, suggest that there are both extended and localized zero-energy modes in a minimally rigid system. However, for the Type I graphs, the gap between the macroscopic and microscopic rigid clusters does *not* emerge as clearly as compared to the jamming graph at similar system sizes.

This difference between between the jamming graph and the Type I graph could be due to the connectivity of the Type I graphs, which is less constrained than the jamming graphs. See Figure 2.12. In particular, the fraction of vertices with just two bonds is about 59 percent. The removal of either bond removes the possibility of that particular vertex participating in any rigid cluster of at least size three. While for the jamming graph, the removal of a bond does not prevent the neighboring vertex of now two or more neighbors from taking part in another local rigid cluster. In other words, the rigid cluster structures are not as local as in the jamming graph such that one may have to go to much larger system sizes to observe a gap in the rigid cluster

sizes. Interestingly, Goodrich and collaborators [51] did not observe a sudden loss of rigidity for a subsystem size below some lengthscale for bond-diluted hexagonal lattices—a standard model for two-dimensional rigidity percolation—where vertices of coordination number two are allowed. As with Type I graphs, it may be that one must go to much larger system sizes to see a gap emerge.

Also, note that the coordination number distribution for the jamming graphs exceeds 6 (Fig. 12). Indeed, the kissing number (i.e. the contact number or number of neighbors) for a monodisperse disc packing is 6 and it is 12 for a three-dimensional monodisperse sphere packing. In the repulsive soft disc simulations, the size distribution is typically bidisperse (two sizes), where the ratio of the two radii is 1.4 so as to obtain disordered packings [5, 6]. However, one also obtains a jamming transition with a polydisperse size distribution. The polydispersity would alter the upper bound of the coordination number distribution, which is nonuniversal, but would not alter the important universal properties of an average coordination number of four and that each particle is enclosed by a triangle by at least three of its neighbors at jamming.

After deleting one bond, let us briefly discuss how the system restabilizes mechanically (or not) with the random addition of one bond. If the added bond is within one rigid cluster, then the bond is redundant and the graph does not restabilize mechanically. However, if the added bond is between two rigid clusters, then it is an independent constraint such that the graph becomes minimally rigid and, therefore, must restabilize mechanically, i.e. there is only one rigid cluster. In terms of a lengthscale affected by the perturbation, if the destabilized system is made up of many microscopic rigid clusters, the lengthscale affected by the perturbation is of order the system size, i.e. it is infinite in the infinite system limit, since the system goes from many microscopic rigid clusters to one macroscopic rigid cluster with the addition of one bond.

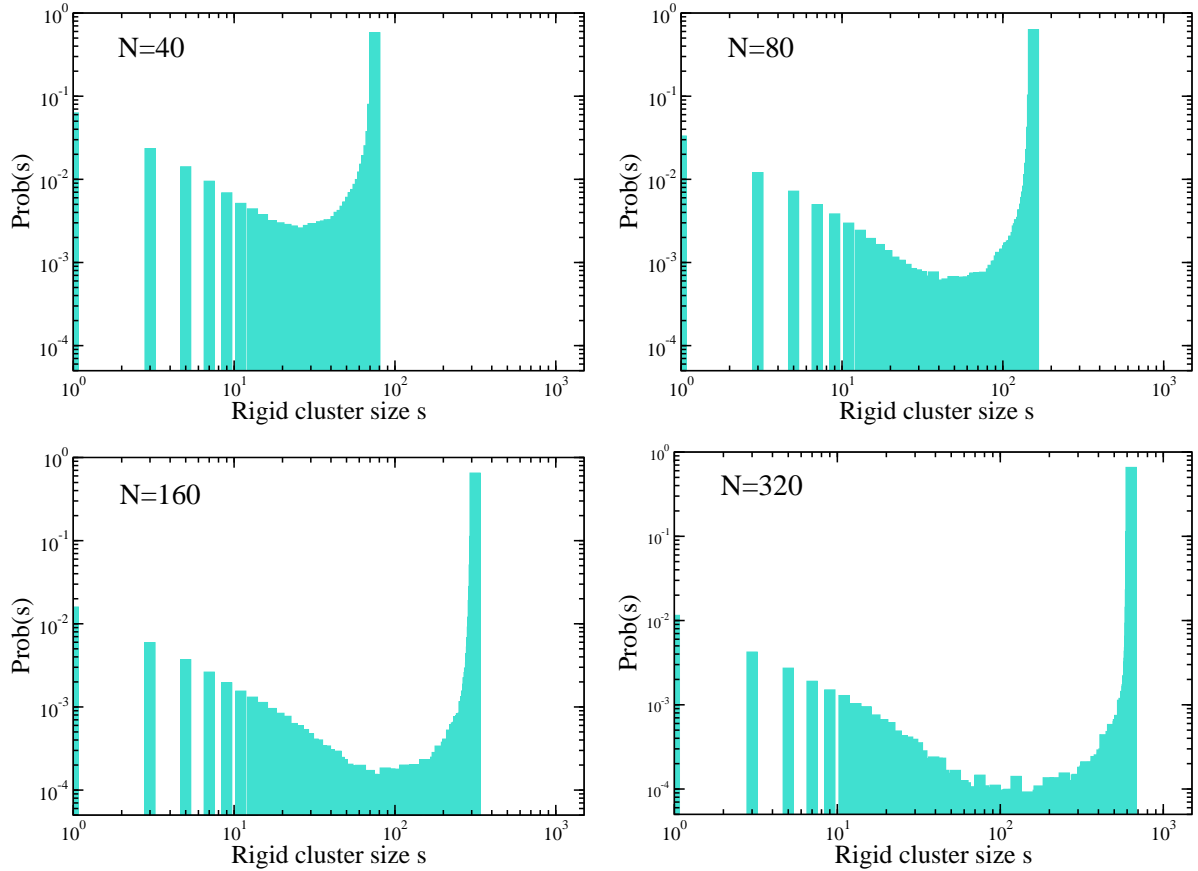


Figure 2.11: Plot of $Prob(s)$, the probability for a bond to participate in a rigid cluster of size s after one bond is deleted from the minimally rigid graphs generated by Henneberg Type I moves only. The different graphs represent different system sizes.

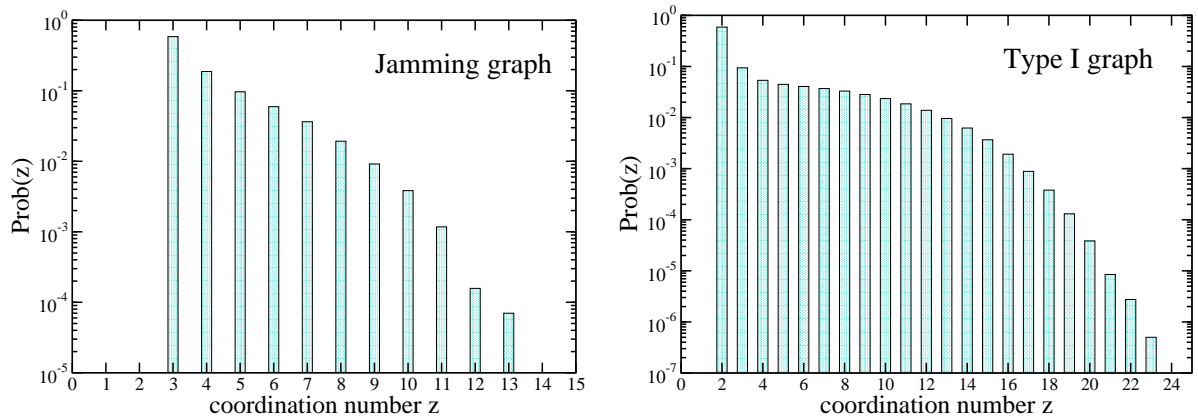


Figure 2.12: Plot of $Prob(z)$, the probability for a site to have z neighbors, for the jamming graphs (left) and the graphs generated using Henneberg Type I moves (right). For both plots, $N = 40$.

2.3.2 Hyperstatic: Randomly adding and deleting more than one bond

We begin with a jamming graph and randomly add some number of bonds, A . The graph is no longer minimally rigid, i.e. it is now hyperstatic. This action allows us to study systems that are “above” jamming where the macroscopic rigid clusters survive at least one bond deletion. We can then randomly delete (different) bonds from this hyperstatic graph and investigate how the system destabilizes mechanically. We may then be able to identify a lengthscale that decreases from the system size at jamming to some lengthscale smaller than the system size as a result of randomly deleting D bonds.

For a concrete example, consider adding eight redundant bonds to a jamming graph with $N = 40$. For 100,000 realizations, the random removal of one bond does not create more than one rigid cluster, i.e. the system is still rigid globally. The random removal of two bonds creates a few small rigid clusters in addition to the macroscopic rigid cluster with a gap in between. See Figure 2.13. When three bonds are randomly removed, however, we observe more of a qualitative change in the rigid cluster size distribution. The gap between microscopic rigid clusters and macroscopic rigid clusters closes. The concept of a single system with microscopic rigid clusters distinct from macroscopic rigid clusters no longer makes sense. We are now beginning to observe extended break up of the system. The gap size just before the extended break-up sets a size scale, $s^\#$. This size scale can be easily converted to a lengthscale via $s^\# \sim (l^\#)^2$ in two dimensions (assuming compactness).

How does $s^\#$ scale with N and with distance to the rigidity transition? We define $\epsilon = \frac{A}{N}$ to describe the distance to the transition. More specifically, since $\langle z \rangle = \frac{2}{N_f}(2N_f - 3 + A)$, with N_f representing the final number of vertices in the graph after counter-balancing, then

$$\langle z \rangle - 4 + \frac{6}{N_f} = \frac{4}{3}\epsilon, \quad (2.4)$$

where we have included the $1/N_f$ correction in the location of the transition [15, 80] and used $\frac{N}{N_f} = \frac{2}{3}$. For fixed ϵ , we observe that $s^\#$ increases with increasing N until beginning to reach a plateau that is independent of system size. We also observe that as ϵ decreases, $s^\#$ increases, though it will ultimately be cut-off by the system size. In other words, $s^\#$ is behaving as a size scale near a critical point. See Figure 14.

To test this hypothesis, we measure $s^\#$ as a function of ϵ for several system sizes and attempt finite-size scaling via the following route. Let $l \sim \epsilon^{-\nu}$, where l is some underlying diverging lengthscale in the system. If the observed diverging lengthscale, $l^\#$, is due to the underlying diverging lengthscale, then $l^\# \sim \epsilon^{-\rho}$ such that

$$l^\# = l^{\rho/\nu} f(l^{1/\nu} \epsilon), \tag{2.5}$$

with $f(y)$ as some universal scaling function. For the cut-out subsystem analysis with either free or fixed boundary conditions, $\nu = 1$. If we assume this and set $\rho = \nu$, then we do not obtain a good scaling collapse. A more recent discovered diverging lengthscale, l_c , associated with the localization of phonon modes in floppy networks, results in $\nu = 1/2$ [57, 81]. If we, again, assume $\rho = \nu$, we do not obtain a good scaling collapse. We also tried the two remaining combinations of $\nu = 1, \rho = 1/2$ and $\nu = 1/2, \rho = 1$ and did not obtain good collapse. However, with $\nu = 1/3$ and $\rho = 1/2$, we do obtain a good scaling collapse. See Figure 14. While this data is suggestive of perhaps a new diverging lengthscale in the system associated with point perturbations via $\nu = 1/3$, this possibility may be ruled out by the study of larger system sizes.

It is interesting to note that mean-field correlation length exponents of $1/4$, $1/2$, and 1 exist in disordered systems [20, 49, 50, 57, 81], while a correlation length exponent of $1/3$ is presumably less common. Incidentally, while $\nu = 1/4$ (and $\rho = 1/2$) is not as good a collapse as with $\nu = 1/3$, it cannot be ruled out at this stage. However, we can conclude that $\nu = 1, 1/2$ and/or $\rho = 1, 1/2$ does not lead to sufficient collapse for at least the system sizes we study.

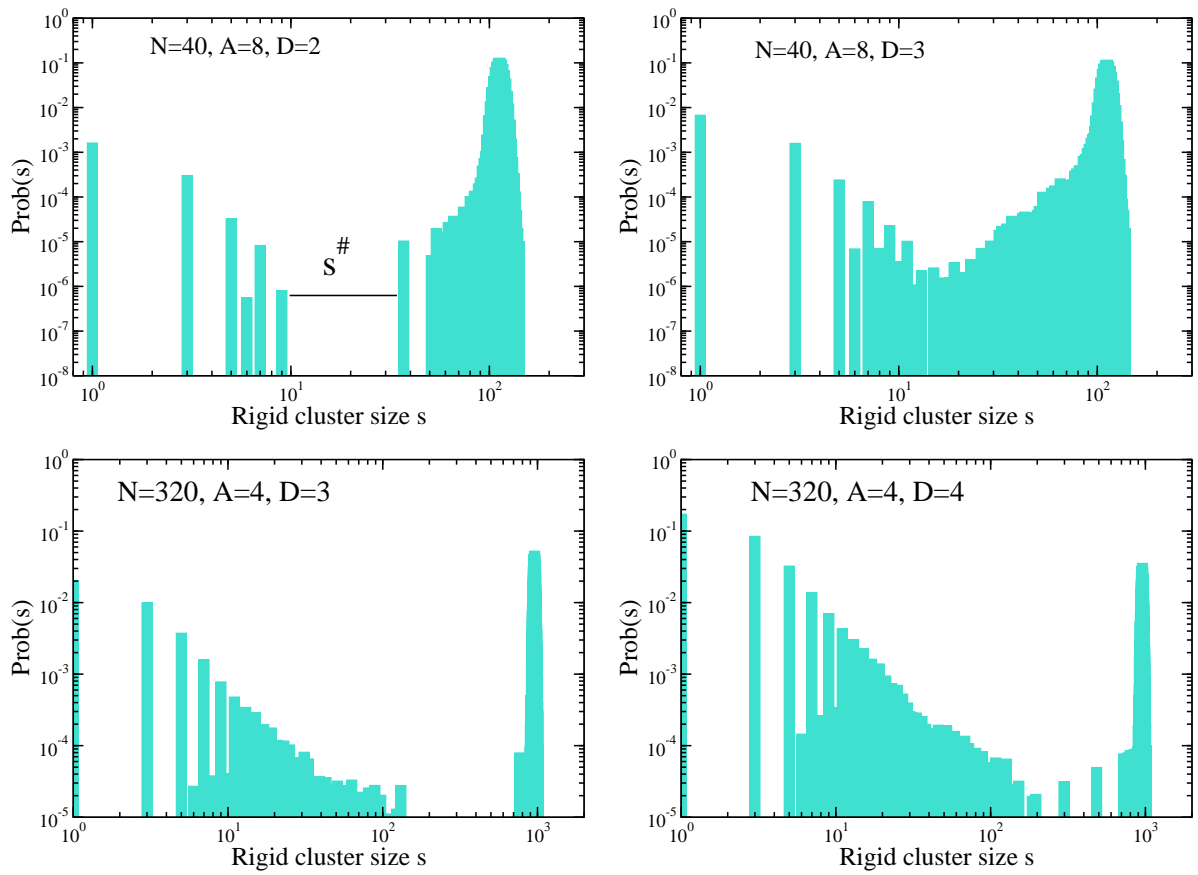


Figure 2.13: Plot of $Prob(s)$, the probability for a bond to participate in a rigid cluster of size s after A bonds are randomly added to the jamming graph and then D bonds are randomly deleted. Two different system sizes are shown.

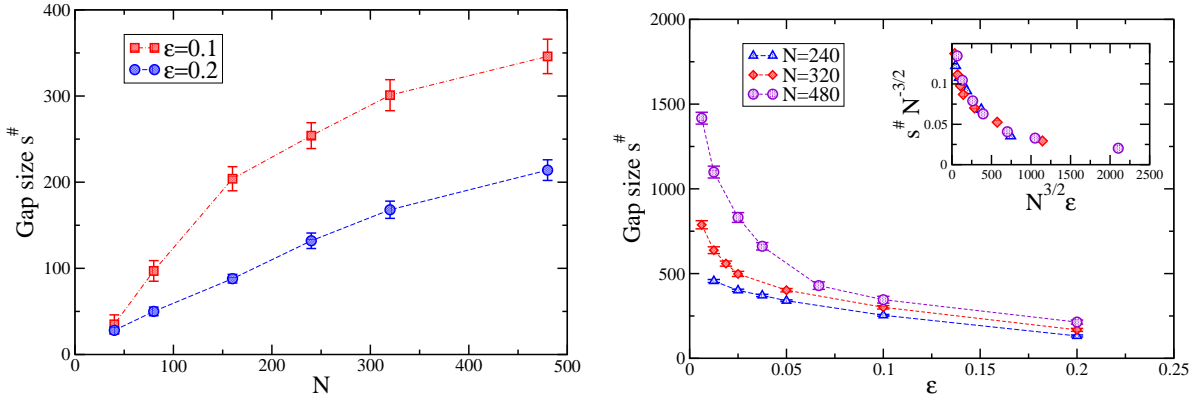


Figure 2.14: Left: Plot of the gap size $s^\#$ as a function of N for fixed $\epsilon = \frac{A}{N}$. Right: Plot of $s^\#$ as a function of ϵ for different system sizes. The inset is a finite-scaling scaling collapse obtained with $\nu = \frac{1}{3}$ and $\rho = \frac{1}{2}$. All dashed lines are guides for the eye.

2.4 Discussion

We have presented an algorithm for the spatially local construction of jamming graphs. Jamming graphs represent the contact geometry of frictionless, repulsive soft discs in two dimensions at the onset of mechanical rigidity. In other words, they contain both the property of local mechanical stability and the necessary and sufficient condition for minimal rigidity via the Henneberg construction. Since the bonds represent contacts between particles/vertices, the jamming graph is planar. Varying the construction of these (and related) graphs allows us to turn on/off different properties of particle packings at/near the onset of rigidity in a controlled way to ultimately form a more concrete and comprehensive picture of jamming.

Our construction of jamming graphs begs at least three immediate extensions of study. For the first extension, if one associates a disc with each vertex and each bond dictates the contact between two discs, then we can potentially analyze the question of whether or not there exists a unique packing fraction at the onset of rigidity in the infinite system limit [6, 72, 82, 83, 84]. Indeed, there have been a number of different definitions of the onset of jamming ranging from the random closed packing (RCP) point [6, 85] to a maximally jammed state [82] to a jamming line [83, 84].

To address this issue, we can create a physical realization of discs from a jamming graph using the circle packing theorem [86]. The circle packing theorem states that for every connected simple planar graph G there exists a circle packing in the plane whose intersection graph is isomorphic to G . There are more strict conditions for uniqueness as such and these will be explored. Note that to more readily associate a jamming graph with a disc packing, we will allow for a polydisperse size distribution of discs. While we can immediately explore this issue in two dimensions where both Laman's theorem is exact and the circle packing theorem holds, it would be interesting to extend the jamming graph to three dimensions and higher. It turns out that the three-dimensional version of Laman's theorem for some networks are essentially exact [87]. Higher-dimensional extensions of the circle packing theorem would indeed be more challenging.

As for the second immediate extension, with jamming graphs we can search for interplay between global mechanical stability and local mechanical stability since we can easily turn off/on local mechanical stability. This on/off switch allows us to compare the mechanics of fixed connectivity networks from rigidity percolation [60, 61] with repulsive particle packings [54, 57, 77, 88]. While local mechanical stability may not play as much of a role at the transition (other than suppressing fluctuations [50]), it will certainly play a role in particle rearrangements above jamming, where local mechanical stability is also required. For instance, if particle chains form as a result of some perturbation, the chain should buckle so that particles having two contacts will ultimately have at least three contacts with the appropriate geometry. Such particle rearrangements above jamming can also be studied using jamming graphs with the removal and addition of bonds. For instance, if the breaking of a contact results in a vertex not being counter-balanced, with some input of force information [79, 89, 90, 91], a sequence of moves can be generated to regain the local mechanical stability while ensuring that the graph remain hyperstatic.

For the third immediate extension, local rules governing a system may lead to a

field theory, should one exist. And while there is not necessarily consensus on a field theory for jamming [92, 93], our spatially local construction of the jamming graph may provide insight for building a modified field theory for a system with both local and global constraints. Such a framework may accelerate the quest to determine how to classify the various constraints in terms of potentially different universality classes. For instance, enforcing only the local k -core constraint leads to one type of phase transition, while the counter-balance constraint leads to another [20, 94]. And while such attempts are not currently appreciated in the field, a classification system based on constraints will ultimately emerge.

For instance, the notion of constraints changes when one deviates from frictionless, repulsive soft discs. Ellipsoidal particle packings may or may not be isostatic at the onset of rigidity depending on which degrees of freedom can be accessed [95, 96]. It turns out that one can also extend Laman's theorem in two dimensions to systems with other degrees of freedom [66] and, correspondingly, extend the Henneberg construction. Such an extension of the jamming graph may, therefore, prove useful for understanding the onset of rigidity for nonspherical particles. As for frictional systems, while the history of the contact information may be difficult to incorporate into an equivalent jamming graph, one can extend the pebble game (to a (3,3) pebble game) to map out the rigid clusters of frictional packings to compare with frictionless packings [97]. These endeavors (and others) will help form a concrete framework for the onset of rigidity in disordered systems.

After constructing these jamming graphs, the deletion of one bond allows us to study how the system destabilizes. In the system sizes studied, there exist two scenarios, one where the removal of the bond leads to catastrophic collapse of the single rigid cluster with many microscopic rigid clusters (an extended zero-energy mode) and the other where at least a macroscopic rigid cluster survives (a localized zero-energy mode). As the system size increases, the probability of the localized zero-energy mode decreases. It would be interesting to prove whether or not this probability vanishes in

the infinite system limit. Particularly in two dimensions, there is a wealth of mathematical literature on minimal rigidity to potentially go beyond heuristic arguments and numerics.

As opposed to uncovering a diverging lengthscale in surface versus bulk effects [49, 50, 51, 52, 54], we have potentially uncovered a new diverging lengthscale in the rigid phase in response to random bond deletion. With a correlation length exponent close to $1/3$, it appears that this new lengthscale is not related with the introduction of a force monopole in the particle packings [56]. However, once forces are introduced, and/or the contact geometry is allowed to rearrange as the system responds to the point perturbation, then one should presumably obtain the prior result. Again, the ability to build upon the jamming graph by incorporating further detail bit-by-bit will allow us to identify the properties ultimately dictating a particular behavior or response.

Chapter 3

Constraint Percolation on Hyperbolic lattices

3.1 Introduction

Geometry plays a key role in driving physical processes in such different physics fields as relativity, cosmology, quantum field theories, and condensed matter. In condensed matter systems specifically, the effect of geometry on the nature of a phase transition is of interest. In particular, Hyperbolic spaces that possess a constant negative curvature of -1 have been applied recently in several condensed matter models, namely the Ising model and percolation. Why consider hyperbolic spaces? Hyperbolic geometry connects to properties of mean field theory, or Bethe lattices, with the same nonvanishing ratio of surface to volume of compact structures as the size of the lattice scales to infinity. The relevance of loops, moreover, are small. Accordingly, hyperbolic lattices provide a test bed for studying phase transitions in a geometry that interpolates between Bethe lattices and Euclidean lattices. Hyperbolic lattices are also interesting from a jamming and glassy physics perspective because they provide a natural mechanism in two dimensions to frustrate global crystalline order and allow for a more tractable model to study glass transition and jamming in two dimensions [98].

We use hyperbolic tessellations here to study k -core and force balance percolation models. Recall that k -core percolation is constraint percolation model where occupied sites having less than k occupied neighboring sites are pruned starting with an initial random and independent occupation of sites. This pruning is done consecutively until all occupied sites have at least k occupied neighboring sites. In mean field, k -core percolation resembles some properties of a mixed phase transition, i.e. discontinuity in the order parameter and a diverging length scale, as in the jamming transition. And yet k -core percolation on Euclidean lattices appears exhibit either a continuous phase transition in the same universality class as unconstrained percolation or no transition ($p_c = 1$). So we ask the question: What is the nature of the k -core percolation transition on hyperbolic lattices? Will the transition behave more like what is computed on the Bethe lattice, or not?

As you will soon discover, many of the numerical techniques developed for the analysis of the phase transition from not-spanning to spanning in unconstrained percolation are not as readily applicable on hyperbolic lattices given the strong boundary effects. As a means of comparison, we also investigate counter-balance percolation on hyperbolic lattices. Counter-balance percolation is another constraint percolation model [94] in which each site is first occupied with some occupation probability p . Then, if an occupied site is not surrounded by neighboring occupied sites such that local mechanical stability can be guaranteed, the occupied site is removed from the lattice. This procedure is repeated until all occupied sites obey the occupation constraint. This model was studied in two- and three-dimensions. Numerical simulations suggested strongly signs of a discontinuous transition in the standard order parameter (i.e. the fraction of sites participating in the spanning cluster) which also occurs in jamming. And yet numerical simulations also suggested that there exists a correlation length scale diverging faster than any power-law, which is different from jamming with numerics suggesting the more standard power-law diverging correlation length [5].

So we expect counter-balance percolation to be discontinuous on various Euclidean lattices. A mean field theory of counter-balance percolation is not possible because spatial information is encoded in the constraints. Studying counter-balance percolation on hyperbolic lattices will allow us to work towards a mean field theory without giving up the spatial constraints. We expect counter-balance percolation to exhibit a discontinuous percolation transition on hyperbolic lattices since it already appears to be in the presence of many loops. This behavior should give us something to compare against when trying to determine whether or not k -core percolation exhibits a discontinuous transition on hyperbolic lattices. This information will help us better understand the nature of k -core percolation, which, again, is a minimal model of jamming to help lay the foundation for microscopic understanding of the jamming transition.

The remainder of this chapter is organized as follows: We will study several properties of k -core percolation models for $k = 1, 2, 3$, and counter-balance percolation on hyperbolic tessellations. We present in Section 2 details of the hyperbolic lattice and various percolation algorithms. In Section 3 we present a theoretical proof that the threshold for counter-balance percolation is strictly less than one for most of the tessellations. This section is a bit technical and can be skipped by the reader should their interest be more in the nature of the phase transition. We present our numerical results in Section 4, where we study the order parameter, the crossing probability, and the cluster size distribution. We summarize and discuss the implications of our results in Section 5.

3.2 Model and methods

The key step in the simulation process is to construct a hyperbolic lattice. We do this by implementing the algorithm described in detailed in Ref. [99]. In the construction of a $\{P, Q\}$ hyperbolic lattice, where, again, P denotes the number of sides of each

polygon and Q denotes how many polygons meet at a vertex, the central polygon is built first, this is the first layer. Then by translations and rotations of the central polygon, the second layer is built. This process is followed recursively until a desired number of layers are built. An l -layer is composed of those polygons that do not belong to an m -layer for $m < l$ and share an edge or vertex with a polygon in the $(l - 1)$ -layer. The algorithm makes use of the *Wierstrass model* for hyperbolic geometry, where points lie on the upper sheet of the hyperboloid $x^2 + y^2 - z^2 = -1$. Consequently, rotations and translations are given by 3×3 Lorentz matrices. The Wierstrass is related to the Poincare model through the stereographic projection toward the point $(0, 0, -1)^t$ given by

$$\begin{pmatrix} x \\ y \\ z \end{pmatrix} \rightarrow \frac{1}{1+z} \begin{pmatrix} x \\ y \\ 0 \end{pmatrix}. \quad (3.1)$$

The exponential growth of number of vertices with respect to the number of layers constrains severely the number of layers used in the simulations. Typically we simulate

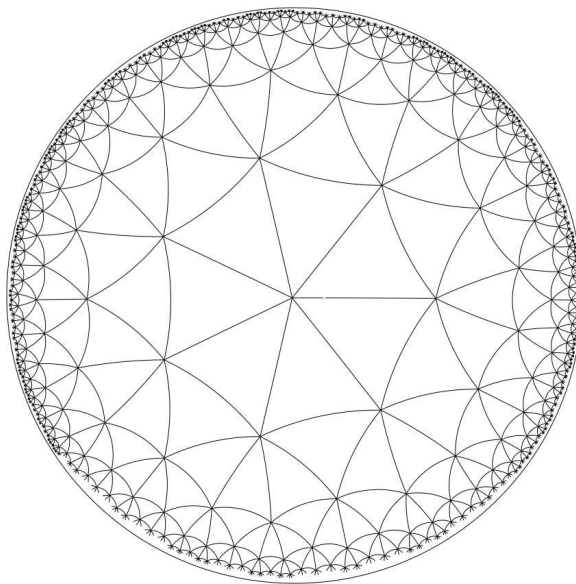


Figure 3.1: $\{3, 7\}$ tessellation on the Poincare disk.

around 10 layers. This is comparable to the recent work by Gu and Ziff studying ordinary percolation on hyperbolic lattices [100]. Ziff is considered a leader in the world of numerical analysis of percolation. We impose fixed boundary conditions. Recent work on implementing periodic boundary conditions in certain tilings may ultimately be investigated [98]. However, the sets of hyperbolic tilings that can be used using the methods in [98] have less than 30000 sites due to a lack of knowledge of all possible normal subgroups of a given Fuchsian group.

Once a tessellation is created, each of its sites are occupied with probability p . For k -core percolation, we then recursively remove any occupied site (excluding boundary sites) that has less than k occupied neighboring sites. For counter-balance percolation, we recursively remove any occupied sites (excluding boundary sites) that are not enclosed by a triangle of neighboring occupied sites, i.e. those sites that are not mechanically stable. We do this until all occupied sites obey the imposed constraint. We have numerically tested on around one million runs, that the order in which we check the counter-balance constraint does not affect the final configuration, i.e. that the model is abelian. It has been also argued that the k -core model is abelian [101].

We then use the Hoshen-Kopelman algorithm to identify the clusters and their respective sizes. To determine if a cluster is spanning, we break up the lattice into four cardinal regions: NE , NW , SW , and SE . See Figure 3.2. We regard the cluster as percolating, or spanning, when it connects either NE and SW sites or NW and SE sites, as in Ref. [100]. We then measure the probability to span, or cross for an occupation probability p and we call it $R(p)$. We also measure the number of times we check the lattice to cull occupied sites not obeying their respective constraints. This *culling time* tends to diverge near the transition.

3.3 Theoretical proof of $p_c < 1$ for some hyperbolic tillings

It has been mentioned that there exists two critical percolation probabilities, p_l and p_u for ordinary percolation on hyperbolic tillings. For our counter-balance model however, it seems there is just one critical percolation probability according to the results presented later. Let us call this probability, p_{CB} , the probability above which we have a percolating cluster. It is possible to prove that $p_{CB} < 1$ for some hyperbolic tillings $\{P, Q\}$. The proof follows two steps:

1. To establish the existence of trees on a tessellation $\{P, Q\}$ with a certain connectivity that depends on the parity of Q . For Q even we demand a connectivity $z = 6$ and for Q odd, $z = 5$.

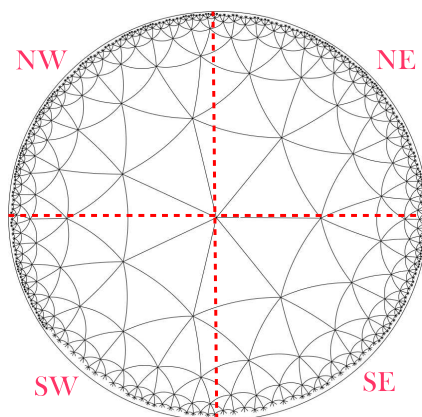


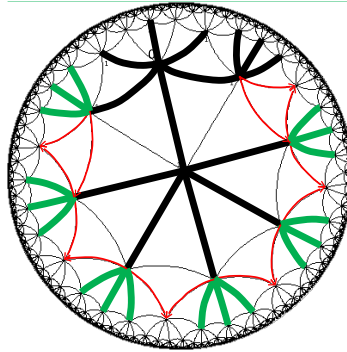
Figure 3.2: $\{3, 7\}$ tessellation on the Poincaré disk with the four boundary regions.

2. We apply a well known result of k -core percolation on trees, i.e. that the critical percolation is less than one when $k < z$. For our purposes we require $k = 5$ for Q even and $k = 4$ for Q odd. Accordingly we need to show that sites on a percolating cluster for 5-core model on those $z = 6$ trees, and Q even case, satisfy counter-balance condition. In a similar way for the Q odd case.

Let us prove each of these items in due order.

1. We need to show the existence of trees of connectivity $z = 6$ and $z = 5$ for Q even and odd, respectively. Let us suppose Q is even. It is easy to see that $z = 6$ trees cannot be built when $Q = 4, 6$ as there is not enough "space" to build such kind of trees. The case $Q = 8$ is more interesting.

Figure 3.3: Impossibility of building a tree of connectivity $z = 6$ on the $\{3, 8\}$ tessellation due to the lack of space

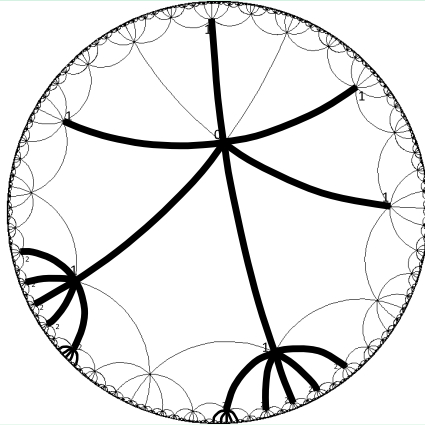


The tessellation $\{3, 8\}$ do not admit such construction because the tree overlap onto itself as illustrated in Fig. 3.3 where red arrows shows some of those positions at which the tree (green) effectively overlaps onto itself.

However $z = 6$ can be built on tessellation $\{4, 8\}$. To see this we choose a site which we call the $0th$ -generation. The first generation are the neighbors of such site. The nth -generation will be formed by those sites neighbors of the $(n - 1)th$ -generation that do not belong to a kth -generation where $k < n$. This

is illustrated in Fig. 3.4. By construction, between two adjacent *1st*-generation sites on the $z = 6$ tree there is one *2nd*-generation site which does not belong to the tree. Now between the closest sons of those *1st*-generation sites which are *2nd*-generation sites belonging to the tree, there are six *3rd*-generation sites not belonging to the tree. By construction such tree can be expanded without overlapping.

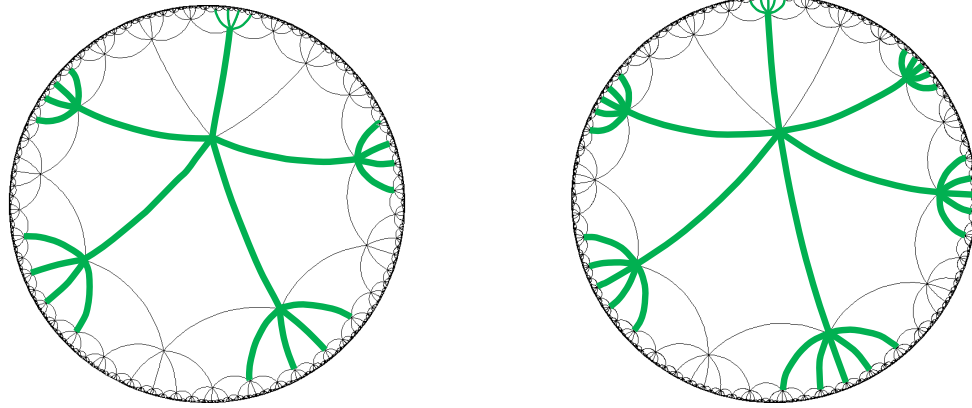
Figure 3.4: Tessellation $\{4, 8\}$ enables the construction of trees of connectivity $z = 6$



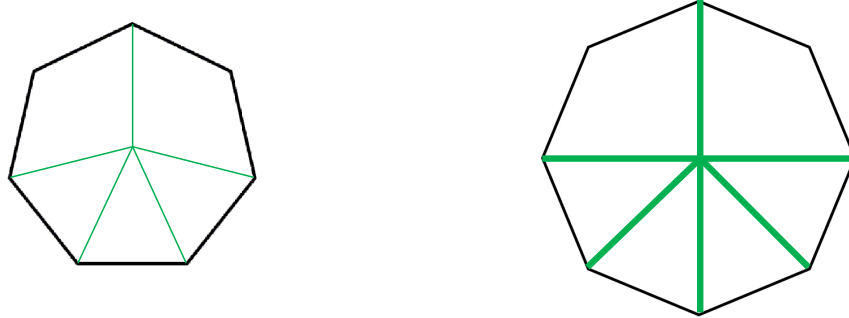
For $P > 4$ we have more vertices in each layer which gives more space to build the tree, and the same construction holds. Accordingly we can build $z = 6$ trees on tessellation $\{P, 8\}$ when $P > 3$. Likewise, it can be checked that for any P, Q even and $Q > 9$, it is possible to build a tree of connectivity $z = 6$. Analogously, it is checked that trees of connectivity $z = 5$ can be built on tessellations $\{P, 7\}$ where $P > 3$, and for any tessellation $\{P, Q\}$ where $Q > 8$ is odd. In summary those trees necessary for our proof can be built on any tessellation $\{P, Q\}$ as long as $Q > 8$ and for the tessellations $\{P, 7\}, \{P, 8\}$ as long as $P > 3$.

2. Any site of the trees built in step 1. of a $\{P, Q\}$ tessellation will be contained in a Q -gon as illustrated in Fig. 3.5.

Now let us take such Q -gons on a euclidean setting as illustrated in Fig. 3.5(c) and 3.5(d). One of the neighbors of central site is isolated from others, let us call



(a) Tree of connectivity $z = 5$ on the $\{4, 7\}$ tessellation (b) Tree of connectivity $z = 6$ on the $\{4, 8\}$ tessellation



(c) Euclidean illustration of the "central" part of the $z = 5$ tree on tessellation $\{4, 7\}$ (d) Euclidean illustration of the "central" part of the $z = 6$ tree on tessellation $\{4, 8\}$

Figure 3.5: Tree construction on the hyperbolic tessellations

it north neighbour, N . It happens that any tree of connectivity 4 (Q even case) containing site N and imbedded in those trees of connectivity $z = 5$, satisfy the counter-balance condition as indicated in Fig. 3.6.

Notice that this *triangle* condition on the central site is preserved in the hyperbolic geometry because the function that relates those polygons in different geometries preserves topology. A similar proof applies to trees of connectivity

5 embedded in those trees of connectivity $z = 6$ (Q even case).

Notice that this analysis holds for any site so we can always construct such a Q -gon with the same characteristics for any site occupied site. Now let us call p_{4c} the critical percolation probability for 4-core percolation on trees of connectivity $z = 5$ and p_{5c} such probability for 5-core percolation on trees of connectivity $z = 6$. It follows from the discussion above that $p_{CB} < p_{4c}$ for Q even, and $p_{CB} < p_{5c}$ when Q is odd (search p_{4c} and p_{5c}) at least for those tessellations where we can make the construction illustrated in Fig. 3.5.

3.4 Results

We work with tessellations $\{3, 7\}$, $\{7, 3\}$, and $\{4, 7\}$, where the first two tessellations are the most common studied [100, 102]. We study $k = 1, 2, 3$ -core percolation and counter-balance percolation on such tessellations. The order parameter, defined as S_1/N , where S_1 is the size of the largest cluster and N the total number of sites, determines the continuity/discontinuity of the transition, i.e. should it increase from zero continuously as the occupation probability p is increased, then the transition is continuous. We also study properties of the full cluster size distribution (not just the largest cluster). To independently determine where the threshold occurs, we measure the crossing probability $R(p)$ discussed below. Recall that for unconstrained

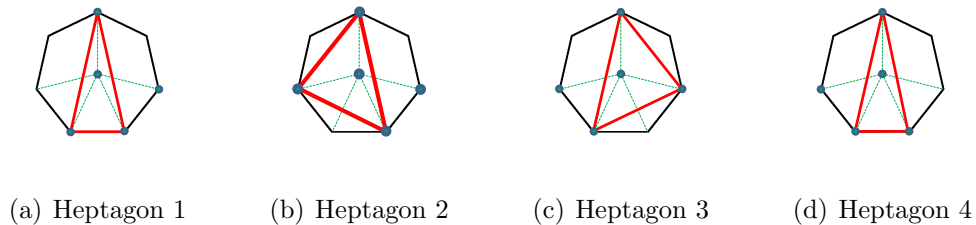


Figure 3.6: Illustration of all the possible cases of occupation for a 4-core cluster on a tree of connectivity $z = 5$

percolation on hyperbolic lattices there are two thresholds p_l and p_u , not just one.

3.4.1 Crossing probability

It has been proved that unconstrained percolation exhibits three phases on a hyperbolic lattice [103]. Specifically, for $p < p_l$ there is no percolating cluster, for $p_l < p < p_u$ there are infinitely many percolating clusters, and when $p > p_u$ there is just one percolating cluster. The existence of three phases is reflected in the crossing probability, $R(p)$. According to Ref. [100], as the number of layers tends to infinity, $R(p)$ tends to a function that in the intermediate phase is a straight line with finite slope in the infinite layer limit. If there is just one phase boundary, as with unconstrained percolation on Euclidean lattices, then in the infinite system limit $R(p)$ jumps discontinuously at the boundary from zero to one through some value of $R(p_c)$ (the Cardy crossing value) at the transition. So there would be no finite slope region in the infinite system limit.

Since $k = 1$ -core percolation removes only isolated occupied sites, it is equivalent to unconstrained percolation. We should, therefore, observe this finite slope intermediate region in the crossing probability as the number of layers tends towards infinity. This finite slope region has indeed been observed in Ref. [100] for $k = 0$ -core percolation. Fig. 3.7(a) presents the crossing probability for all four percolation models. To check for the existence of the intermediate region in $R(p)$ we extract its maximum slope M near the inflection point. We then plot the inverse of this slope as a function of the $1/\ell$ and extrapolate to the number of layers, ℓ , going to infinity limit. The results are illustrated in Fig. 3.8. The inverse of the slope, $1/M$ tends to similar values for 1-core and 2-core models. For 1-core, it tends to 0.240 and 0.223 for the 2-core model. Meanwhile $1/M$ tends to 0.131 for 3-core model. The fact that the inverse of the slope tends to -0.036 for the counter-balance model, which is much closer to zero than the three other models, is an indication that the slope tends to infinity at the transition. Consequently there should be just two phases for the counter-balance

model.

The suggestion of a finite slope regime of $R(p)$ for all three k -core percolation models suggests that there is an intermediate phase for $R(p)$. In other words, all three models behave similarly to unconstrained percolation. Of course, we have empirically chosen a function to implement the extrapolation. In Ref. [100], the maximum slope M as a function of $N(\ell)^{-0.7}$, where $N(\ell)$ is the number of vertices in a layer was used. In this work, different choices of the exponent did not affect the outcome. We also

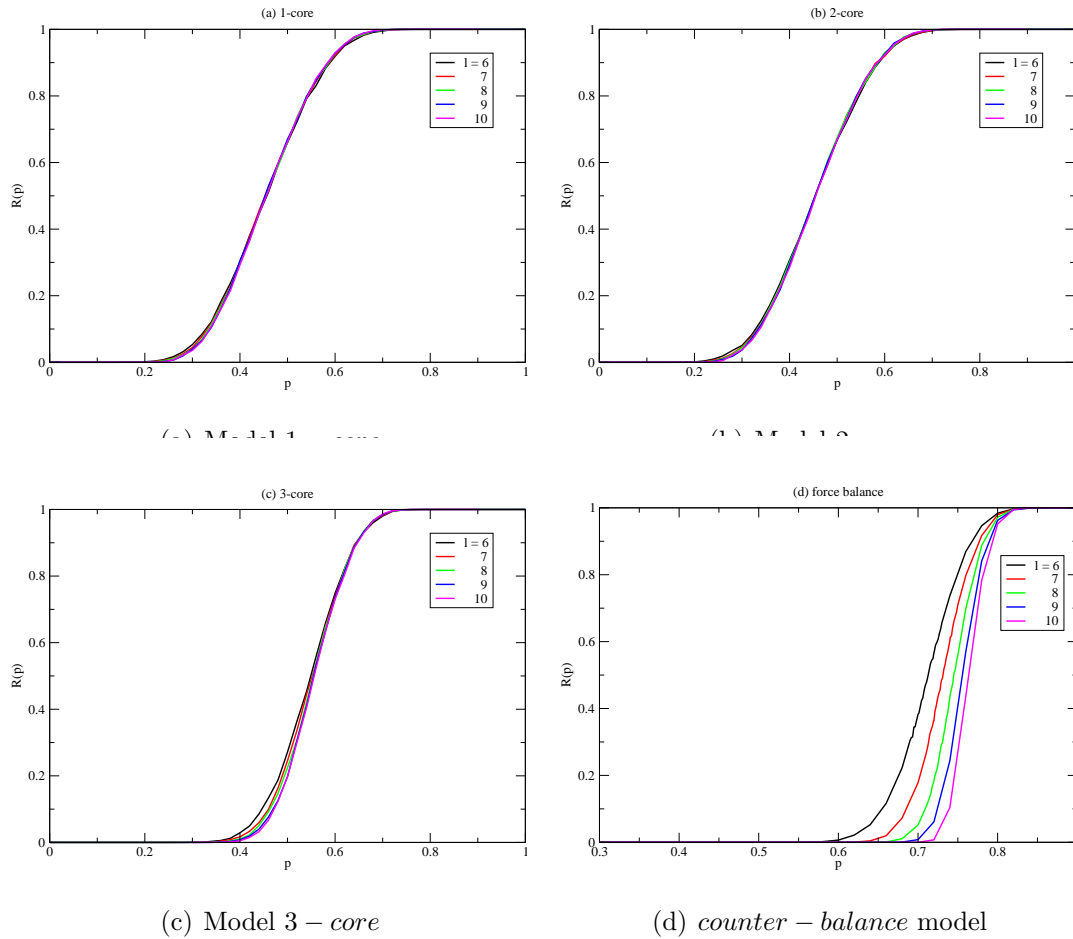


Figure 3.7: Crossing probability on $\{3, 7\}$ tessellation and different percolation models. counter-balance model apparently is discontinuous which is confirmed by the extrapolating the value of the slope with $1/l$.

tested different slightly extrapolation functions and our results remain unchanged in terms of the interpretation.

3.4.2 Order Parameter

For unconstrained percolation on Euclidean lattices the order parameter, P_∞ , is a continuous function of p . Since $k = 1, 2$ -core models are equivalent to unconstrained percolation in terms of the transition, they should behave similarly. While the order parameter in $k = 3$ -core on the Bethe lattice jumps discontinuously at the transition, on Euclidean lattices it does not. For counter-balance percolation on two- and three-dimensional Euclidean lattices, the order parameter jumps discontinuously at the transition. We present $P_\infty(p)$ for different layer numbers for the four different models on the $\{3, 7\}$ tessellation in Fig. 3.9.

Since any differences between the curves is not clear by eye, we perform a similar extrapolation to what was used for the study of $R(p)$. We measure the maximum slope of each curve and plot the inverse of the maximum slope, $1/S_0$ with respect to $1/l$. Should the transition be continuous, then the y -intercept of $1/S_0$ to be greater

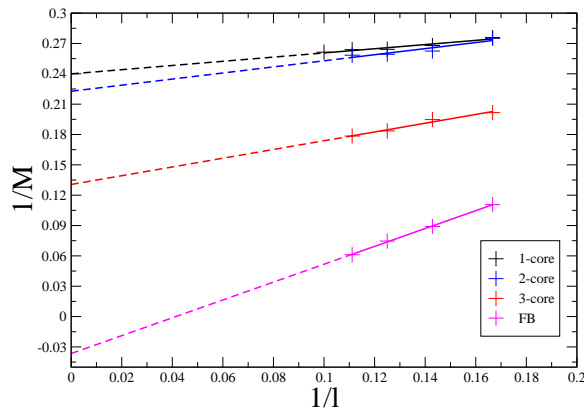


Figure 3.8: Inverse slope of Crossing probability, $1/M$, tendency on $1/l$ for different models on the $\{3, 7\}$ lattice. For 1-core model $1/M$ tends to 0.240, for 2-core to 0.223, for 3-core to 0.131, and for counter-balance (CB) to -0.036 indicating M is tending to ∞ as l tends to ∞ .

than zero. Should the transition be discontinuous, then the y -intercept should vanish. We found that the 1-core and 2-core models have a very similar limiting value, $1/S_0 = 0.0953$ and $1/S_0 = 0.0996$, respectively. The y -intercept tends to $1/S_0 = 0.0686$ for the 3-core case, which is different than the previous two cases, but still non-zero. The k -core models may indeed be continuous phase transitions for the $\{3, 7\}$ tessellation. For the counter-balance model, the same extrapolation method yields tends to a negative value as shown in Fig. 3.10 that is very close to zero. This result may indicate that counter-balance percolation belongs to a discontinuous phase transition. This

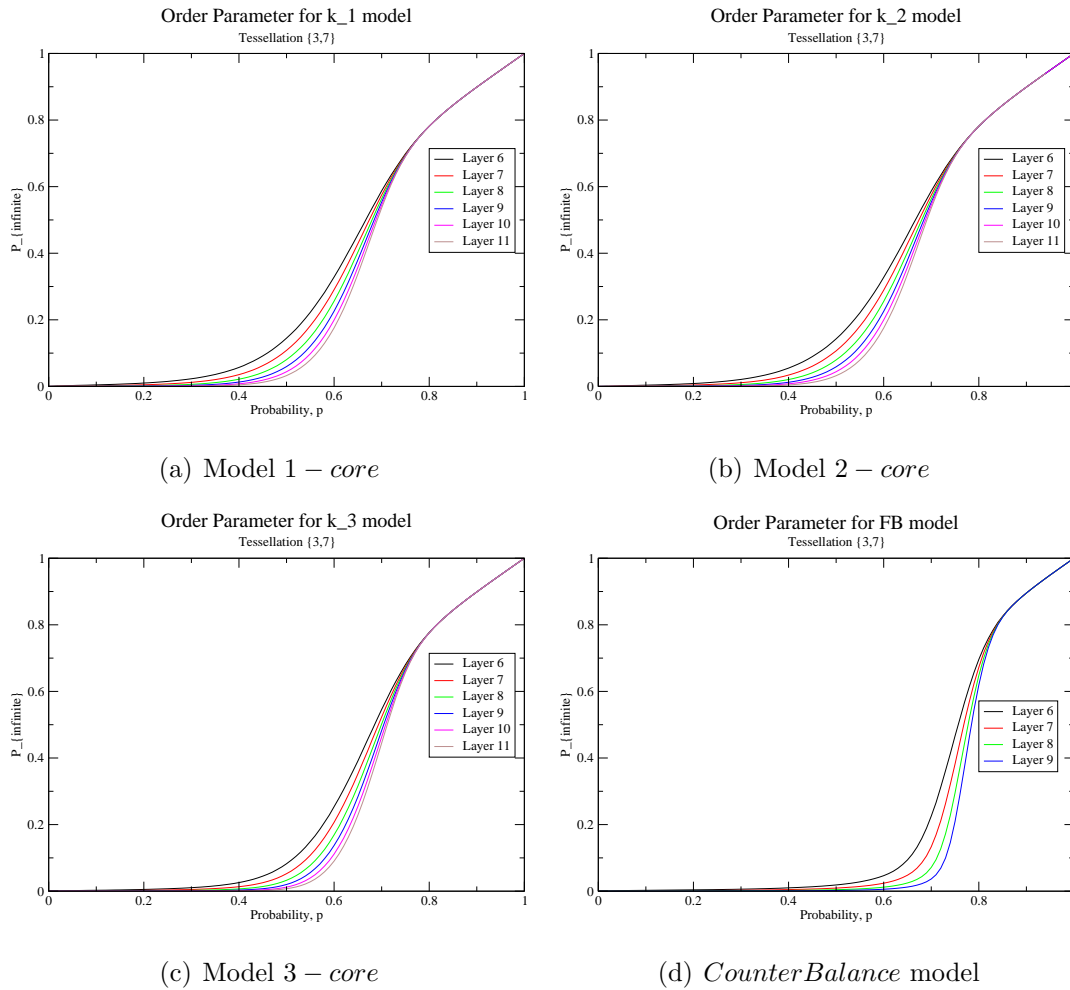


Figure 3.9: The order parameter for the different models on the $\{3, 7\}$ lattice.

result is expected since it is discontinuous on Euclidean lattices as well.

3.4.3 Cluster sizes

For unconstrained percolation on Euclidean lattices the cluster size distribution, $\rho(s)$, for cluster size s falls off exponentially below $p_u = p_l$, becomes power law at $p_u = p_l$, and is believed that $\rho(s) \sim \exp(-\eta(p)s^{1-1/d})$ for $p > p_u$ [18]. One might therefore expect that $\rho(s) \sim \exp(-s)$ for $p > p_u$ for a hyperbolic lattice since it shares some similar properties with the Bethe lattice. The Bethe lattice is a high-dimensional graph in the sense that the probability of forming a loop is zero. We now present the histogram for the cluster sizes (which has the same scaling as $\rho(s)$) for the various models. We observe for all the k -core models and the counter-balance the following behavior. Below some probability, p_{clus} , the histogram is concave as seen in Fig. 3.11. Then the histogram becomes power law when $p > p_{clus}$ with an additional peak at the end of the distribution. Accordingly, for $p > p_{clus}$ the histogram scales as $s^{-\tau}$, except for the peak.

We have the following values for τ for the different models. For the k -core models $\tau = 2.09, 2.07, 2.04$ for $k = 1, k = 2$, and $k = 3$ -core models respectively. These values agree with earlier simulations of unconstrained percolation on the hyperbolic

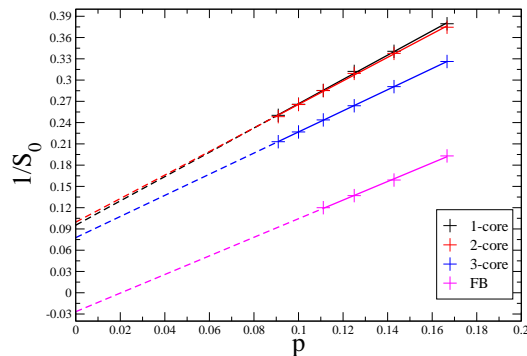
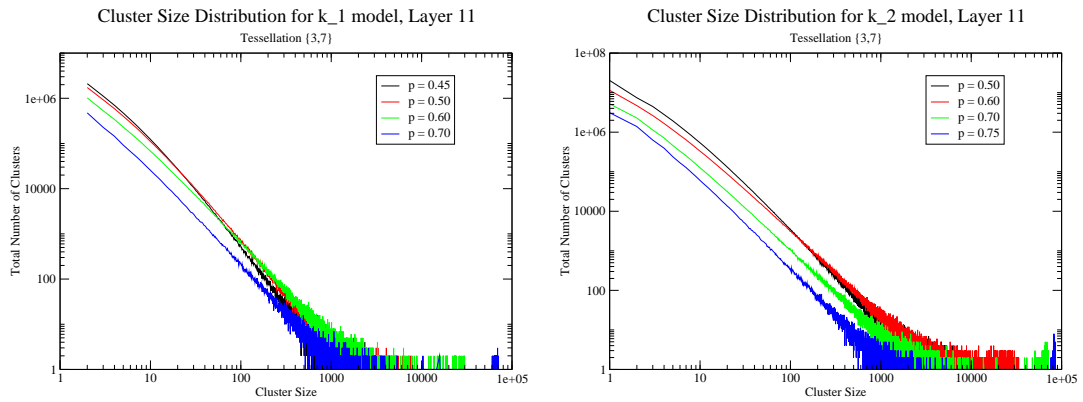


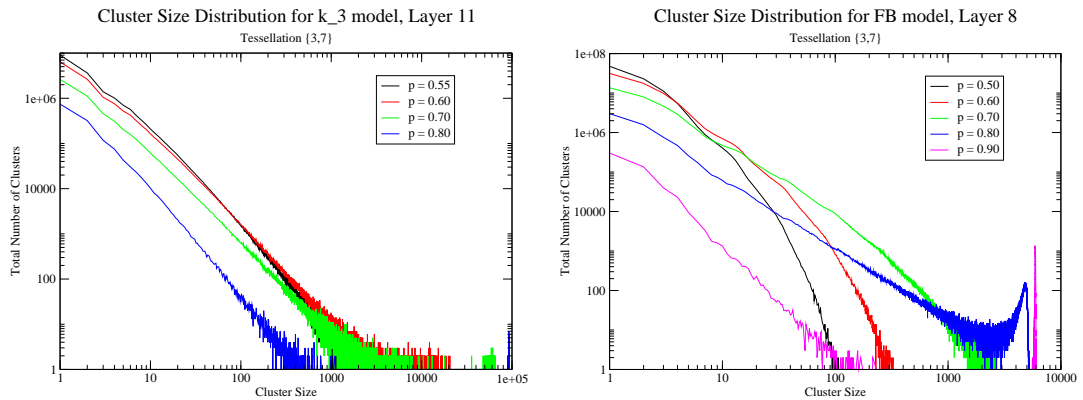
Figure 3.10: The inverse of the maximum slope of the order parameter as a function of ℓ for the different models on the $\{3, 7\}$ lattice.

lattice [102]. For the counter-balance model, $\tau = 1.76$. Again, the counter-balance model appears to be a different phase transition from the k -core models. More importantly, the data suggests that, again, $k = 3$ -core behaves similarly to unconstrained percolation, which is the same observation for $k = 3$ -core on Euclidean lattices.

For the $\{3, 7\}$ tessellation, the $k = 1$ -core histogram becomes more broad with increasing occupation probability and remains broad at larger p . The $k = 2, 3$ -core



(a) Cluster size distribution for the 1-core model and $l = 11$. (b) Cluster size distribution for 2-core model and $l = 11$.



(c) Cluster size distribution for 3-core model and $l = 11$. (d) Cluster size distribution for Counter balance model and $l = 8$.

Figure 3.11: Cluster size histograms (as opposed to distributions) for different models and the $\{3, 7\}$ lattice. 10000 samples were implemented for each data set.

models exhibit similar behavior. However, the small system sizes limit our interpretation.

For the counter-balance model, the cluster size histogram becomes broad at $p \approx 0.8$ with an additional peak at $s \approx 5000$ (for $l = 8$). An additional peak is not observed in the k -core models. Is this peak robust at larger system sizes? If $p_u < 1$, then this graph could be an indication that counter-balance is different from k -core in the hyperbolic plane. Larger system sizes are being studied. Moreover, at even larger p , the cluster size distribution appears to scale differently than the $p = 0.8$ curve, which is different from the k -core model results.

3.4.4 Culling time

The culling time is the number of sweeps through the lattice to complete the culling/removal process for those occupied sites not obeying the respective constraints. On Euclidean lattices, the culling time for $k = 3$ -core and counter-balance percolation increases near the percolation transition due to an increasing lengthscale in the distance over which the removal of one occupied site triggers the removal of other occupied sites.

In Fig. 3.12, we observe the culling time for tessellation $\{3, 7\}$, for $k = 2, 3$ -core and counter-balance models. Note that for $k = 1$ -core it just takes one sweep of the lattice to eliminate sites not satisfying the constraint so there is no diverging lengthscale. According to Fig. 3.12, there is a peak in the culling time T as a function of p . Note that the position of the peak for the k -core models does not move and presumably yields an estimate for p_l . Accordingly, on $\{3, 7\}$ for the 2-core model, $p_{2l} \approx 0.28$, and for the 3-core model $p_{3l} \approx 0.45$. However, for counter-balance model the peak is increasing with the number of layers. We obtain the extrapolated $p_{CB}^* \approx 0.837$ when scaling p_{CB} as l^{-1} . While there are the two regimes of many spanning clusters and one unique spanning cluster for $k = 1$ -core, it is not obvious that these two regimes exist for $k = 2, 3$ -core. A peak that remains broad in the infinite system limit may be indicative of the two regimes.

3.4.5 Debate about p_u

There exist three phases for unconstrained percolation on a hyperbolic lattice [103]. For $p < p_l$ there is no percolating cluster, for $p_l < p < p_u$ there are infinitely many percolating clusters and for $p_u < p$ the infinite number of percolating clusters join form one. There is not clear consensus, however, about how to numerically calculate p_l and p_u . According to Ref. [102] p_l can be measured as the probability above which there is a cluster connecting boundary points to the center. And p_u can be

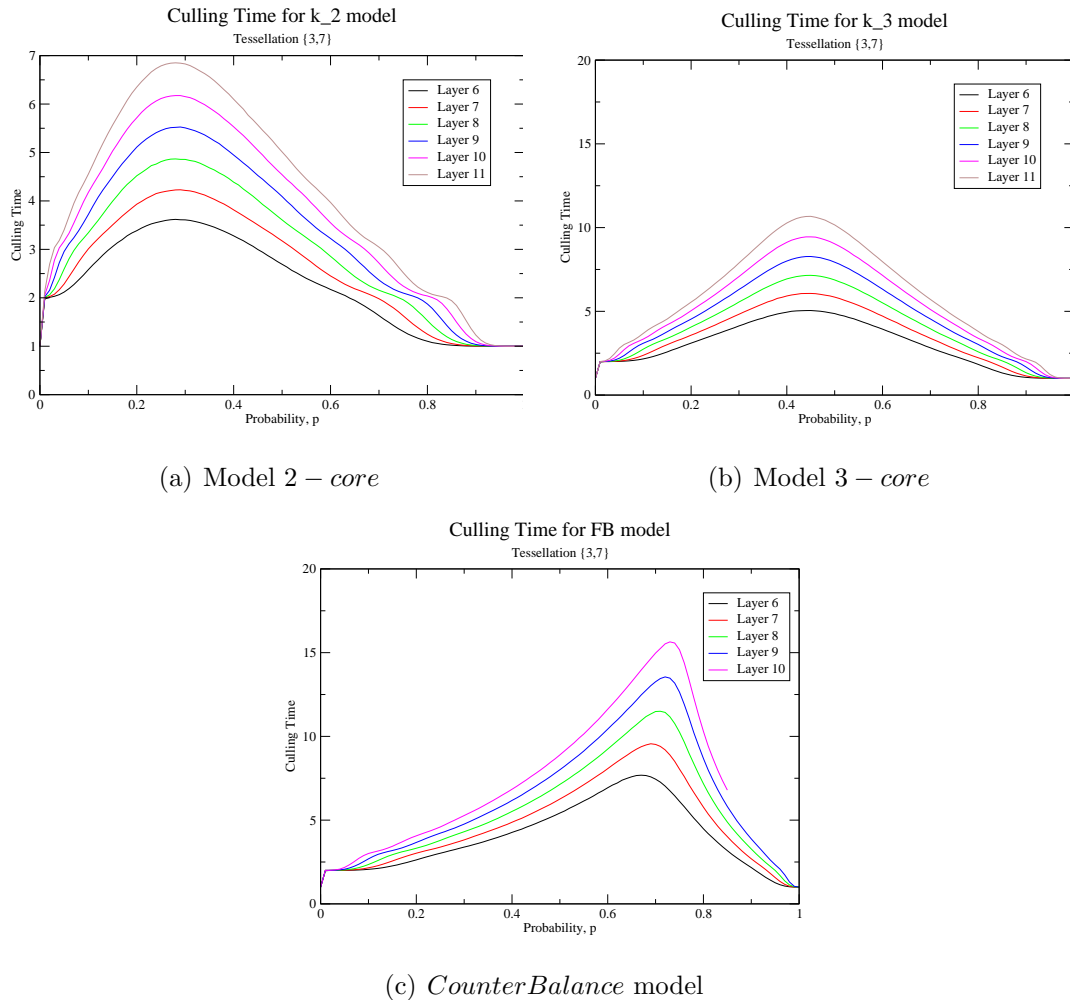


Figure 3.12: Culling time for the different constraint percolation models for the $\{3,7\}$ lattice. Each data set was averaged over 50,000 samples.

measured in three different ways. The probability above which the ratio between the second biggest cluster and the biggest cluster, S_2/S_1 , becomes negligible, or there is a finite fraction of the boundary points connected to the middle, or the cluster size distribution $P(s)$ becomes power law.

According to Ref. [100], p_l and p_u can be measured from the crossing probability $R(p)$, i.e. the probability of having a cluster going from one side of the lattice to the other. While this is the more straightforward measure, it would be good to find other measurements as consistency checks. It is important to note that there is a

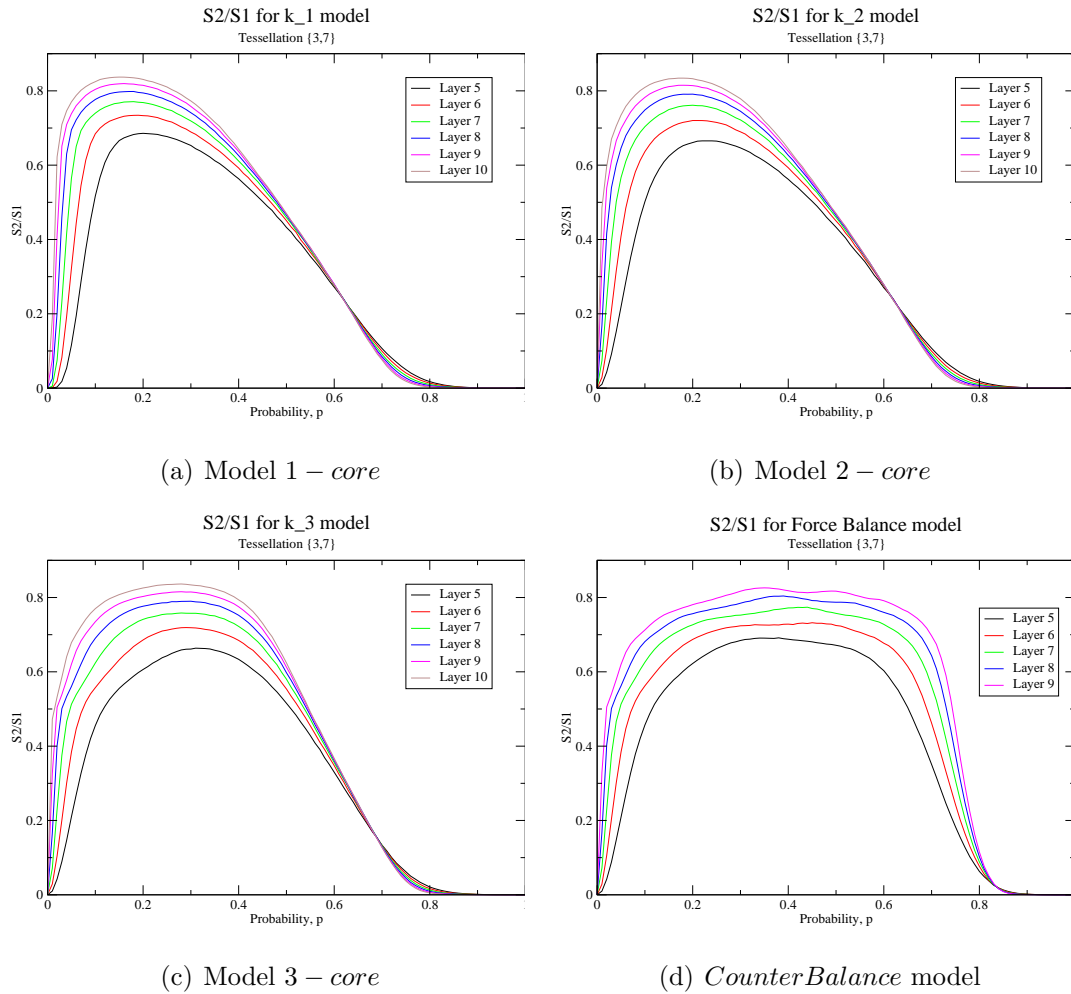


Figure 3.13: Ratio S_2/S_1 for different models and for Tesselation $\{3, 7\}$

relationship between p_l and p_u on a lattice and its values on the dual lattice that are denoted as \bar{p}_l and \bar{p}_u respectively. Such relationship is

$$p_l + \bar{p}_u = 1, \quad \bar{p}_l + p_u = 1. \quad (3.2)$$

As the measurement of p_l is less controversial than the one for p_u we can use Eq. (3.2) to calculate p_u by calculating \bar{p}_l on the dual lattice. Regarding the controversy for calculating p_u , Ref. [102] determines a way of finding p_u by measuring the ratio $S2/S1$ between the second largest and largest clusters. The initial claim was that in the infinite limit such a curve will be discontinuous at some intersection point (see their Fig. 4).

We measure the ratio $S2/S1$ where $S1$ is the size of the biggest cluster and $S2$ is the size of second biggest cluster. Again, the p at which this ratio jumps to zero in the infinite limit determines p_u (according to Ref. [102]). In a more recent paper though, the same authors state it could be the case that the curve not be discontinuous at this point, such as the curves for $R(p)$. In fact, according to Fig. 3.13(a) this seems to be the case here. So we do not rely on this method any further.

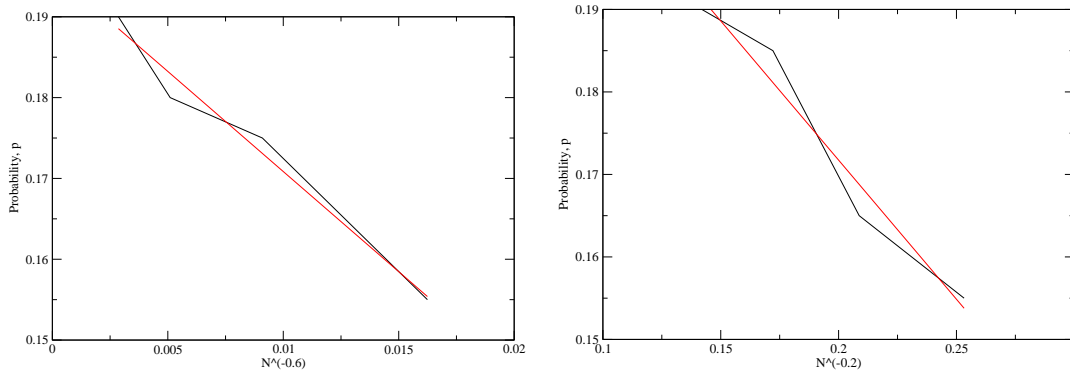
For $k = 1$ -core model we developed an estimate for p_u according to the procedure outlined in Ref. [100] for tessellations $\{3, 7\}$ and $\{7, 3\}$. We measure the slope of the curve on the crossing point region (see Fig. 3.13(a) for tessellation $\{3, 7\}$). Accordingly, the best estimate for p_u in the tessellation $\{3, 7\}$ is $p_u = 0.73 \pm 0.02$ and in the tessellation $\{7, 3\}$, $p_u = 0.86 \pm 0.02$.

To estimate p_l we search for the point at which the crossing probability is greater or equal than 10^{-4} , similar to the procedure followed in Ref. [100]. For these calculations the data was averaged over 100000 runs and has large fluctuations.

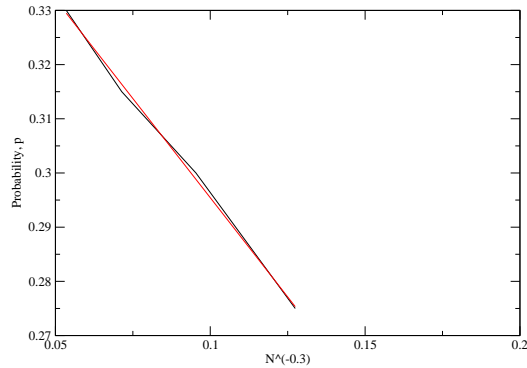
In Fig. 3.14 we illustrate the extrapolation for getting p_l for the k -core models on the tessellation $\{3, 7\}$. For $k = 1$ -core, $p_l = 0.20$; for $k = 2$ -core, $p_l = 0.24$; for $k = 3$ -core, $p_l = 0.37$ Accordingly, for unconstrained percolation ($k = 1$ -core) on tessellation $\{3, 7\}$, we have $p_l + \bar{p}_u = 1.06$, which very roughly satisfies eq. 3.2.

3.5 Discussion

We have studied four constraint percolation models on mainly the $\{3, 7\}$ hyperbolic tessellation. We find that all three k -core models exhibit similar behavior falling



(a) Model 1-core. Best fitting was by scaling with $N^{-0.6}$ and getting $p_l = 0.196$, Correl. coef. -0.9885
 (b) Model 2-core. Best fitting was by scaling with $N^{-0.2}$ and getting $p_l = 0.239$, Correl. coef. -0.9885



(c) Model 3-core. In this case we have two extremely close correlations. For l^{-1} we got $p_l = 0.438$ with Corr. Coef. -0.9990 and for $N^{-0.3}$ we got $p_l = 0.369$ with Corr. Coef. -0.9989. I am showing here just the correlation with N

Figure 3.14: Crossing Probability results for different models and for Tessellation $\{3, 7\}$

under the universality class of unconstrained percolation. This is not a surprise for $k = 1, 2$ -core percolation, which have been shown to behave similarly to unconstrained percolation. However, given the mixed $k = 3$ -core transition on Bethe lattices, but the continuous phase transition (should $p_c < 1$) on Euclidean lattices may be surprising. In fact, earlier work of $k = 3$ -core percolation on hyperbolic lattices argued that the transition behaves discontinuously (in terms of the order parameter). In this earlier work, it was proven that $p_c < 1$ for $k = 3$ -core percolation on hyperbolic lattice of certain types, which is an important step in that it constrains the analysis of the data. However, there was no proof of the discontinuity, only arguments and some numerical evidence. So our results do not contradict mathematics.

An interesting result is that k -core models exhibit two critical probabilities, p_l and p_u , meanwhile counter-balance model seems to exhibit just one critical probability. This comes from the fact that the counter-balance condition constrains the spatial occupation of neighbors of an occupied site in such a way that the cluster tends to expand in every direction. It does not allow the possibility of having several percolating clusters that do not overlap.

From Sec. 3.4.3 we have for the cluster size critical exponent the values $\tau = 2.09, 2.07, 2.04$ for $k = 1, k = 2$, and $k = 3$ -core models respectively. Meanwhile, for the counter-balance model we have $\tau = 1.76$, all this on the tessellation $\{3, 7\}$. Then it seems to have a clear distinction again between counter-balance and the k -core models, which all seem to have a similar behavior.

According to the behavior of the order parameter, P_∞ , k -core models exhibit a continuous transition, while counter-balance is discontinuous, at least on the $\{3, 7\}$ tessellation. Counter-balance percolation is also discontinuous on Euclidean lattices so it does not change this nature by the changing of the underlying geometry.

The observation that the nature of the transition in $k = 3$ -core percolation does not change from Euclidean lattices to hyperbolic lattices may indicate that any decrease in the number of loops is not enough to drive the transition from a mixed

transition on the Bethe lattice, where there are no loops. In other $k = 3$ -core percolation is very sensitive to loops. We must think about this further to better understand the nature of the k -core percolation phase transition in all geometries.

Chapter 4

Cell motion in densely packed tissues

4.1 Introduction

There has been much quantitative study of individual cells moving on two-dimensional surfaces [41, 42]. Recent work on cell motion in densely packed tissues (composed of many cells), however, demonstrates properties that are rather different from the properties of individual cell motion. More specifically, in densely packed, or confluent, tissues, where there are no gaps between cells, researchers have discovered signatures of collective motility such as dynamical heterogeneities [35, 36], caging behavior and anomalous diffusion [37]. The first two properties cannot be observed in single cell experiments and individual cells tend to undergo a persistent random walk, as opposed to anomalous diffusion [104]. These differences are significant since a cell moving through other cells is a more native environment than a single cell moving on a two-dimensional surface.

Dynamical heterogeneities, caging behavior, and anomalous diffusion occur in many glassy non-biological materials, including polymers, granular materials, and foams [27]. As mentioned in the introduction, they can be understood in terms of the

potential energy landscape, which specifies the total potential energy of a material as a function of the positions of all the degrees of freedom, such as the particle positions. Any glassy material spends most of its time close to a mechanically stable minimum in the potential energy landscape. Rare fluctuations, however, can overcome the high energy barriers and allow the material to escape to a new minimum. These collective, rare fluctuations typically involve a particle escaping from a cage generated by its neighbors and the subsequent rearrangement of such particles. Therefore, knowing the distribution of these energy barriers contributes toward the understanding of particle motion in such systems.

The distribution of energy barriers in rigid nonliving materials such as dry foams has been studied [105]. Dry foams are jammed at confluence. The individual elements, therefore, do not change neighbors unless a sufficient external force is applied at the boundaries. So energy is injected at the boundaries via shear to study the rearrangements. The rearrangements tend to occur at special weak regions or soft spots in the material [106] and the energy barriers associated with these rearrangements are power-law distributed [105].

Since cells in confluent tissues constitute living, or active, matter, they can regularly intercalate, or exchange neighbors in the absence of external forces [38]. They do so by actively changing their shapes and exerting forces on contacts to overcome large mechanical energy barriers and transition from one metastable state to another. So cell motility in tissues is set not by single-cell migration rates but instead by the rate at which cells can squeeze past neighbors. Because energy is injected locally, instead of globally at the boundaries, the statistics of energy barriers explored by cells might be very different from those in inactive materials.

There is currently no existing theoretical framework for predicting energy barriers to cell motion in confluent tissues. This work represents the first attempt to do so. We will do it using a shape equilibrium, or vertex, model where each cell has an energy contributing to bulk deformations, an energy contributing to surface tension,

and a contribution accounting for the elastic contractility of the actomyosin based cortex [107]. Such models have been successfully used to predict the minimum energy shapes of 2D cross-sections of 3D cells in confluent tissues [108, 109, 110, 111]. We should mention that although several recent particle-based models for collective cell motion show signatures of glassy dynamics [112, 113], these break down at confluence and do not capture changes to cell shapes that occur during intercalation.

This chapter is organized as follows. We first present the shape equilibrium model used to describe the deformations of cells in confluent tissues. We then study active T1 transitions between four cells in this model, which is the minimum number of cells required in any T1 transition. Recall from the introduction that a T1 transition allows for neighbor exchange so that a cell can move through the confluent tissue via a sequence of T1 transitions due to its activity (hence the term “active T1 transition”). We study the energy barrier associated with this transition numerically and analytically. We then study a collection of 64 cells and compare our results to the simpler four cell case, as well as hint at what can happen when one of the cells moving through the confluent tissue is of a different type than others with an eye towards understanding how cancer cells move through tissue at the single cancer cell level. We end with a discussion of the implications of our work.

4.2 Model and Methods

To capture the shapes of cells and how the shapes evolve as cells migrate in a confluent tissue, we consider the following energy functional for the i th cell in a two-dimensional slice/monolayer of a three-dimensional confluent cell packing that depends on its shape [109]:

$$E_i = \xi_i P_i^2 + \gamma_i P_i + \beta_i (A_i - A_0)^2, \quad (4.1)$$

where P_i and A_i are the perimeter and area of the i th cell respectively. The first term in this energy is quadratic in the perimeter. It represents the active contractility

due to the actin-myosin sub-cellular cortex as regulated by an elastic constant ξ_i . The second term in Eq. (4.1) captures the competition between line tension in the cortex and the effects of cell-cell adhesion. When cells strongly adhere, it is more energetically favorable to increase its perimeter, hence implying a negative γ_i . When cell-cell adhesion is small and surface tension dominates, then γ_i is positive.

The third term in Eq. (4.1) can be obtained by the following argument. Assume that a cell is an incompressible medium with fixed volume V_0 in three dimensions. When packed into a columnar layer, the height of each cell is given by H and the area A such that $V_0 = AH$. With V_0 fixed, the change in the cell height is related to the change in cross-sectional area,

$$\delta H \sim -\Delta A. \quad (4.2)$$

Under confluent conditions (no gaps between cells), the change in the columnar height is determined by the strength of the adhesion with the neighboring cells. To first order, this adhesive energy can be approximated by a linear spring coupling to the change in cell height, ΔH :

$$E \sim \Delta H^2. \quad (4.3)$$

Combining these two equations, we arrive at the third term in the cell shape energy, where β_i is the height elasticity set by intercellular adhesion and A_{i0} is the preferred area of the i th cell.

The shape energy for the i th cell (Eq. (4.1)) contains a gauge freedom since its definition depends on differences from some baseline energy. It is the energy differences that are physically relevant. Using this gauge freedom, we can complete the square for the perimeter term to write

$$E_i = \xi_i(P_i - P_{i0})^2 + \beta_i(A_i - A_0)^2, \quad (4.4)$$

where an effective preferred perimeter $P_{i0} = -\gamma_i/(2\xi_i)$ can be defined.

For the moment, we consider all single cell properties to be equal, i.e. $\beta_i = \beta$, $\xi_i = \xi$, $A_{i0} = A_0$, and $P_{i0} = P_0$ for all i . The total shape energy for a confluent monolayer composed of N cells can then be written non-dimensionally as

$$\varepsilon = \frac{1}{\beta A_0^2} \sum_{i=1}^N E_i = \sum_{i=1}^N [(a_i - 1)^2 + \kappa(p_i - p_0)^2], \quad (4.5)$$

where $a_i = A_i/A_0$ and $p_i = P_i/\sqrt{A_0}$ are the rescaled area and perimeter respectively. The rescaled modulus $\kappa = \xi/(\beta A_0)$ is the generalized contractility and $p_0 = P_0/\sqrt{A_0}$ is the generalized line tension. Note that p_0 becomes negative when cell-cell adhesion is negligible and surface tension dominates. We will not consider that case here and only focus on $p_0 > 0$ here.

The above mechanical energy functional has been remarkably successful in predicting cell shapes in embryonic tissues [108, 110] and it allows for anisotropic interactions between cells. Although a few researchers have used these models to investigate the effects of cell growth and division [108, 109]. We will now use it to analyze cell migration.

Under confluent conditions, cells can only rearrange via active T1 topological swaps, as illustrated in Fig. 4.1. Although cell division and death can lead to fluid-like behavior [114], these are not necessary for cell migration [37, 115] and, therefore, we study cell packings in the absence of these processes. When considering a packing of cells, to induce an active T1 transition at an edge, the total energy is minimized while the length of the edge L is actively decreased from h until the edge reaches zero length. Such processes are common during planar junction remodeling in epithelial layers [38]. A topological swap takes place at $L = 0$. The new edge is actively increased back to its initial length and then allowed to relax to its final unconstrained minimized state. Except for this active T1 transition, the topology of the network of vertices and edges remains fixed. Cell motion can arise due to a sequence of active T1 transition by an individual cell.

How is the total energy minimized? Each cell is specified by its vertices, edges,

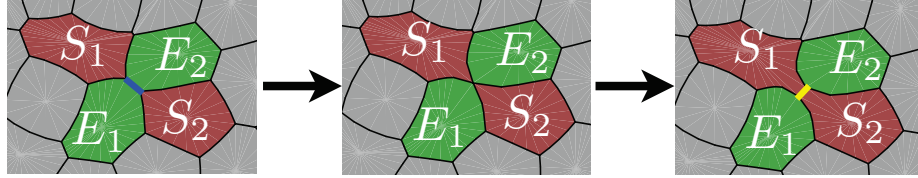


Figure 4.1: Illustration of an active T1 transition in a model confluent tissue. Cells E_1 and E_2 share an edge before the transition and become disjoint after the transition, while S_1 and S_2 are disjoint before the transition and share an edge after the transition.

and faces. Surface Evolver uses this information to numerically minimize the energy of the N cell system using gradient descent, with respect to the vertices of the cells, to find the nearest local minimum [116]. The edges of the cells are also refined (bisected) to look for more continuous changes in shapes before the energy minimization takes place. All structures and states studied here have been minimized such that the average energy of a cell changes by less than one part in 10^5 between consecutive minimization steps.

This active T1 transition can be easily studied with $N = 4$ cells, the minimum number of cells required for the transition. We do so assuming a hexagonal arrangement of hexagonally shaped cells for simplicity. Polygonal shaped cells are observed in images in monolayers of confluent tissues so this simplification is not superficial. Moreover, while an $N = 4$ cell seems very simplistic, active T1 transitions can be experimentally studied in such a system as long as the four cells are confined presumably.

We also study the active T1 transition in many cell packings. To generate an amorphous packing of $N > 4$ cells, we generate a random point pattern of N points in a box of length L , with L chosen such that the area per cell is unity. Periodic boundary conditions are implemented. This initial random point pattern is generated using uniformly distributed points. A Voronoi tessellation is then generated based on the initial random point pattern resulting in a fully connected structure of N cells.

This structure is then inputted into Surface Evolver as described above.

4.3 Results

4.3.1 $N = 4$ cells

To study active T1 transitions, which is minimally a four cell-interaction, we begin with the simplest $N = 4$ cell system shown in Fig. 4.2. As stated previously, the active T1 move is induced by shortening the green apical junction, initially of length $L = h$. When the green apical junction is shrunken to zero length, $L = 0$, a topological swap is made such that neighboring cells are exchanged. After the apical junction remodeling, L is then increased until $L = h$ with energy minimization invoked at each change in length. For convenience, we set $a_i = 1$ and $\kappa = 1$.

To study the energy barriers to cell migration using active T1 transitions, in Fig. 4.3, we present the shape of an active energy barrier by plotting $\varepsilon_{tot}(L)$ for $p_0 = 3.0$. We observe that as the edge length decreases, the energy of the system increases until reaching a maximum at $L = 0$. The energy then decreases as the edge length is increased again after the active T1 transition. The energy barrier $\Delta\varepsilon$ is given by

$$\Delta\varepsilon = \varepsilon_4(0) - \varepsilon_4(L). \quad (4.6)$$

So the cell must overcome this energy barrier to obtain new neighbors.

To understand the effect of p_0 , which means increasing the cell-cell adhesion, we present $\Delta\varepsilon$ for p_0 ranging from 3 to 4 (Fig. 4.4). We observe that as p_0 increases, $\Delta\varepsilon$ decreases monotonically until reaching zero. The decrease is approximately linear, but clearly there is some curvature. Beyond $p_0 \gtrsim 3.8$, the active energy barrier vanishes. A finer increment in p_0 and additional refinement reveals that the active energy barrier vanishes near $p_0 \approx 3.72$, which is the perimeter of a regular hexagon of unit area. The additional refinements, where the number of refinements is denoted by NR increases the number of degrees of freedom since each edge is bisected with

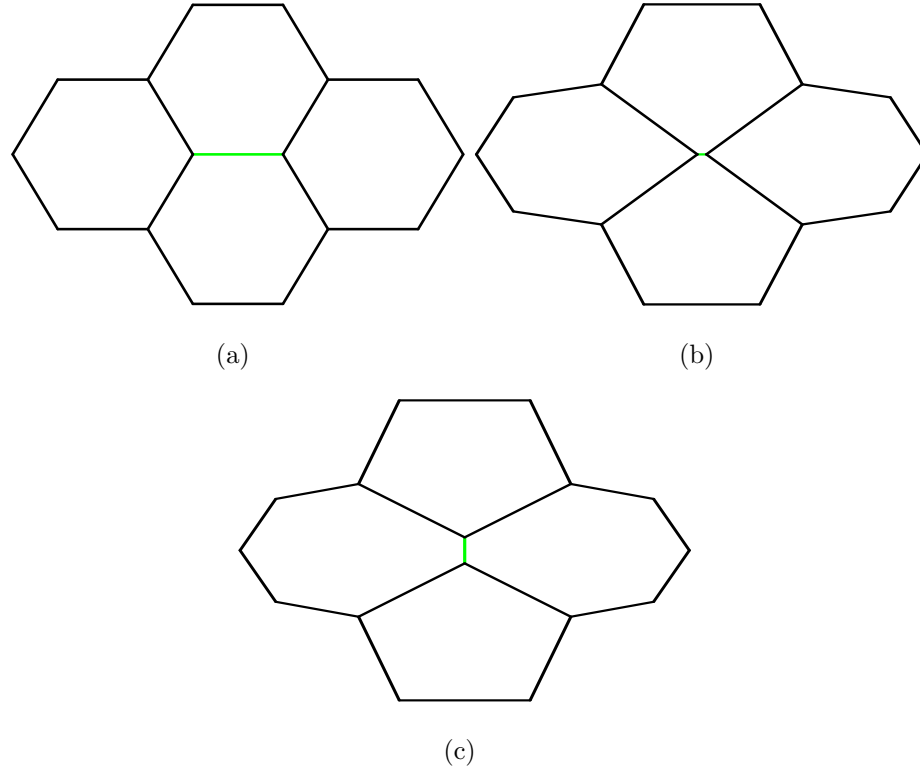


Figure 4.2: (a) The initial $N = 4$ cell configuration. (b) The length of the center horizontal edge (colored green) decreases. (c) The $N = 4$ cell configuration after the active T1 transition is applied, and the now vertical center edge is expanded.

each refinement. While this is only a four-cell system, it is interesting that we observe an active rigid-to-fluid transition where the system goes from having active energy barriers to impede cell migration to not having active energy barriers so that it is easy for a cell to migrate through the confluent tissue as the cell-cell adhesion increases. We should mention that near the rigid-to-fluid transition (the vanishing of the energy barrier), we checked that $NR = 3$ refinements agreed with $NR = 2$.

To understand the rigid-to-fluid transition in this $N = 4$ cell system, let us construct the following analytical calculation. We consider a system of four regular hexagonal cells with unit area. Correspondingly, the length of each side of each hexagon is $h = \frac{\sqrt{2}}{\sqrt{3\sqrt{3}}}$. It is then assumed that the only region near the edge that is transformed changes shape. Accordingly, the change in energy for the system illus-

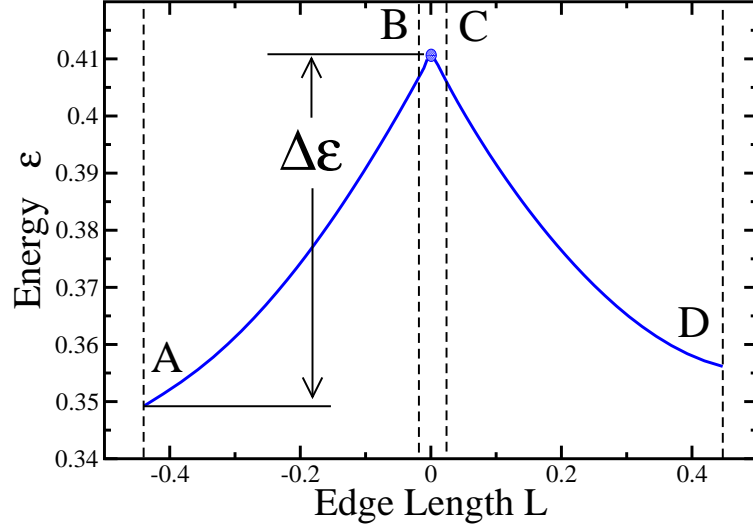


Figure 4.3: The total energy of the $N = 4$ cell system with $p_0 = 3.0$. The energy barrier is denoted by $\Delta\varepsilon$. Points A and B correspond to Fig. 4.2(a) and Fig. 4.2(b) respectively. The negative lengths correspond to before the T1 transition and the positive correspond to after.

trated in Fig. 4.2 when the edge undergoing the T1 transition shrinks from $L = h$ to $L = 0$ is

$$\begin{aligned} \Delta\varepsilon_A(L) &= \sum_{i=1}^4 \{(a_i(L) - 1)^2 + \kappa(p_i(L) - p_0)^2\} - \sum_{i=1}^4 \{(\kappa(6h - p_0))^2\} \\ &= 8S(L)^2 + 2\kappa [4h + 2h'(L) - p_0]^2 + 2\kappa [3h + L + 2h'(L) - p_0]^2 - \sum_{i=1}^4 \{(\kappa(6h - p_0))^2\} \end{aligned} \quad (4.7)$$

where $S(L) = \sqrt{3}h(h - L)/8$ and $h'(L) = \frac{1}{2}h\sqrt{7 - \frac{4L}{h} + \frac{L^2}{h^2}}$. See Fig. 4.5 for the definitions of S and h' . Note that we have not minimized the energy in this calculation and therefore distinguish this energy change, $\Delta\varepsilon_A(L)$, from $\Delta\varepsilon$ above, where the energy is minimized at each step. Figure 4.6(a) plots $\Delta\varepsilon_A(L)$ as a function of L for $p_0 = 3.0$. The curve looks similar in shape to the minimized curves (Fig. 4.3), but the scale is larger because the energy is not being minimized, only tracked. If we plot $\Delta\varepsilon_A(h)$ from this analytical calculation as a function of p_0 , then we obtain Fig. 4.6(b). We, again, observe a rigid-to-fluid transition with the energy barrier vanishing around $p_0 \sim 4.4$. This transition is surely an upper bound because we have not minimized the energy. In any event, at large enough p_0 , the energy barrier

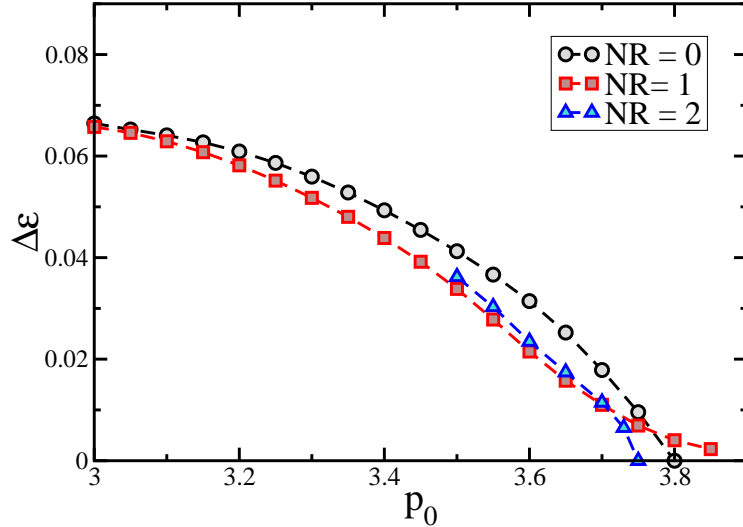


Figure 4.4: The energy barrier as a function of p_0 ranging from 3 to 4 varying the number of refinements, NR . In Surface Evolver, each refinement bisects an edge to double the number of vertices. There is a rigid-to-fluid transition (the vanishing of the energy barrier) around $p_0 = 3.72$.

vanishes.

We should also note that a similar analytical calculation but with the area fixed yields a vanishing of the energy barrier near $p_0 = 3.8$, which is the preferred perimeter for a pentagon with unit area. With this result, the rigid-to-fluid transition could simply be interpreted as the emergence of zero energy cost pentagons (for fixed area), which is one of the final two polygons involved in the T1 transition.

How does energy barrier change with different shape profiles of the cells as they make the active T1 transition? Even in this simple $N = 4$ cell system arranged in this particular manner, can we address this question by adding vertices to some of the edges near the active T1 transition and pinning these additional vertices. For instance, we pin four vertices involved in the active T1 transition some distance from the transition edge. We denote that distance to be x . See Fig. 4.7. Figure 4.8 shows several energy traces as the T1 edge is swapped for different x s. For small x , $x < 1/2$, the energy required to undergo a T1 transition is larger than the barrier so and the T1 transition does not occur. What does this mean physically? When x is

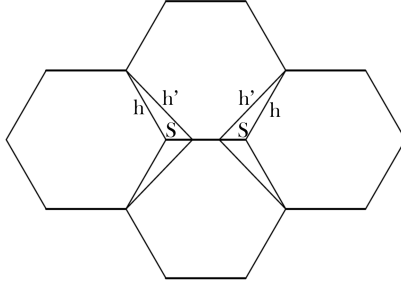


Figure 4.5: Schematic for quantities used in the analytical calculation. The quantity S is the area of the triangle enclosing it.

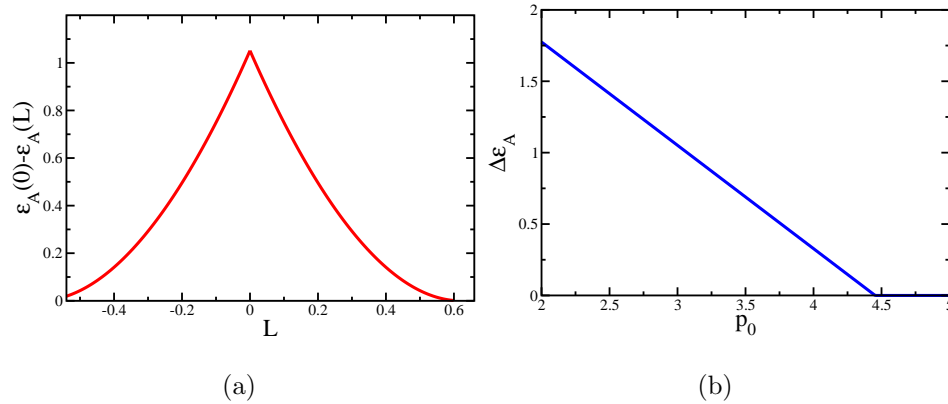


Figure 4.6: (a) Energy trace for active T1 transition for $p_0 = 3$ from the analytical calculation. (b) Energy barrier as a function of p_0 from the analytical calculation.

near zero, the “nose” of the transition cell is very narrow and constrained, making it more difficult to move past its neighbors. As x increases to h , the nose becomes broader. We find that the active energy barrier decreases with increasing x in Fig. 4.9 for larger x ($x > 1/2$). This result suggests that the broader the nose, the faster the cell can migrate, assuming the attempt frequency as discussed in Chapter 1 is independent of the profile. In other words, a needle-like protrusion for the moving cell would not be as energetically favorable if it wanted to optimize its migration speed. To demonstrate that our results are rather independent of the number of refinements and the precision level in accepting when the energy stops changing, we plot our

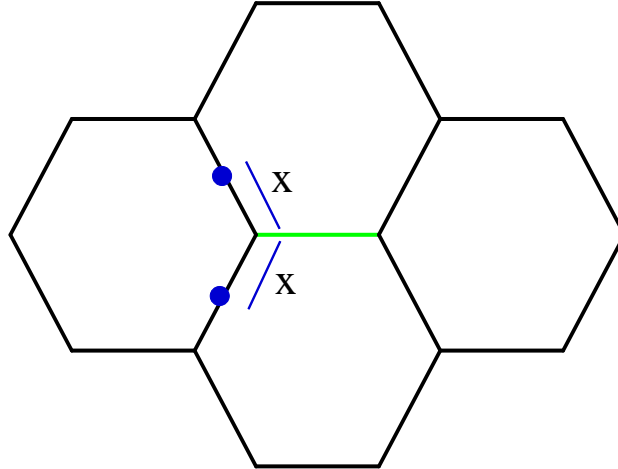


Figure 4.7: Schematic depicting the parameter x used in the calculation. The blue circles denote added vertices that are pinned before the active T1 transition.

results for different numbers of refinements and for different precision level. Recall that our precision level is one part in 10^5 is used throughout, unless stated otherwise.

Finally, before going to the many cell case, we investigate the change in the energy barrier when the migrating cell is different from the remaining cells. Such investigation could be useful to study how cancer cells, for example, migrate through a confluent tissue. While tumors tend to be stiffer than the surrounding healthy tissue, individual cancer cells tend to be softer (lower Young modulus, analogously lower β_i) than healthy cells [117]. This difference can be captured in our model by changing the generalized contractility κ , or equivalently a dimensionless parameter γ multiplying the area term for the $i = 1$ entry of the energy. This $i = 1$ cell represents the cancer cell. Now see Fig. 4.10. We find that as cancer cell becomes softer by decreasing its γ_1 , the energy barrier for the T1 transition is lowered monotonically. So the cancer cell will be more motile than a healthy cell.

4.3.2 Many cells

We now consider $N = 64$ cells. Figure 4.11 shows an example packing. Fig. 4.11. Figure 4.12 then shows the total energy of the system as a function of the edge length

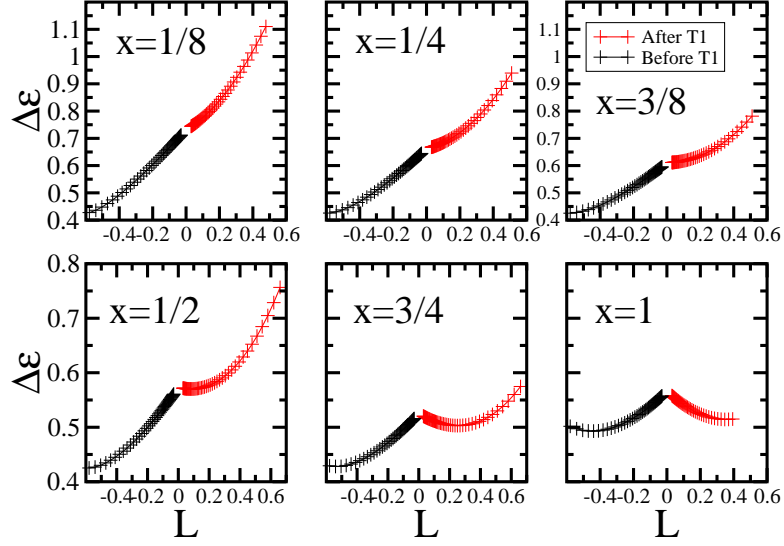


Figure 4.8: Energy barrier traces for different x s for $p_0 = 3.0$.

during a typical T1 transition. As before, the length L is displayed as a negative number before the T1 transition and positive after the T1 transition. The energy barrier for this process $\Delta\varepsilon$ is defined as the minimum energy required to escape state A towards another stable state D . The shape of the energy barrier profile looks very similar to the $N = 4$ case. Also note that as in the shape profile study for $N = 4$ cells, the energy continues to increase after the T1 transition (Fig. 4.12(c)). In some of these cases, once all the edges in the system are relaxed (unpinned), a lower energy state can be found. So the energy barrier required for the active T1 transition is larger than the energy required, i.e. the transition does not occur.

With this amorphous packing we can now obtain statistics for $\Delta\varepsilon$. We do so by testing the active T1 transition path on six randomly generated tissues each consisting of $N = 64$ cells. With each tissue consisting of $\frac{6N}{2} = 192$ unique edges, a total number of 1152 unique transition paths can be investigated. These transition paths contain different topologies and shapes. For all cells in the tissue, we set the parameters such that the minimal shape for each cell is a regular hexagon of area 1: $\kappa = 1$ and $p_0 \approx 3.722$.

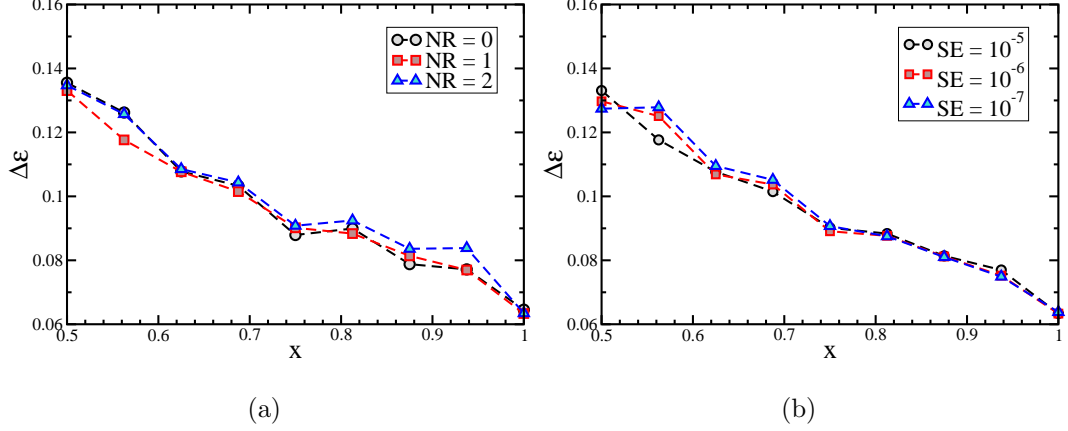


Figure 4.9: (a) Energy barrier as a function of x for different numbers of refinements (NR) and (b) for different precision levels for the energy (SE). The precision level is set to 10^{-5} unless stated otherwise.

The distribution of energy barriers $\varrho(\Delta\varepsilon)$ of these transitions is shown in Fig. 4.12(c). The tail obeys an exponential distribution:

$$\varrho(\Delta\varepsilon) \propto e^{-c \Delta\varepsilon/\langle\Delta\varepsilon\rangle} = e^{-\Delta\varepsilon/\varepsilon_0}, \quad (4.8)$$

where fitting has determined $c = 1.18$ and we define $\varepsilon_0 = \langle\Delta\varepsilon\rangle/c$. This exponential distribution is robust to changes in model parameters κ , p_0 , and cell-to-cell variations ($A_0 \rightarrow A_{0i}$) [40].

Our data suggests that the exponential tails ultimately arise from an interplay between the statistics of edge lengths and the energy functional. The initial T1 edge lengths denoted by L_α are Gaussian distributed. We find, however, that the change in energy due to a reduction in cell perimeter is quadratic in L_α , resulting in an exponential distribution for energy barriers. Our results should be contrasted with nonliving sheared foams. Sheared foams generically generate power-law distributed energy barriers with an exponential cutoff [105]. Our exponential energy barriers appear to be a unique feature of confluent tissues where energy is injected locally. This is intriguing because it is precisely the distribution seen in glassy systems with quenched disorder [33]. One could argue that a power-law distribution of energy

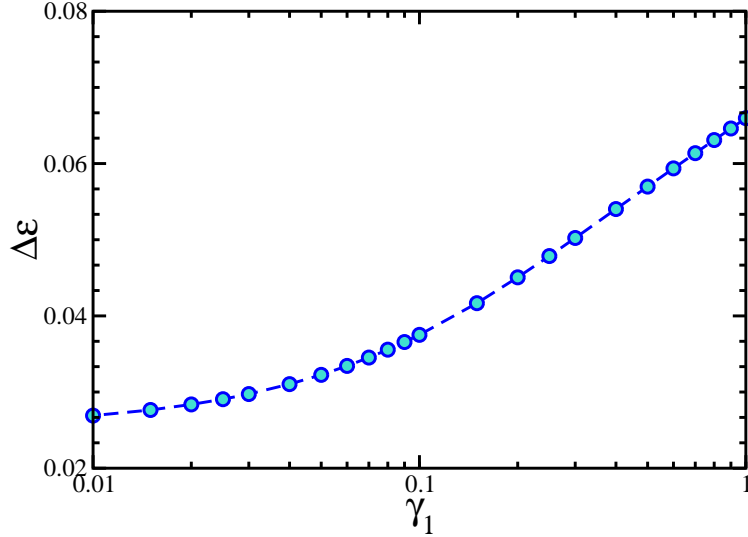


Figure 4.10: $\Delta\epsilon$ for $p_0 = 3$, $\kappa = 1$ for all four cells and different γ_1 for the migrating cell (initially the leftmost cell), where γ_1 is a dimensionless parameter multiplying the area term in the energy.

barriers indicates a more collective process than an exponential distribution. With our shape change model, there are indeed more degrees of freedom than the shape fixed foam model. The overall effect may be to average over spatial fluctuations in a way that the more simple trap model that does not take into spatial preferences in going from one trap to another is more applicable than the foam model.

4.4 Discussion

We have simulated confluent tissue monolayers and numerically calculated the energy barriers required for cell rearrangements via active T1 transitions. We first measure the energy barrier for an $N = 4$ cell packing. We also investigate the dependence of the energy barrier on the shape profile and when one type of cell is migrating among another type of cells forming a tissue. We have also investigated the statistics of these energy barriers by studying $N = 64$ cell packings. We demonstrate that the distribution of energy barriers, $\varrho(\Delta\epsilon)$, is exponential. The shape of the energy barrier in the $N = 64$ case is rather similar to the $N = 4$ case, interestingly enough.

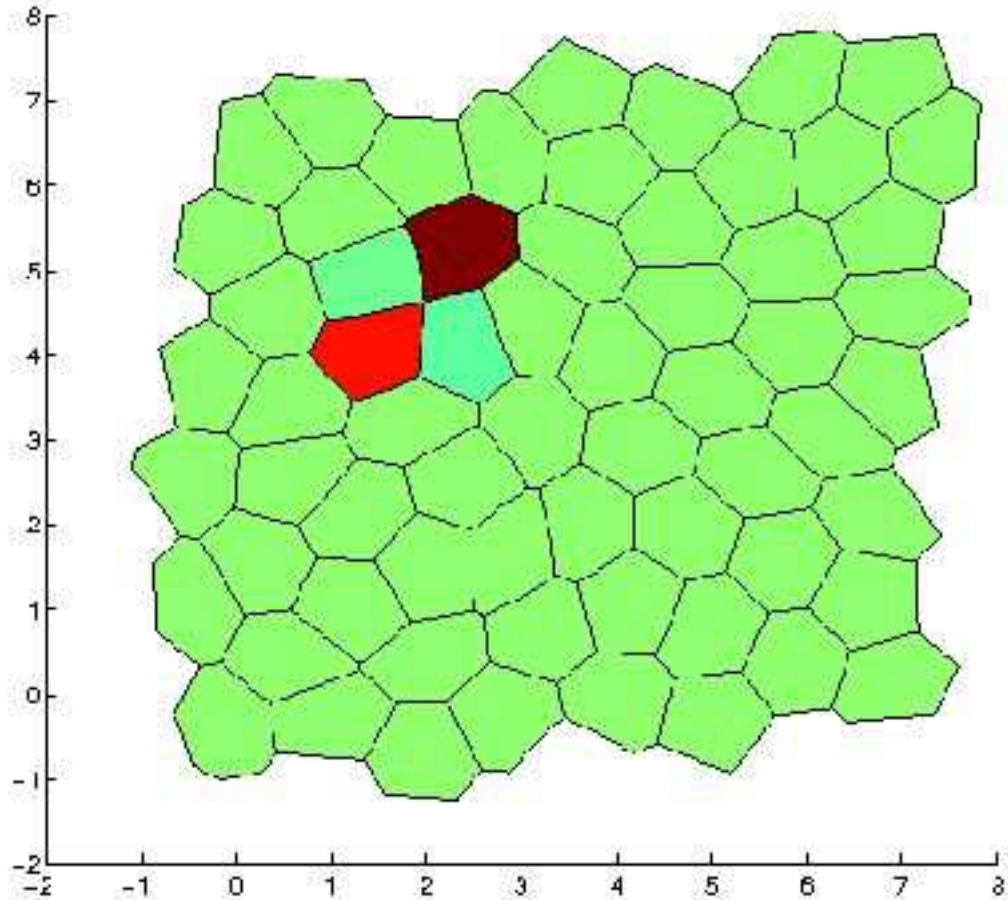


Figure 4.11: An $N = 64$ amorphous, confluent cell packing. See. Ref. 39.

What consequences does this finding have for a cell migrating through a confluent tissue via consecutive active T1 transitions? Recall from Chapter 1 that in traditional statistical mechanics, the rate at which a nonequilibrium (but thermal) system transitions from one metastable state to another is described by an Arrhenius process,

$$R = \omega_0 e^{-\Delta\epsilon/\epsilon_0}, \quad (4.9)$$

where $\Delta\epsilon$ is the energy barrier separating two metastable states, ω_0 is an inherent escape attempt frequency, and $\epsilon_0 = k_B T$ is the scale of energy fluctuations.

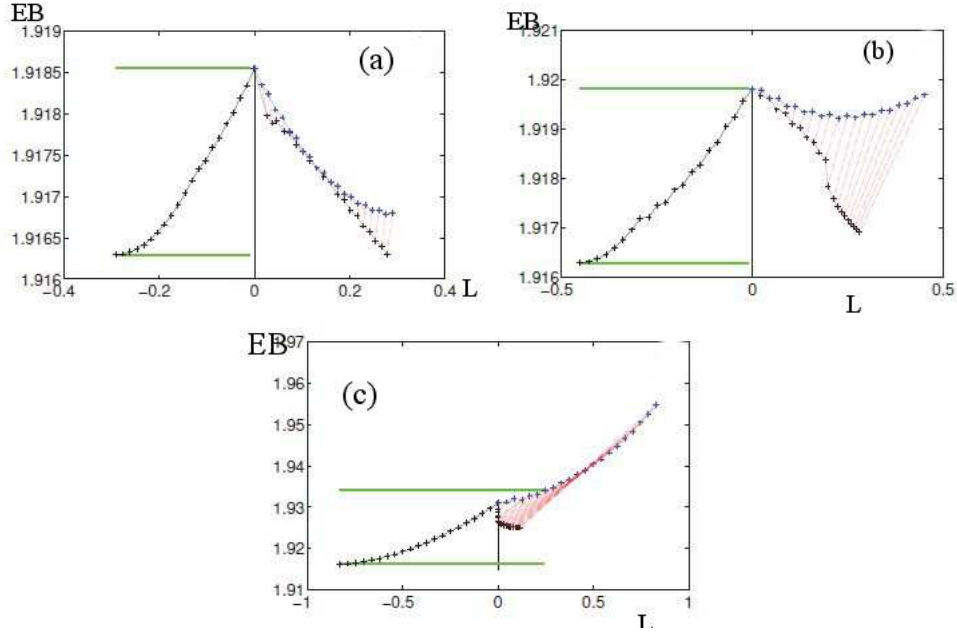


Figure 4.12: Typical energy barrier traces from the $N = 64$ cell simulation. The EB stands for energy barrier. (a) After the active T1 transition, without extra relaxation of the edges by unpinning blue vertices, the energy is a global minimum. (b) After the active T1 transition, the energy does not reach a local minimum, but after edge relaxation to black vertices, can reach a global minimum. (c) The energy continues to rise after the active T1 transition, without relaxation, no energy barrier is observed. With relaxation of all the edges in the system, a lower energy state can be found. So the energy barrier required for the active T1 transition is higher than the energy required to perform the active T1 transition, which means the transition will not occur. See Ref. 39.

While the assumptions on which Eq. (4.9) is based do not necessarily hold in biological tissues, analogues to parameters ω_0 , $\Delta\varepsilon$, and ε_0 exist in cells and likely govern cell motility. Several successful tissue models have characterized cell activity using an effective temperature ε estimated from membrane ruffling [118]. Both ε and the rate at which cells attempt to cross barriers ω_0 are correlated with cell protrusivity and active shape fluctuations, which are determined in large part by the cell's individual biochemical makeup. For simplicity, we assume that ω_0 and ε_0 are single-cell properties that are constant throughout the tissue, although other choices are possible and would be interesting directions of future study. In contrast, the

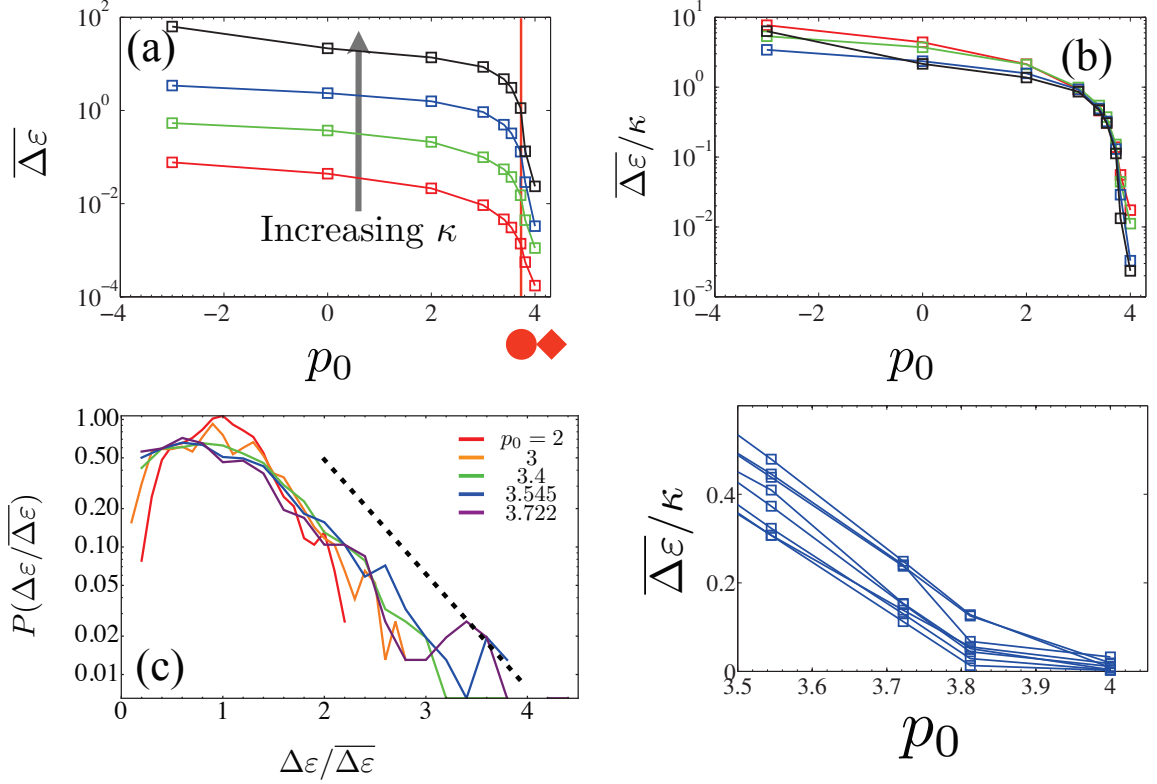


Figure 4.13: (a) The average $\Delta\varepsilon$ as a function of p_0 for different κ s. The circle and the diamond denote the perimeters of a circle and a circle respectively (both with area fixed at unity). (b) The average energy barrier dependence on κ is simple and can be scaled out. (c) The distribution of energy barriers in active T1 transitions. (d) The rigid-to-fluid transition in the $N = 64$ cell system. See Ref. 39. Also note that $\overline{\Delta\varepsilon} = \varepsilon_0$.

distribution of energy barriers, $\varrho(\Delta\varepsilon)$, is clearly a collective property determined by cell-cell interactions and the geometry of cell packing inside the tissue, as described in the previous section. We should also note that one can modify the Arrhenius factor to include a self-propelledness aspect of the cell. Please see Ref. 39 for more details.

From Eq. (4.9), the trapping time $\tau \equiv \omega_0^{-1} e^{\Delta\varepsilon/\varepsilon_0}$ is distributed at long times as

$$\varrho(\tau) \propto \frac{\omega_0}{(\omega_0 \tau)^{1+\Delta\varepsilon/\varepsilon_0}}. \quad (4.10)$$

When $0 < \frac{\Delta\varepsilon}{\varepsilon_0} = \mu < 1$, the averaging trapping (waiting) time diverges. In this regime, the total excursion time t of a migrating cell can be estimated from the

largest trapping time τ_c in M steps, or

$$t \sim M \int^{\tau_c} \tau \varrho(\tau) d\tau \sim M \int^{M^{1/\mu}} \tau^{-\mu} d\tau \sim M^{1/\mu}. \quad (4.11)$$

Here the upper bound of $M^{1/\mu}$ is obtained by assuming that a waiting time longer than τ_c occurs only one during the sequence. From the above scaling, the mean-squared displacement of the migrating cell is

$$\langle X^2 \rangle \sim t^\mu. \quad (4.12)$$

Since $0 < \mu < 1$, this behavior is called *sub-diffusive*. When $\mu > 1$, this anomalous-type behavior is transient, but the time over which it persists diverges as $\mu \rightarrow 1$.

In sum, the exponential distributed energy barriers can lead to such phenomena as anomalous diffusion, which has been observed in cell migration in zebrafish embryos. Note that we did explicitly map the parameters in the model to actual numbers. And while there is work done trying to infer mechanical parameters from the observed geometry of two-dimensional cell arrays [119], the prediction of anomalous diffusion and other glassy phenomena [39] is somewhat insensitive to the parameters used as physicists search for new mechanisms in biology based on minimal models, as opposed to explicit quantitative agreement. The implications for glassy dynamics in confluent tissues may dramatically affect the cell sorting process—the process by which different types of cells cluster to form organs and tissues.

Chapter 5

Active elastic dimers: Cells crawling along rigid tracks

Epithelial cells crawl to heal a wound, white blood cells migrate to chase and ingest harmful bacteria, and, in an embryo, neural crest cells move away from the neural tube to generate neurons, bone cells, and muscle cells [120, 121]. Since cell motility is integral to a wide range of physiological processes, quantitative understanding of it is an important step in the quantification of cell biology at and beyond the cell size scale.

To date, most quantitative understanding of cell motility pertains to cells crawling on surfaces [41]. For example, one can predict the shape of a crawling cell based on its speed [42]. And yet, is a smooth surface a native environment for a crawling cell? The answer is typically no. For instance, epithelial cells must crawl through the three-dimensional extracellular matrix (ECM) to heal a wound. The ECM consists mostly of fibrous collagen with a pore-size that can range up to the order of the cell size (tens of microns) [122]. So how does this type of environment affect single cell motility in terms of speed, overall direction of migration, and sensitivity or robustness to changes in the environment?

There has been a recent explosion in experiments tackling this question [5-17].

These experiments clearly demonstrate that cells crawling through the ECM can take on a very different shape from the ones crawling in two dimensions, namely, they mimic the fibrous environment of the ECM by elongating as they traverse along fibers [123]. An elongated shape is very different from the fan-like cell shapes observed in two dimensions such that new approaches to quantitative modeling may be needed. Based on these results, cell crawling experiments in one dimension have been conducted to study how one-dimensional single cell migration compares to three-dimensional single cell migration along fibers [124, 125]. Moreover, as the cell crawls through the ECM, the cell remodels it, again, calling for new approaches to prior two-dimensional quantitative modeling. While three-dimensional cell migration experiments are becoming numerous, there have been very few studies focused on quantitative modeling of these experiments.

Here, as a first step, we focus on modeling cells that move along very taut ECM fibers—taut enough such that they are essentially featureless (rigid) tracks. To do so, we build a one-dimensional model of cell motility along one fiber, or track, via a bead-active-spring model, the properties of which will be described below. See Figure 5.1. Bead-spring models have been successfully used to elucidate the role of cell mechanical properties in driving shape dynamics for cells crawling in two dimensions. In particular, Refs. [21] and [22] have captured bipedal locomotion in crawling cells using a two dimensional bead-spring model. Ref. [23] introduces a one-dimensional Brownian inchworm model for directed self-propulsion in the presence of noise. This model consists of an elastic dimer representing the front and rear of the self-propelled particle and shows that an effective friction force that depends on the elastic coupling between the two beads can rectify diffusive motion to lead to directed motion (even in the absence of an externally imposed gradient).

In our bead-active spring model, the spring represent stress fibers comprised of actin, myosin, and cross-linker complexes [126]. Because the stress fibers contain myosin motors, they contain an “active” component. ATP-driven myosin walk to-

wards the plus end of the actin filament such that two actin filaments of opposite orientation coupled via myosin will contract, as in muscle. While the orientation of the actin filaments is not as regular as in muscle, i.e. some filaments coupled via myosin are not oppositely oriented, overall contraction still occurs [127]. So the spring denotes the stress fibers, and the beads denote the location of focal adhesions, which enable the stress fibers connect to the ECM. Integrins are one of the main proteins comprising focal adhesions [128]. As far as the type of molecular bonding, it has been shown that integrins can act as catch bonds [129]. For catch bonds, the bond lifetime increases with increasing force before decreasing with even further increase in force, while for slip bonds, the bond lifetime decreases with increasing force [130, 131]. Catch bond behavior is less intuitive than slip bond, but their enhanced strength over a range of forces may play a key role in how cells respond to and explore their mechanical environment.

With these minimal ingredients in our quantitative model, we explore the following questions: What is the interplay between the kinetics of focal adhesion binding to the rigid track and the active mechanics of the stress fibers in affecting cell speed in this constrained environment? What about the role of myosin (active cross-linkers) versus passive cross-linkers in one-dimensional cell crawling? Also, what is the role of randomness, due to activity, on cell crawling? More precisely, how robust is the motion to randomness? The answers to these questions can then be tested *in vitro* with various knockdowns and/or mutant fibroblasts, for example, crawling along fabricated microbridges (with no side walls) as a starting point for understanding how a cell moves in the complicated microenvironment of the ECM.

The organization of this chapter is as follows. The next section details the ingredients for the minimal bead-active spring model along with the equations of motion of the model. Section III presents estimates of the parameters used. Section IV explores solutions to these equations, i.e. cell movement, in the physiological part of the parameter space. The final section, Section V, addresses the implications of our

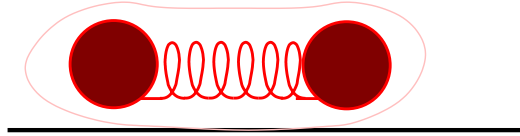


Figure 5.1: Side-view schematic of a two-bead-spring model of a cell crawling along a narrow track.

work.

5.1 A minimal model

We start by asking the following question: which aspects of two-dimensional cell movement hold for cells crawling along the fibers of the ECM, one of the native environments for a crawling cell? Two-dimensional cell crawling studies support the following scenario [41]: The cell extends its front via actin filament nucleation and polymerization and then creates mature focal adhesions under the new extension. Meanwhile, focal adhesions are disassembled near the rear of the cell so that the rear can retract to catch up with the front, which has since continued to extend. The retraction is myosin-driven since the use of blebbistatin suppresses motility of a cell [44], though leading edge cell fragments can continue to move via actin-treadmilling [45]. In this two-dimensional scenario, actin filament nucleation is driven by the branching agent, Arp2/3 [46, 132]. Arp2/3 nucleates branched filaments at a reasonably regular angle of 70 degree from the polymerizing end of actin filaments and, therefore, helps set the lateral extent of the leading edge of the crawling cell. This extent can be broad for cells crawling on two-dimensional substrates, resulting in fan-like shapes at the leading edge.

Some aspects of this description of two-dimensional cell crawling still hold for cell migration on ECM fibers, in the sense that there is extension, the assembly and disassembly of focal adhesions, and contractility driven by myosin. The most notable difference from two-dimensional studies is the elongated shape of cells undergoing

mesenchymal migration, or crawling along fibers. This observation has led researchers to conjecture that this particular mode of cell migration is effectively one-dimensional migration [123]. There are other observations that are consistent with the conjecture. For instance, Arp2/3 does not appear to be as important in generating motion here since the rather wide branch angle leads to large lateral lengths, which would not be commensurate with the underlying fiber [133]. Instead, actin filament nucleation via Arp2/3 is important for generating pseudopods whose possible function could be to search out for other ECM fibers to move along.

Here we study the motion along one fiber only, and focus on the interplay between stress fibers and focal adhesion. To quantify the interplay between focal adhesions and myosin-driven contractility, we construct a minimal one-dimensional model for a crawling cell as two beads connected by an active spring. The two beads denote the two ends of a cell that attach to the surface via focal adhesions. While focal adhesions occur throughout the cell, traction force microscopy indicates that the focal adhesions exert the largest stresses at the edges of a crawling cell on surfaces [134]. We assume that the same observation holds for cells crawling in confined constrictions. Bead 1, denoted by position $x_1(t)$, is to the right of Bead 2, denoted by $x_2(t)$ as shown in Fig. 5.1. The beads have masses m_1 and m_2 , and friction coefficients γ_1 and γ_2 respectively. The friction coefficients model the focal adhesions, or attachment to the fiber, while the active spring in-between the two beads denotes the stress fibers. Let us now quantify the concept of an active spring.

5.1.1 Stress fibers as active springs with two equilibrium lengths

Stress fibers primarily consist of actin filaments, myosin, and alpha-actinin, a passive cross-linker [126]. A few other proteins, such as zyxin, colocalizes with alpha-actinin [135]. The stress fiber is made up of parallel arrangements of actomyosin units in series. Each actomyosin unit is considered as two actin filament rods connected by

a myosin minifilament and alpha-actinin at each end. Since the stress fibers in cells crawling in constrained geometries exhibit more ordered stress fibers than the cells crawling on surfaces, using this fundamental muscle-like element is very useful [136]. See Figure 5.2. For a static cell, the stress fiber is under contractile tension as it adheres to the substrate. In a moving cell, the focal adhesions are being created and destroyed. Since myosin exhibit catch bond behaviour with an optimum load force of about 6 pN per motor, the myosin may not always be under sufficient load (or too much load) to walk efficiently along the actin filaments [137].

More specifically, when focal adhesions are just beginning to form at the front of the cell, myosin are not pulling due to the small applied load. And when myosin are not pulling, the plus end of actin filaments separate/extend. We argue that the plus ends extend to relieve the strain in the alpha-actinin such that it approaches its equilibrium configuration. See Figure 5.2. In this alpha-actinin extension mode, the mechanical stiffness of the active spring, k , is primarily due to the stiffness of the alpha-actinin. Moreover, the equilibrium spring length of the active spring is denoted by x_{eq1} . As the focal adhesions at the front of the cell mature over a time scale of seconds [138], the myosin come under load again such that they “catch” and exert contractile forces on each pair of actin filaments to induce a contracted mode causing the alpha-actinin to stretch and rotate in the opposite direction. In this mode, myosin provide the mechanical stiffness of the spring and there is a second equilibrium spring length, $x_{eq1} - x_{eq2}$, with $x_{eq2} < x_{eq1}$ as indicated by the isolated stress fiber experiments [127].

How then does the stress fiber switch back the extension mode? As the myosin contract, strain builds in the alpha-actinin. This strain build-up can be enhanced by zyxin binding to the alpha-actinin such that the myosin no longer “catch” and a transition is then made to the extending mode. Experiments tracking zyxin in static cells find that it colocalizes to places along the stress fiber under high tension and have argued that zyxin could act as some molecular switch from one mechanical state

to another [139].

Given these two modes of the stress fiber, passive extension and active (motor) contraction, *we model the elasticity of the stress fiber as a spring with two different equilibrium spring lengths.* The transition between the two modes of the active spring is determined by the extension of the spring. The larger the extension of the spring, the more tensile load on the myosin so as to induce contractility of the myosin. Therefore, a simple model for the equilibrium spring length, x_{eq} , of this active spring is

$$x_{eq} = x_{eq1} - x_{eq2}\Theta(x_1 - x_2 - l), \quad (5.1)$$

where $\Theta(x_1 - x_2 - l)$ is the Heaviside step function. See Figure 5.3. With this choice, when $x_1 - x_2 > l$, the equilibrium spring length is shorter when myosin actively pull and longer when the myosin do not. Moreover, l is bounded below by $x_{eq1} - x_{eq2}$ and above by x_{eq1} . With this changing equilibrium spring length, the spring is now an active contractile element.

In addition to the catch-bond kinetics of the acto-myosin bonds, alpha-actinin exhibits catch-bond kinetics as well [140]. Catch-bond kinetics indicate some sort of conformational change in the protein such that the conformation of the alpha-actinin in the extended mode may indeed be different than when in the contracting mode. The binding of zxyin may also affect the conformation of the alpha-actinin. A possible change in conformation of the alpha-actinin suggests that the transition between extension and contraction is not necessarily reversible, particularly if zxyin bind in one conformation (but not the other) [139]. Moreover, when the active spring is in its extended mode, there is less overlap between the actin filaments such that it is less likely that additional alpha-actinin can bind together two actin filaments. Conversely, when the active spring is in its contracted state, it is more likely that an additional alpha-actinin can link two actin filaments together. Therefore, for the active spring to extend, it must overcome the additional binding energy of the added alpha-actinin, i.e. bonds must be broken. However, this additional binding energy is

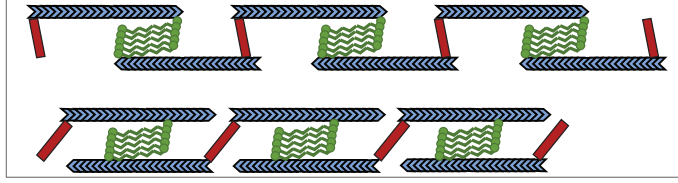


Figure 5.2: Schematic of contractile units in a stress fiber in extended mode (top) and contracted mode (bottom). The blue filaments represent actin filaments, red rectangles, alpha-actinin, and the green shapes, myosin minifilaments. For simplicity, we have not shown any contractile units in parallel, only three units in series.

not present as the active spring contracts.

To account for potential conformational changes in the alpha-actinin, additional alpha-actinin binding, and even internal frictional losses, we allow l to take on two values, l^\uparrow , as the active spring extends and l^\downarrow as the active spring compresses with $l^\uparrow > l^\downarrow$. In sum, the equilibrium active spring length takes on the form,

$$x_{eq} = x_{eq1} - x_{eq2}\Theta(x_1 - x_2 - l^\uparrow), \quad (5.2)$$

when the active spring is extending and

$$x_{eq} = x_{eq1} - x_{eq2}\Theta(x_1 - x_2 - l^\downarrow), \quad (5.3)$$

when the active spring is contracting. This means that the description for x_{eq} contains *hysteresis*. Such hysteresis in stress-strain behavior is often found in materials where the strain history affects the observed stress giving rise to different stress-strain paths for loading and unloading. Prime examples are the phenomenological Johnson-Segalman model of viscoelastic behavior [141], and the experimentally observed strain history dependent mechanical response of soft biological tissue [142]. We must also point out that a recent viscoelastic model for stress fibers is an active version of an viscoelastic polymer model [143]. Because the width of the hysteresis represents a strain barrier and the height a strain “input”, the height of the hysteresis loop must be greater than the hysteresis width to generate motion.

5.1.2 Focal adhesions provide an elastic friction

Now that we have quantified our active spring, we turn to the focal adhesions. The mechanical interaction between the migrating cell and the ECM are mediated by cell surface receptors and associated ligands in the ECM. The ECM glycoprotein fibronectin and the transmembrane receptor proteins of the integrin family, form the major and most well-characterized receptor-ligand pair [144]. In their inactive state, integrins exist in a bent, relaxed form so as to avoid the formation of physiologically harmful cell-cell or cell-ECM connections. Once they are activated via a vertical load, they undergo a conformational change to an extended state [129, 145]. When in this state, AFM experiments find that integrins respond additionally to an increase in the lateral distance between the two extended dimers with an increased bond lifetimes for applied forces up to 30 pN [129]. In other words, integrin can act as a catch bond. It may indeed be the maturation of the focal adhesion that triggers this lateral distance and, thereby, the catch bond mechanism of the integrins [145].

In light of these findings, we conjecture that in the front of the cell, integrins are more likely to act as catch bonds due to maturation of focal adhesions. In the back of the cell, however, integrin act as typical slip bonds, where focal adhesions are merely being disassembled. Therefore, in the front of the cell, the initiation of focal adhesions call for a “small” friction coefficient, but once the focal adhesion forms and develops, it has a large friction coefficient when compared to an integrin slip bond. This “catching” mechanism of cell-track adhesion allows the cell’s front to expand and explore new territory and after having done that, then allows for the cell’s rear to retract with the cell front not losing grip on the new territory it just explored due to the catch bond mechanism. Since the stress fibers and the focal adhesions are connected, we define

$$\gamma_1 = \gamma_{11} + \gamma_{12}\Theta(x_1 - x_2 - l^{\uparrow(l)}) \quad (5.4)$$

with $\gamma_{11}, \gamma_{12} > 0$ and $\gamma_{11} < \gamma_{12}$. For small extensions of the cell, the friction at the

leading bead is smaller than for large extensions. Larger friction implies a larger unbinding rate for integrins and, therefore, the integrins can more effectively grip the track. In addition, because the integrins track the myosin activity, the hysteresis exhibited by the myosin is also exhibited in the friction. See Figure 5.3. Finally, γ_2 , the friction coefficient for the now “rear” bead, is assumed to be constant with the integrins acting as ordinary slip bonds.

5.1.3 Equations of motion

With the stress fibers modeled as an active spring with spring constant, k , and a changing equilibrium spring length, and the focal adhesions localized at the front and the back beads of the two bead-active spring model, the two coupled equations for the motion of the beads are as follows:

$$m_i \ddot{x}_i(t) + \gamma_i(x_1, x_2, l^\uparrow, l^\downarrow) \dot{x}_i(t) = \pm k(x_1 - x_2 - x_{eq}(x_1, x_2, l^\uparrow, l^\downarrow)) + \sqrt{A_i} \zeta_i(t). \quad (5.5)$$

Note that we have included an “active noise” term, where A_i is the variance of the active noise contribution due to stochasticity in motor activity, and $\zeta_i(t)$ is a Gaussian random variable with $\langle \zeta_i(t) \rangle = 0$ and $\langle \zeta_i(t) \zeta_j(t') \rangle = \delta_{ij} \delta(t - t')$. Here, A_i does not satisfy a fluctuation-dissipation relation and is not associated with any temperature. We will study this model for both $A_i = 0$ (deterministic) and $A_i > 0$ (non-deterministic).

5.2 Estimation of parameters

Now that we have the formal solutions for the relative and center-of-mass coordinates, let us present estimates for the parameters involved before analyzing the solutions in further detail.

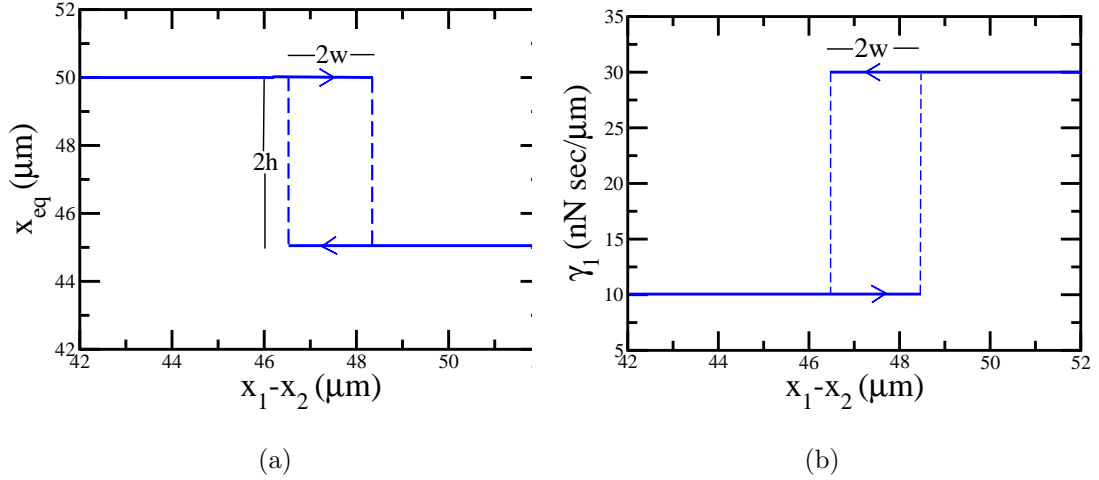


Figure 5.3: Left (a): Plot of the equilibrium spring length x_{eq} as a function of $x_1 - x_2$. Right (b): Plot of friction coefficient γ_1 as a function of $x_1 - x_2$. The parameters used are listed in Table I.

5.2.1 Active spring parameters

The actomyosin units account for both the passive mechanical stiffness and the active contractile properties of the stress fiber. The stiffness of the myosin minifilament is represented by a spring of stiffness $N_m k_m$, where N_m is the number of myosin motors in the minifilament and k_m is the spring constant for each individual myosin with $k_m \approx 1$ $p\text{N}/\text{nm}$ (1 $p\text{N}/\text{nm} = 1$ $\text{nN}/\mu\text{m}$) and $N_m \approx 50$ [146]. For $N_m \approx 50$, the typical length of a myosin minifilament is 0.3 μm , while its width is approximately 30 nm [147], which is also consistent with the approximate length of alpha-actinin. Each motor exerts equal and opposite contractile forces on the two actin filaments, denoted each by f , on the two actin filaments. Each myosin motor head can exert a maximum of $f/2 = 3$ $p\text{N}$ of contractile force [148]. The actin filaments are modeled as rigid filaments with the pair of spanning a maximum length L . Typically, $L = 1$ μm . Each alpha-actinin is modeled as a linear spring with spring constant, $k_0 \approx 50$ $p\text{N}/\text{nm}$ and rest length L_a that can change due to potential conformational changes in the alpha-actinin between the extending and contracting modes of the actomyosin units [149].

As mentioned previously, experiments on isolated stress fibers find up to a 23 percent decrease in length with the addition of ATP [127]. In the extended mode, we use an equilibrium spring length, $x_{1eq} = 50$ microns since stress fibers typically consist of about 50 actomyosin units in series and each of the units span a maximum of 1 micron [150]. Given the experimental results for percentage of decrease in length of the stress fiber due to myosin contractility, we will explore a range of percentages around 10 percent.

With the above ingredients, we can also estimate the effective stiffness of the stress fiber active-spring as follows. The effective stiffness of a myosin minifilament consisting of $N_m \approx 50$ myosin motors, each with a myosin spring constant approximately 1 pN/nm in parallel, is 50 pN/nm . In the extended mode of the active spring, the alpha-actinin contributes to the elasticity, in the contracted mode, the myosin minifilaments contribute to the stress fiber elasticity. This leads to a spring stiffness of $\sim 50 \text{ pN/nm}$ for either mode for each unit such that $k = 50 \text{ pN/nm} (N_p/N_s)$, where N_s is the number of acto-myosin contractile units in series and N_p in parallel. With $N_s = 50$ and $N_p = 1$, $k \approx 1 \text{ pN/nm}$. For $N_p > 1$, the effective stress fiber spring constant is larger.

5.2.2 Friction parameters

We model the integrins as springs with dissociation kinetics described by catch or slip bond behavior. Each integrin bond can be thought of as a single Hookean spring and allowed to fail at one point at the cell-ECM interface. At the back of the cell, the unbinding kinetics of the integrin bond will follow slip bond behavior with an effective dissociation rate, K_{off}^* , that increases exponentially according to a Bell Model [131], or

$$K_{off}^* = K_{off} e^{F_{bond}/F_b} \quad (5.6)$$

where K_{off} is the unforced dissociation rate of the slip bond, $F_b = k_B T / \psi$ is the characteristic bond rupture force and ψ is a characteristic unbinding lengthscale, and F_{bond} is the tension within an individual slip bond spring. Hence, the slip bond lifetime simply decreases with increasing applied tensile force.

For the front bead, the integrin bond acts as a catch bond in the presence of developing focal adhesions and the dissociation kinetics is a sum of two pathways—one where the bond is strengthened by the applied force and other where it is weakened. The summative unbinding rate can be written as follows:

$$K_{off}^* = K_s e^{F_{bond}/F_b} + K_c e^{-F_{bond}/F_b} \quad (5.7)$$

where, the unforced unbinding rates $K_s = K_{off} e^{-F_s/F_b}$ and $K_c = K_{off} e^{F_c/F_b}$ are each associated with each pathway [151].

Once K_{off} is known, the friction coefficients can be computed using using the formula,

$$\gamma = \frac{N_{int} k_{int}}{K_{off}^*}, \quad (5.8)$$

where N_{int} is the number of bound integrins and k_{int} is the spring constant of the molecular bond. We use $k_{int} \approx 10 \text{ pN/nm}$ and $N_{int} \approx 1$, though we will explore other values. Since integrins form the bond between the cell and the substrate, we use the kinetic curve obtained from Kong and collaborators for the lifetime of a single bond as a function of applied load [129]. For the front bead, we use $K_{off}^* = 1 \text{ s}^{-1}$ to compute $\gamma_{11} = 10 \text{ nN s}/\mu\text{m}$, the weaker coefficient, and an off-rate of 1/3 inverse seconds for the stronger value of the friction coefficient of the front bead, leading to $\gamma_{12} = 20 \text{ nN s}/\mu\text{m}$. Then, $\gamma_{11} + \gamma_{12} = 30 \text{ nN s}/\mu\text{m}$. For the back bead, $K_c = 0$ and we use $K_{off}^* = 0.5 \text{ s}^{-1}$ to arrive at $\gamma_2 = 20 \text{ nN s}/\mu\text{m}$.

Parameters	Values
k	1 nN/ μ m
x_{eq1}	50 μ m
x_{eq2}	5 μ m
l^\downarrow	\sim 46.5 μ m
l^\uparrow	\sim 48.5 μ m
γ_{11}	10 nN s/ μ m
γ_{12}	20 nN s/ μ m
γ_2	20 nN s/ μ m
m_1, m_2	\sim 0
A_1, A_2	\sim 0

Table 5.1: Table of parameters used.

5.3 Results

To solve the equations of motion, (Eq. 5.5), we neglect inertia, as demanded by the physiological conditions. We then first investigate the cell crawler in the absence of any noise such that $A_1 = A_2 = 0$. Next, defining $x = x_1 - x_2$ and subtracting the equation of motion for x_2 from x_1 , we arrive at

$$\dot{x} = -\left(\frac{1}{\gamma_1(x, l^{\uparrow(\downarrow)})} + \frac{1}{\gamma_2}\right)k(x - x_{eq}(x, l^{\uparrow(\downarrow)})), \quad (5.9)$$

depending on whether the spring is extending or compressing. Similarly, the equation of motion for the center of mass is

$$v_{cm}(t) = \dot{x}_{cm} = -\frac{1}{2}\left(\frac{1}{\gamma_1(x, l^{\uparrow(\downarrow)})} - \frac{1}{\gamma_2}\right)k(x - x_{eq}(x, l^{\uparrow(\downarrow)})), \quad (5.10)$$

where $x_{cm} = \frac{x_1 + x_2}{2}$. A non-zero center of mass velocity translates to motion of the cell.

Since the center of mass velocity equation depends on x , we first solve the equation of motion for x . To do so, we break up the system into when the equilibrium spring

length is x_{eq1} and when the equilibrium spring length is $x_{eq1} - x_{eq2}$. In the former case,

$$x_I(t) = x_{eq1} + (x(0) - x_{eq1})e^{-\frac{k}{\gamma_2} \frac{(\gamma_{11} + \gamma_2)}{(\gamma_{11})} t}, \quad (5.11)$$

and in the latter,

$$x_{II}(t) = x_{eq1} - x_{eq2} + (x(0) - x_{eq1} + x_{eq2})e^{-\frac{k}{\gamma_2} \frac{(\gamma_{11} + \gamma_{12} + \gamma_2)}{(\gamma_{11} + \gamma_{12})} t}. \quad (5.12)$$

Now, depending on the history of the spring, be it contracting or extending, we can piece together these solutions accordingly. For example, assume $x(0) \geq l^\uparrow$, then x decreases and obeys $x_{II}(t)$, which decreases exponentially with time. This is because the cell has “over-extended itself” in its search for new territory and now the focal adhesions have matured so both the equilibrium spring length is decreased, due to myosin-induced contractility, and the front catch bonds “catch” such that the back of the cell can catch up with the front without losing new ground. After the initial decrease in x , as soon as x decreases below l^\downarrow , then the myosin effectively stop pulling, due to strain built up in the stress fibers from the focal adhesions and alpha-actinin, and the equilibrium spring length increases with new focal adhesions developing at the front. Once this happens, we re-zero our time clock back to $t = 0$ and iterate $x_I(t)$, an exponential expansion given the initial condition, until x becomes larger than l^\uparrow such that $x_{II}(t)$ solutions become valid and the process repeats itself. As we will see below, this cyclic process in an overdamped system leads to net motion due to (1) the switching between the two equilibrium spring constants, which drives the overdamped system out-of-equilibrium, and (2) the asymmetry in the friction coefficients. Both properties are needed for motion.

Let us analyze the active dimer motion as a function of the width and height of the hysteresis loop. Defining $w = \frac{1}{2}(l^\uparrow - l^\downarrow)$ and $h = \frac{1}{2}x_{eq2}$, the two timescales over which the cell undergoes extension and contraction are given by $t_I = \beta \log \frac{h+w}{h-w}$ and $t_{II} = \alpha \log \frac{h+w}{h-w}$ respectively, where $\alpha = \gamma_2(\gamma_{11} + \gamma_{12})/k(\gamma_{11} + \gamma_{12} + \gamma_2)$ and $\beta = \gamma_2\gamma_{11}/k(\gamma_{11} + \gamma_2)$. As stated earlier, $w < h$ for motion to occur since the active

strain energy generated by the myosin must overcome the strain barrier by the alpha-actinin. When the active dimer is extending to relieve the strain in the alpha-actinin and $x > l^\downarrow$, the maximum and minimum values of the center of mass velocity are

$$\begin{aligned} v_{cm,max,I} &= \frac{k}{2} \left(\frac{1}{\gamma_{11}} - \frac{1}{\gamma_2} \right) (h + w) \\ v_{cm,min,I} &= \frac{k}{2} \left(\frac{1}{\gamma_{11}} - \frac{1}{\gamma_2} \right) (h - w). \end{aligned} \quad (5.13)$$

Similarly, when the dimer is contracting, and $x < l^\uparrow$, the maximum and minimum values of the center of mass velocity are given by

$$\begin{aligned} v_{cm,max,II} &= \frac{-k}{2} \left(\frac{1}{\gamma_{11} + \gamma_{12}} - \frac{1}{\gamma_2} \right) (h + w) \\ v_{cm,min,II} &= \frac{-k}{2} \left(\frac{1}{\gamma_{11} + \gamma_{12}} - \frac{1}{\gamma_2} \right) (h - w). \end{aligned} \quad (5.14)$$

Finally, the time-averaged-over-one-period v_{cm} , or \bar{v}_{cm} , is given by

$$\bar{v}_{cm} = \frac{t_I \bar{v}_{cm,I} + t_{II} \bar{v}_{cm,II}}{t_I + t_{II}}, \quad (5.15)$$

where

$$\bar{v}_{cm,I} = \frac{(\gamma_2 - \gamma_{11})}{2t_I(\gamma_{11} + \gamma_2)} (x_I(0) - x_{eq1}) \left(e^{-\frac{k}{\gamma_2} \frac{\gamma_{11} + \gamma_2}{\gamma_{11}} t_I} - 1 \right), \quad (5.16)$$

and

$$\bar{v}_{cm,II} = \frac{(\gamma_2 - (\gamma_{11} + \gamma_{12}))}{2t_{II}(\gamma_{11} + \gamma_{12} + \gamma_2)} (x_{II}(0) - (x_{eq1} - x_{eq2})) \left(e^{-\frac{k}{\gamma_2} \frac{\gamma_{11} + \gamma_{12} + \gamma_2}{\gamma_{11} + \gamma_{12}} t_{II}} - 1 \right). \quad (5.17)$$

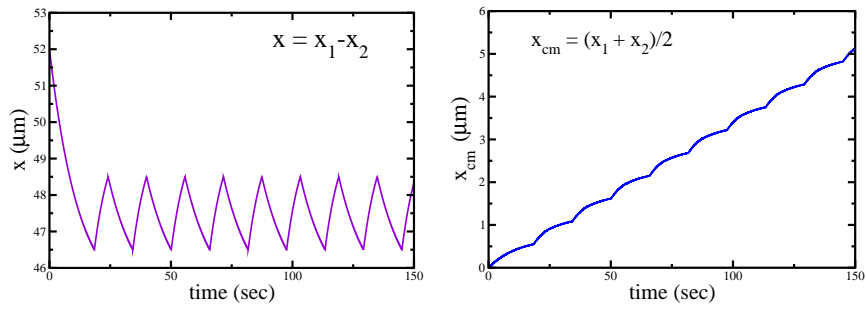
The time-averaged-over-one-period v_{cm} would presumably be the simplest measurement an experimentalist could perform. So we will study it in detail.

Using our parameter estimates from Sec. III, we first present results for $x_{rel}(t)$, $x_{cm}(t)$, and $v_{cm}(t)$. See Figure 5.4. Apart for the initial cycle, for each subsequent cycle, the time in the extension mode is 5.65 s and the time in the contraction mode is 10.17 s. Note that the time scale for the extension mode, which corresponds to the timescale for focal adhesion maturation, is in agreement with the observed timescale of seconds for focal adhesion maturation [138]. We find $v_{cm,max,I} = 0.088 \mu\text{m/s}$,

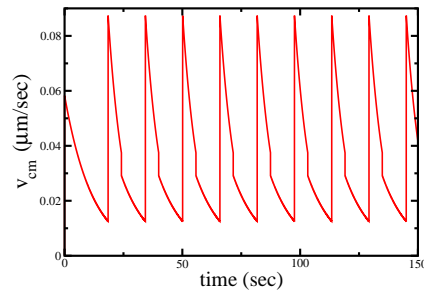
$v_{cm,min,I} = 0.038 \mu m/s$, $v_{cm,max,II} = 0.029 \mu m/s$, and $v_{cm,min,II} = 0.013 \mu m/s$. The time-averaged-center-of-mass-velocity is $\bar{v}_{cm} = 0.033 \mu m/s$. This value is in reasonable agreement with the order-of-magnitude time-averaged velocity for wild-type HT-1080 fibrosarcoma cells crawling in the ECM [152]. Of course, we have not yet taken into account the elasticity of the collagen fiber(s) such that we expect our result to be an upper bound on the speed. Interestingly, the maximum instantaneous velocity of the center of mass is the same order as keratocytes crawling on surfaces [42]. The time-averaged velocity of the center of mass is about an order of magnitude smaller. So, using physiologically based independent estimates for the parameters involved we obtain reasonable cell speeds for cells traveling in the ECM.

How does \bar{v}_{cm} vary with the spring parameters, namely, k , h , and w ? In Figures 5.5 and 5.6, we plot both \bar{v}_{cm} and $x_{cm}(t)$ for several values of these parameters. As indicated by Eqns (5.15)-(5.17), \bar{v}_{cm} increases linearly with the spring constant k . On the other hand, increasing the width of the hysteresis loop, w , decreases \bar{v}_{cm} since there is a larger strain barrier to overcome to elongate. Once the strain barrier becomes equal to or larger than the added strain energy (due to myosin pulling, for example), i.e. $w > h$, then the active cell can longer move effectively. Moreover, increasing the difference between the two equilibrium spring lengths (increasing h), adds more active strain energy into the system with the motors contracting more effectively such that the active dimer can crawl faster until the speed becomes limited by the asymmetry in the friction coefficients. An increase in h can be driven by the addition of myosin (in the contraction mode) or increasing the spring constant associated with the alpha-actinin since the extension mode is driven by releasing strain in the alpha-actinin (as opposed to actin growth).

As stated previously, it is the combination of the nonequilibrium nature of the active spring and the asymmetry of the friction that leads to motion. We have added this asymmetry explicitly given the molecular understanding of how the integrins behave as catch bonds as focal adhesions mature. In the absence of this asymmetry,



(a)



(c)

Figure 5.4: (a) Plot of cell length $x = x_1 - x_2$ as a function of time for the parameters given in Table I. (b) Plot of position of the center of mass, x_{cm} , as a function of time. (c) Plot of velocity of the center of mass, v_{cm} , as a function of time.

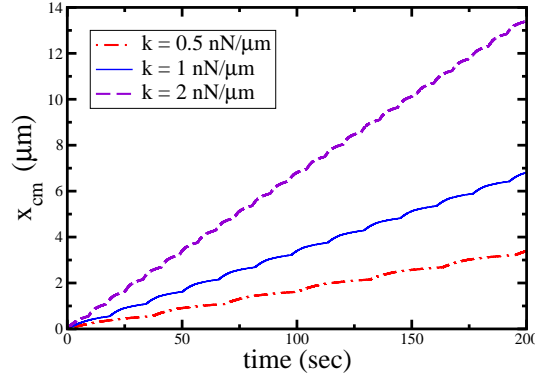


Figure 5.5: Left: Plot of center of mass for cell as a function of time for different spring constants k . The parameters are from Table I (unless stated otherwise).

i.e. $\gamma_{11} + \gamma_{12} = \gamma_2$ with $\gamma_{12} = 0$, then $v_{I,II,cm} = 0$. Moreover, if $\gamma_{12} = 0$, then $\bar{v}_{cm} = 0$ (even for $\gamma_2 \neq \gamma_{11}$) because any new territory gained during the extension mode will be lost during the contraction mode. See Figure 5.7. Moreover, in breaking the symmetry, we have made a choice as to which direction the active dimer crawls. The cell can change direction when $\gamma_{11} > \gamma_2$ and $\gamma_{12} < 0$. Since motion of the center of mass in the extension mode is now to the left, as long as the asymmetry in the friction coefficients in the contraction mode is such that not all new territory gain is lost, then there is net motion to the left. We also observe that as the difference between γ_{11} and γ_2 increases, \bar{v}_{cm} also increases. This increase allows the extension mode of the active dimer to be more efficient at exploring new territory and increases \bar{v}_{cm} (provided $\gamma_{12} \neq 0$ to model the catch bond behavior of the integrin at the front of the cell). See Figure 5.7.

Now let us investigate the motion of the active dimer when nonequilibrium noise ($A_i > 0$) is turned on? Is the motion robust? Why ask this? Well, the cell is very much a dynamic entity. There is mounting evidence that the motion of objects placed in a cell, such as a carbon nanotube, couples to myosin-driven stress fluctuations in the cytoskeleton [153]. These fluctuations are reminiscent of thermal noise, but with a nonthermal origin. To study the effect of noise on our crawling cell, we simulate

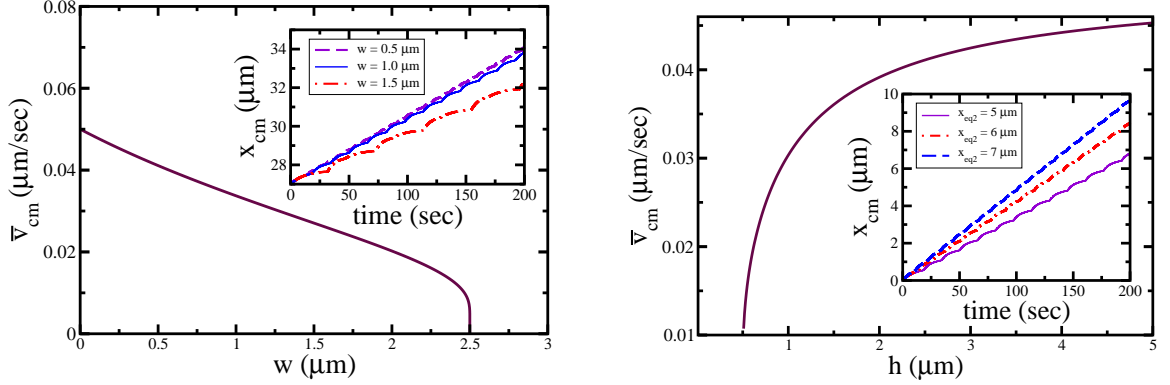


Figure 5.6: Left: Plot of $\bar{v}_{cm}(w)$. Left Inset: Plot of $x_{cm}(t)$ for different widths. Right: Plot of $\bar{v}_{cm}(h)$ for $w = 0.5$ μm . Right Inset: Plot of $x_{cm}(t)$ for different heights of hysteresis loop.

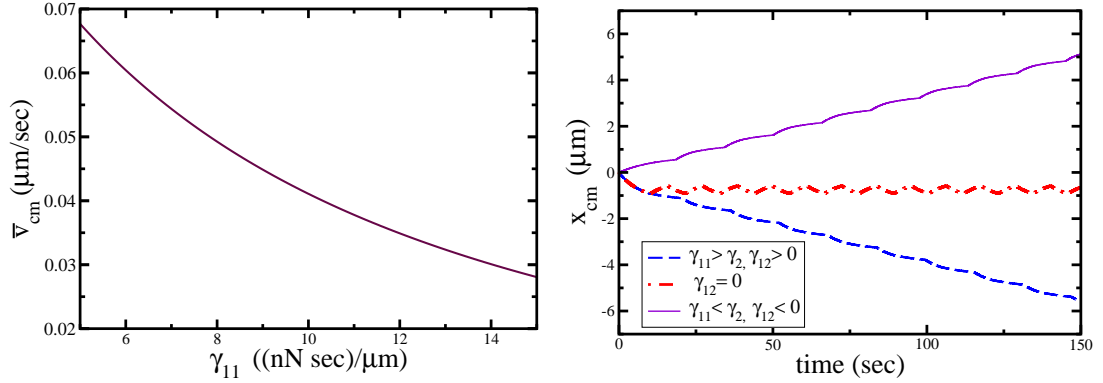


Figure 5.7: Left: Plot of $x_{cm}(t)$ for different friction coefficients. Right: Plot of $\bar{v}_{cm}(\gamma_{11})$.

the equations of motion using the Euler-Maruyama scheme with $A_i > 0$ [154]. We define $A = A_1 = A_2$.

Given our deterministic active dimer, for small enough values of A , the noise can be added perturbatively and should not affect the cyclic behavior of the active dimer. More precisely, we find that for $A < 0.1$ $\text{nN}^2 \text{s}$, the noise does not affect the motion of the cell with the cyclic behavior between the extension and contraction modes remaining on average (See Figure 5.8). However, as A is increased beyond 0.1, $\text{nN}^2 \text{s}$, the scallops become washed out on average, though the average speed of the cell

remains virtually unchanged. One can estimate the upper bound of this crossover. When the cell is in the extension mode, for instance, the variance, $\sigma_I(t)$, is given by $\sigma_I(t) = \langle x_I^2(t) \rangle - \langle x_I(t) \rangle^2 = \frac{A(\gamma_{11} + \gamma_2)}{k\gamma_2\gamma_{11}}(1 - e^{-\frac{2k(\gamma_2 + \gamma_{11})t}{\gamma_2\gamma_{11}}})$. When $\sqrt{\sigma_I(t)}$ becomes of order the hysteresis width in the timescale t_I (to use as a first approximation), then the area of the deterministic hysteresis gets washed out on average. This upper bound corresponds approximately to $A \approx 10 \text{ nN}^2\text{s}$, which is a bit larger than the observed value. One can improve upon this upper bound by taking into account the directionality of the hysteresis loop and determine the average time scale that the velocity of the relative coordinate goes from positive to negative (a velocity zero-crossing). This is because a velocity zero-crossing can drive the active dimer from one mode to the other. One can impose a threshold on the noise for this switching to occur. We leave such modifications for potential future work. What we have learned, however, is that the deterministic model for the model cell is robust to a range of nonequilibrium, or active, noise. The upper limit of this range maps to an effective diffusion constant of a

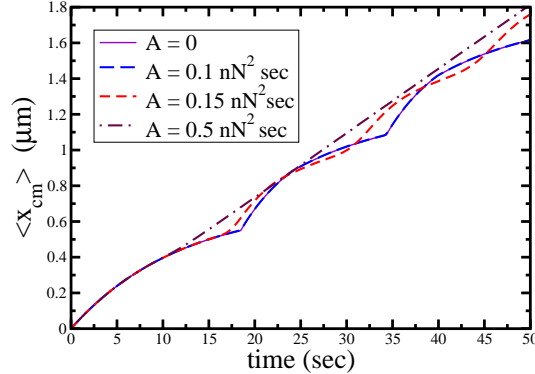


Figure 5.8: Plot of $x_{cm}(t)$ for different values of the noise with $A = A_1 = A_2$.

Finally, we ask the following question: How does the motion of the active dimer change if the hysteresis loops contain finite slopes? Then, in going from one mode to the other, the stress fiber would no longer behave as a switch, but the change in equilibrium spring length would depend continuously on the strain. Since the integrals

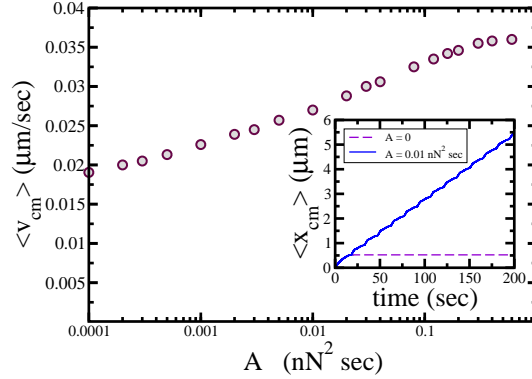


Figure 5.9: Plot of $\langle v_{cm} \rangle (A)$ for finite slope case with a slope of $5/2$. Inset: Plot of $\langle x_{cm} \rangle (t)$ for $A = 0$ and $A = 0.01 nN^2 s$.

are ultimately coupled to the stress fibers, changes in the friction coefficients would also depend continuously on the strain. Well, as long as curves with finite slope intersect with the $x = x_{eq}$, as is the case with our model, then motion will cease since this is an overdamped system now in equilibrium. See Figure 5.9. However, the addition of active noise kicks the dimer out of equilibrium and motion resumes. If the active noise is sufficient to change the direction of the strain (extending to compressing, for example), there is a switch from one equilibrium spring constant to the other. A threshold on this switch will require an active noise strength above this threshold to regain motion. Furthermore, at least for $A_1 = A_2$, as the strength of the active noise increases, so does the average velocity of the center-of-mass, or $\langle v_{cm} \rangle$, though the increasing the active noise strength by an order of magnitude eads to a gain of a few tenths of a percent. In sum, for this finite slope case, active noise is crucial for sustainable net motion.

5.4 Discussion

We have constructed a minimal model for cell moving on a rigid fiber. The model contains two beads and one spring, the beads representing the front and the back of

the cell respectively. Friction coefficients for each bead represent the focal adhesions between the substrate and the cell. We assume the back bead to have constant friction, while the front bead friction changes as nascent focal adhesions become mature focal adhesions to grip the surface via their catch bond behavior. In addition, the single spring connecting the front and the back beads models the basal stress fibers stretching along the cell. The effect of myosin is modeled by a change of the equilibrium spring length. When myosin is actively contracting, the equilibrium spring length is shorter than when myosin is not. We have emphasized that the extension mode is driven by relieving strain in alpha-actinin binding, which could be enhanced due to zyxin binding to alpha-actinin, when the myosin unbind. Both the catch bond behavior and/or dynamics of alpha-actinin may give rise to hysteresis in this active contractility, which we have incorporated into the model.

We find that the activity of the myosin and the asymmetry in the friction coefficients due to catch bond behavior of the integrins at the front of the cell and slip bond behavior at the back are both needed to obtain directed motion of the crawling cell in an overdamped system in the absence of any noise. Like Refs. [155] and [156], our model does not require actin-filament nucleation driven by the branching agent Arp2/3 for cell motility. This is important for elongated cells crawling along ECM fibers where Arp2/3 plays a role in generating pseudopods to potentially explore new ECM fibers, but does not drive motility [133]. In contrast to Ref. [155], where an advection-diffusion equation for the motor concentration coupled with an active contractile stress drives the motion, our model takes into account the stress fiber structure and the interaction with the substrate via focal adhesion friction. In contrast to Ref. [156], our model is deterministic and observes motion in the direction of larger friction (at least for some part of the cycle), which is in keeping with experiments [134].

Using independent estimates for the parameters in the model, we find reasonable agreement with observed speeds of elongated cells crawling along ECM fibers [152].

We also study the average speed as a function of the parameters, which can presumably be qualitatively explored, at least, via knockdowns of the proteins involved or via mutants. For instance, the larger the difference between the two equilibrium spring lengths, the faster the average cell speed. A larger difference could be due to more myosin (to enhance the contraction mode), or more alpha-actinin (to enhance the extension mode). Interestingly, increased expression levels of alpha-actinin are found in melanomas and in tumor cell lines with faster migration rates (than the corresponding healthy cells) [157]. We also find that the net deterministic cell motion is robust to active noise. For the time being, we varied the parameters of the model independently and studied the time-averaged center-of-mass velocity, or speed. However, varying some of the parameters simultaneously may yield an optimal speed.

Our model may help understand the finding of oscillations observed in cells that are lacking in the protein zyxin. More specifically, recent experiments [152] have found that zyxin-depleted cells migrating in the ECM move persistently along highly linear tracks before reversing their direction. This reversal persists resulting in oscillations. These oscillations have also been observed in cells moving on one-dimensional micro-patterned substrates, but not in two dimensions. Such periodic migration has been shown to result from the coupling between cell shape and actin-polymerization driven polarity in phase-field models of cell migration [158]. While protrusive stresses generated by actin filament nucleation via Arp2/3 (and subsequent polymerization) at the leading edge of the cell play a key role in two-dimensional cell migration, it is less dominant in three-dimensional migration. Our model does not require actin filament nucleation and may provide further insight into the underlying mechanism for the above periodic migratory motion in the one and three dimensions. Should zyxin be knocked down, then the switching behavior in our active spring between contraction and extension may become compromised over time (with redundant proteins not as efficient as zyxin) and the cell will eventually not be able to move. Hence, it will fluidize, reorient itself, and begin to crawl in another direction to search out

new space. In the one-dimensional case, the cell can only reverse its direction to search out “new” space.

One important advantage of our minimal model is that its simplicity easily allows for extension. For instance, we can (1) introduce Arp2/3 generated pseudopods via extra beads and active springs (2) incorporate elasticity into the track, (3) introduce a cell nucleus via extra beads and active springs, and (4) scale up to many cells interacting via cadherins. As for adding elasticity to the track, the motility of cells migrating in the ECM depends on its microstructure [5-17]. What are, then, the strategies or optimization principles that cells use to migrate in the ECM such that they can harness the elasticity of the ECM fibers to move, while also overcoming the physical barriers to motion imposed by the matrix architecture? We can begin to answer such questions by coupling our model cell to an extensible worm-like polymer and probe the cell’s motility. As for introducing a cell nucleus, the discovery of actin stress fibers extending over the nucleus [159] such that as the cell crawls the nucleus is squeezed in the direction transverse to crawling [160], begs for study via modeling. We can add these actin cap stress fibers to our basal stress fiber model and address whether their presence helps speed up or slow down a cell crawling along a one-dimensional elastic fiber. And, finally, the extension to interacting active elastic dimers is motivated by recent experiments on a collection of spindle-shaped NIH-3T3 cells at high densities [161]. Given the geometry of such cells, their mechanism for motion may indeed be similar to one described here. This begs the question, under what conditions does the cell motion *not* rely on actin-filament nucleation and polymerization, other than the constrained geometry case of crawling along ECM fibers? Confinement by other cells, potentially of a different type, may indeed be another possibility.

Chapter 6

Future directions

The jamming graph is a useful mathematical object that enables one to study the connectivity of a purely repulsive particle packing at the rigidity transition. We were able to show two different scenarios when a jamming graph becomes flexible by deleting just one edge. In one case the result was many small rigid clusters and in the other case very few small rigid clusters emerged. We naturally conclude that there is a set of critical edges whose removal produces many rigid components. It would be interesting to have a characterization of such critical edges. It would also be interesting to impose positive weights on the jamming graph to represent forces (once redundant bonds are added) and ask about the interplay between connectivity and forces given some dynamical rules for the breaking and forming of contacts. It is also possible to assign to each vertex in the jamming graph a disk of appropriate radius by means of the circle packing theorem [86]. By using both force assignments to the edges of the graph and disk assignments to the vertices, one can approach more accurately the complexity of the problem.

The study of constraint percolation models on hyperbolic lattices allowed us to deduce that k -core percolation for $k = 1, 2$, and 3 demonstrate similar behavior in the sense that all of them exhibit the three phases of ordinary percolation in this type of geometry: there are no percolating clusters for low values of the occupation

probability p , several percolating clusters for a probability between two critical values, and one "big" percolation cluster for probabilities higher than those two critical probability values. This conclusion is inferred from the behavior of the crossing probability. For the case of counter balance percolation, it seems there is just the usual two percolation phases, no percolating cluster for occupation probability less than a threshold value and one percolating cluster for occupation probabilities higher than this value. The code for generating hyperbolic tessellations is, in general, useful to analyze other physical problems. For example, we could study the jamming graphs that are set on a hyperbolic geometry. This would allow us to interpolate away from Euclidean lattices and study the effect of loops on rigidity. Arguments have been made as to the loopless nature of the jamming transition, i.e. the jamming system acts if it were on a Bethe lattice (a mean field system). It would be interesting to better understand how this property comes about.

The finding of glassy dynamics for cell migration in confluent tissues may have all sorts of consequences for cell sorting. Cells are the basic structural and functional units of living matter (beyond the micron scale), so understanding the ability of different types of cell to sort and form organs and tissues is an important problem. Chapter 5 is, in some ways, complementary to Chapter 4 in that it models single cell motion and the interaction with the substrate, as opposed to cell-cell interaction. It would be interesting to combine some of the details at the level of various proteins developed in Chapter 5 with the collective cell model studied in Chapter 4 to arrive at a more comprehensive theory of cell migration.

Bibliography

- [1] R. K. Pathria. *Statistical Mechanics*. Elsevier, New York, 2nd revised edition, 1996.
- [2] J. Zhang, T. Majmudar, and R. Behringer. Force chains in a two-dimensional granular pure shear experiment. *Chaos*, **18**:041107, 2008.
- [3] S. F. Edwards. The full canonical ensemble for a granular system. *Physica A*, **353**:114–118, 2005.
- [4] D. J. Durian. Foam mechanics at the bubble scale. *Phys. Rev. Lett.*, **75**:4780–4783, 1995.
- [5] C. S. O’Hern, S. A. Langer, A. J. Liu, and S. R. Nagel. Random packings of frictionless particles. *Phys. Rev. Lett.*, **88**:075507, 2002.
- [6] C. S. O’Hern, L. E. Silbert, A. J. Liu, and S. R. Nagel. Jamming at zero temperature and zero applied stress: The epitome of disorder. *Phys. Rev. E*, **68**:011306, 2003.
- [7] H. J. Hertz. Ueber die berührung fester elastischer körper. *J. Reine Ang. Math.*, **92**:156–171, 1881.
- [8] D. J. Durian. Bubble-scale model of foam mechanics: Melting, nonlinear behavior, and avalanches. *Phys. Rev. E*, **55**:1739, 1997.

- [9] A. J. Liu, M. Wyart, W. van Saarloos, and S. R. Nagel. The jamming scenario – an introduction and outlook. In L. Berthier, G. Biroli, J.-P. Bouchaud, L. Cipeletti, and W. van Saarloos, editors, *Dynamical heterogeneities in glasses, colloids, and granular media*, pages 298–336. Oxford University Press, Oxford, 2010.
- [10] M. van Hecke. Jamming of soft particles: geometry, mechanics, scaling, and isostaticity. *J. Phys. Cond. Matt.*, **22**:033101, 2010.
- [11] A. J. Liu and S. R. Nagel. The jamming transition and the marginally jammed solid. *Annu. Rev. Condens. Matter Phys.*, **1**:347, 2010.
- [12] C. F. Schreck, B. T. Thibault, C. S. O’Hern, and M. D. Shattuck. Repulsive contact interactions make jammed particulate systems inherently nonharmonic. *Phys. Rev. Lett.*, **107**:078301–1–078301–4, 2011.
- [13] C. P. Goodrich, A. J. Liu, and S. R. Nagel. Comment on repulsive contact interactions make jammed particulate systems inherently nonharmonic. *Phys. Rev. Lett.*, **112**:049801–1–049801–4, 2014.
- [14] J. C. Maxwell. On the calculation of the equilibrium and stiffness of frames. *Philos. Mag.*, **27**:294, 1864.
- [15] G. Laman. On graphs and rigidity of plane skeletal structures. *J. Engrg. Math.*, **4**:331, 1979.
- [16] D. J. Jacobs and B. Hendrickson. An algorithm for two-dimensional rigidity percolation: The pebble game. *J. Comp. Phys.*, **137**:346, 1997.
- [17] J. H. Lopez and J. M. Schwarz. Constraint percolation on hyperbolic lattices (in preparation). 2014.
- [18] D. Stauffer and A. Aharony. *Introduction To Percolation Theory*. Taylor and Francis, 2nd revised edition, 2003.

- [19] P. J. Flory. *Principles of Polymer Chemistry*. Cornell University Press, New York, 1953.
- [20] J. M. Schwarz, A. J. Liu, and L. Q. Chayes. The onset of jamming as the sudden emergence of an infinite k -core cluster. *Europhys. Lett.*, **73**:560–566, 2006.
- [21] M. C. Medeiros and C. M. Chaves. Universality in bootstrap and diffusion percolation. *Physica A*, **234**:604–610, 1997.
- [22] N. S. Branco and C. J. Silva. Universality class for bootstrap percolation with $m = 3$ on the cubic lattice. *Int. J. Mod. Phys. C*, **10**:921–930, 1999.
- [23] M. Aizenman and J. L. Lebowitz. Metastability effects in bootstrap percolation. *J. Phys. A: Math. Gen.*, **21**:3801–3813, 1988.
- [24] F. Klein. Uber die sogenannte nicht-euklidische geometrie. *Math. Ann.*, **4**:573–625, 1871.
- [25] F. Sausset, G. Tarjus, and P. Viot. Thermodynamics and structure of simple liquids in the hyperbolic plane. *J. Stat. Mech.*, **88**:P04022, 2009.
- [26] S. K. Baek, H. Makela, P. Minnhagen, and B. J. Kim. Ising model on a hyperbolic plane with a boundary. *Phys. Rev. E*, **84**:032103, 2011.
- [27] M. D. Ediger. Spatially heterogeneous dynamics in supercooled liquids. *Annual Review of Physical Chemistry*, **51**(1):99–128, 2000. PMID: 11031277.
- [28] A. J. Liu and S. R. Nagel. Jamming is just not cool anymore. *Nature*, **396**:21–22, 1998.
- [29] F. Ritort and R. Sollich. Glassy dynamics of kinetically constrained models. *Adv. Phys.*, **52**:219–243, 2003.

- [30] R. Candelier, O. Dauchot, and G. Biroli. The building blocks of dynamical heterogeneities in dense granular media. *Phys. Rev. Lett.*, **102**:088001–1–088001–4, 2009.
- [31] E. R. Weeks, J. C. Crocker, A. C. Levitt, A. Schofield, and D. A. Weitz. Three-dimensional direct imaging of structural relaxation near the colloidal glass transition. *Science*, **287**:627–630, 2000.
- [32] P. G. Debenedetti and F. H. Stillinger. Supercooled liquids and the glass transition. *Nature*, **410**(6825):259–267, 03 2001.
- [33] C. Monthus and J.-P. Bouchaud. Models of traps and glass phenomenology. *J. Phys. A: Math. Gen.*, **29**(14):3847, 1996.
- [34] Peter Sollich. Rheological constitutive equation for a model of soft glassy materials. *Phys. Rev. E*, 58:738–759, Jul 1998.
- [35] Thomas E. Angelini, Edouard Hannezo, Xavier Trepap, Manuel Marquez, Jeffrey J. Fredberg, and David A. Weitz. Glass-like dynamics of collective cell migration. *Proceedings of the National Academy of Sciences*, 108(12):4714–4719, 2011.
- [36] D. N. Kenechukwu, M. Knorr, J. Käs, and M. Zink. The impact of jamming on boundaries of collectively moving weak-interacting cells. *New J. Phys.*, **14**(11):115012, 2012.
- [37] E.-M. Schötz, M. Lanio, J. A. Talbot, and M. L. Manning. Glassy dynamics in three-dimensional embryonic tissues. *J. Roy. Soc. Inter.*, **10**(89):11, 12 2013.
- [38] C. Guillot and T. Lecuit. Mechanics of epithelial tissue homeostasis and morphogenesis. *Science*, **340**(6137):1185–1189, 06 2013.

- [39] Dapeng Bi, Jorge H. Lopez, J. M. Schwarz, and M. Lisa Manning. Energy barriers and cell migration in densely packed tissues. *Soft Matter*, **10**:1885, 2014.
- [40] D. Bi, J. H. Lopez, J. M. Schwarz, and M. L. Manning. *unpublished*, 2014.
- [41] A. Mogilner. Cell motility: Have we got its number? *J. Math. Biol.*, **58**:105–134, 2009.
- [42] K. Keren, Z. Pincus, G. M. Allen, E. L. Barnhart, G. Marriott, A. Mogilner, and J. A. Theriot. Mechanism of shape determination in motile cells. *Nature*, **453**:475–480, 2008.
- [43] R. J. Petrie, N. Gavara, R. S. Chadwick, and K. M. Yamada. Nonpolarized signaling reveals two distinct modes of 3d cell migration. *J. Cell Biol.*, **197**(3):439–455, 04 2012.
- [44] T. M. Svitkina, A. B. Verkhovsky, K. M. McQuade, and G. G. Borisy. Analysis of the actin-myosin ii system in fish epidermal keratocytes: Mechanism of cell body translocation. *J. Cell Biol.*, **139**:397, 1997.
- [45] N. Ofer, A. Mogilner, and K. Keren. Actin disassembly clock determines shape and speed of lamellipodial fragments. *Proc. Natl. Acad. Sci. USA*, **108**:20394, 2011.
- [46] H. N. Higgs and T. D. Pollard. Regulation of actin filament formation through arp2/3 complex. *Annu. Rev. Biochem.*, **70**:649, 2001.
- [47] J. H. Lopez, Moumita Das, and J. M. Schwarz. Active elastic dimers: Cells moving on rigid tracks. page under review, 2014.
- [48] S. Alexander. Amorphous solids: Their structure, lattice dynamics, and elasticity. *Phys. Repts.*, **296**:65–236, 1998.

- [49] M. Wyart, S. R. Nagel, and T. A. Witten. Geometric origin of excess low-frequency vibrational modes in weakly connected amorphous solids. *Eur. Phys. Lett.*, **72**:486, 2005.
- [50] M. Wyart, L. E. Silbert, S. R. Nagel, and T. A. Witten. Effects of compression on the vibrational modes of marginally jammed solids. *Phys. Rev. E*, **72**:051306, 2005.
- [51] P. Goodrich, W. G. Ellenbroek, and A. J. Liu. Stability of jammed packings i: the rigidity length scale. *Soft Matter*, **9**:10993–10999, 2013.
- [52] M. Mailman and B. Chakraborty. A signature of a thermodynamic phase transition in jammed granular packings: Growing correlations in force space. *J. Stat. Mech.*, **2011**:L07002, 2011.
- [53] M. Mailman and B. Chakraborty. Using point-to-set correlations to probe unjamming of frictionless grains. *J. Stat. Mech.*, **2012**:P05001, 2012.
- [54] B. Tighe. Floppiness, cutting, and freezing: Dynamic critical scaling near isotaticity. *Phys. Rev. Lett.*, **109**:168303, 2012.
- [55] W. G. Ellenbroek, E. Somfai, M. van Hecke, and W. van Saarloos. Critical scaling in linear response of frictionless granular packings near jamming. *Phys. Rev. Lett.*, **97**:258001, 2006.
- [56] W. G. Ellenbroek, M. van Hecke, and W. van Saarloos. Jammed frictionless disks: Connecting local and global response. *Phys. Rev. E*, **80**:061307, 2009.
- [57] G. During, E. Lerner, and M. Wyart. Phonon gap and localization length in floppy materials. *Soft Matter*, **9**:146, 2012.
- [58] H.-K. Janssen and U. C. Tauber. The field theory approach to percolation processes. *Ann. Phys.*, **147**:147, 2005.

- [59] M. F. Thorpe. Continuous deformation in random network. *J. Non-Cryst. Solids*, **57**:355, 1983.
- [60] S. Feng and P. N. Sen. Percolation on elastic networks: new exponent and threshold. *Phys. Rev. Lett.*, **52**:214, 1984.
- [61] S. Feng, M. F. Thorpe, and E. Garboczi. Effective-medium theory of percolation on central-force elastic networks. *Phys. Rev. B*, **31**:276, 1985.
- [62] D. J. Jacobs and M. F. Thorpe. Generic rigidity percolation: The pebble game. *Phys. Rev. Lett.*, **75**:4051, 1995.
- [63] D. J. Jacobs and M. F. Thorpe. Generic rigidity percolation in two dimensions. *Phys. Rev. E*, **76**:041135, 2007.
- [64] C. Moukarzel and P. M. Duxbury. Stressed backbone and elasticity of random central-force systems. *Phys. Rev. Lett.*, **75**:4051, 1995.
- [65] L. Henneberg. Die graphische statik der stratten systeme. *Manuscript*, 1911.
- [66] I. Streinu and L. Theran. Sparse hypergraphs and pebble game algorithms. *Eur. J. Comb.*, **30**:1944, 2009.
- [67] G. Berg, W. Julian, R. Mines, and F. Richman. The constructive jordan curve theorem. *Rocky Mount. J. Math.*, **5**:225, 1975.
- [68] A. V. Tkachenko and T. A. Witten. Stress propagation through frictionless granular material. *Phys. Rev. E*, **60**:687, 1999.
- [69] L. Silbert, D. Ertas, G. S. Grest, T. C. Halsey, and D. Levine. Geometry of frictionless and frictional sphere packings. *Phys. Rev. E*, **65**:031304, 2002.
- [70] P. Olsson and S. Teitel. Critical scaling of shear viscosity at the jamming transition. *Phys. Rev. Lett.*, **99**:178001, 2007.

- [71] A. Donev, F. H. Stillinger, and S. Torquato. Calculating the free energy of nearly jammed hard-particle packings using molecular dynamics. *J. Comp. Phys.*, **225**:509, 2007.
- [72] P. Chaudhuri, L. Berthier, and S. Sastry. Jamming transitions in amorphous packings of frictionless spheres occur over a continuous range of volume fractions. *Phys. Rev. Lett.*, **104**:165701, 2010.
- [73] D. Vagberg, P. Olsson, and S. Teitel. Glassiness, rigidity, and jamming of frictionless soft core disks. *Phys. Rev. E*, **83**:30303(R), 2011.
- [74] S. Dagois-Bohy, B. P. Tighe, and J. Simon. Soft sphere packings at finite pressure but unstable to shear. *Phys. Rev. Lett.*, **109**:095703, 2012.
- [75] C. Moukarzel. An efficient algorithm for testing the generic rigidity of graphs in the plane. *J. Phys. A: Math. Gen.*, **29**:8079, 1996.
- [76] C. Moukarzel. Elastic collapse in disordered isostatic networks. *Europhys. Lett.*, **97**:36008, 2012.
- [77] W. G. Ellenbroek, Z. Zeravcic, W. van Saarloos, and M. van Hecke. Non-affine response: Jammed packings vs. spring networks. *Europhys. Lett.*, **87**:34004, 2009.
- [78] This Example Was Pointed Out to Us by Brigitte Servatius.
- [79] E. Lerner, G. During, and M. Wyart. Low-energy non-linear excitations in sphere packings. *Soft Matter*, **9**:8252–8263, 2013.
- [80] C. Goodrich, A. J. Liu, and S. R. Nagel. Finite-size scaling at the jamming transition. *Phys. Rev. Lett.*, **109**:095704 (4 pp.), 2012.
- [81] M. Wyart. Scaling of phononic transport with connectivity in amorphous solids. *Europhys. Lett.*, **89**:64001, 2010.

- [82] S. Torquato, T. M. Truskett, and P. G. Debenedetti. Is random close packing of spheres well defined? *Phys. Rev. Lett.*, **84**:2064, 2000.
- [83] G. Parisi and F. Zamponi. Mean field theory of hard sphere glasses and jamming. *Rev. Mod. Phys.*, **82**:789, 2010.
- [84] P. Charbonneau, E. I. Corwin G. Parisi, and F. Zamponi. Universal microstructure and mechanical stability of jammed packings. *Phys. Rev. Lett.*, **109**:205501, 2012.
- [85] J. D. Bernal and J. Mason. Packing of spheres: Co-ordination of randomly packed spheres. *Nature*, **188**:910, 1960.
- [86] Kenneth Stephenson. *Introduction to circle packing*. Cambridge University Press, New York, 2005.
- [87] M. V. Chubynsky and M. F. Thorpe. Algorithms for 3d rigidity analysis and a first order percolation transition. *Phys. Rev. E*, **76**:041135, 2007.
- [88] B. Tighe. Shear dilatancy in marginal solids. 2013. arXiv:1305.5574.
- [89] A. R. T. van Eerd, W. G. Ellenbroek, M. van Hecke, J. H. Snoeijer, and T. J. H. Vlugt. Tail of the contact force distribution in static granular materials. *Phys. Rev. E*, **75**:060302(R), 2007.
- [90] B. P. Tighe, A. R. T. van Eerd, and T. J. H. Vlugt. Entropy maximization in the force network ensemble for granular solids. *Phys. Rev. Lett.*, **100**:238001, 2008.
- [91] S.-L.-Y. Xu, X. Illa, and J. M. Schwarz. Force network analysis of jammed solids. 2010. arXiv:1008.4568.
- [92] S. Henkes and B. Chakraborty. Jamming as a critical phenomenon: A field theory of zero-temperature grain packings. *Phys. Rev. Lett.*, **95**:198002, 2005.

- [93] H. Jacquin, L. Berthier, and F. Zamponi. A microscopic mean-field theory of the jamming transition. *Phys. Rev. Lett.*, **106**:135702 (4 pp.), 2011.
- [94] M. Jeng and J. M. Schwarz. On the study on force-balance percolation. *Phys. Rev. E*, **81**:011134, 2010.
- [95] M. Mailman, C. F. Schreck, B. Chakraborty, and C. S. O'Hern. Jamming in systems composed of frictionless ellipse-shaped particles. *Phys. Rev. Lett.*, **102**:255501, 2009.
- [96] Z. Zeravcic, N. Xu, A. J. Liu, and S. R. Nagel. Excitations of ellipsoid packings near jamming. *Europhys. Lett.*, **87**:26001, 2009.
- [97] S. Henkes, Y. Fily, D. Quint, and J. M. Schwarz. Frictional jamming and the 3,3 pebble game (in preparation). 2014.
- [98] F. Sausset and G. Tarjus. Periodic boundary conditions on the pseudosphere. *J. Phys. A: Mathematical and Theoretical*, **40**:12873, 2007.
- [99] D. Dunham. Hyperbolic symmetry. *Comp. Maths. with Appls.*, **12**:139–153, 1986.
- [100] H. Gu and R. M. Ziff. Crossing on hyperbolic lattices. *Phys. Rev. E* **85**, **85**:051141, 2012.
- [101] S. S. Manna. Abelian cascade dynamics in bootstrap percolation. *Physica A: Stat. Mech. Appls.*, **261**:351–358, 1998.
- [102] S. K. Baek, P. Minnhagen, and B. J. Kim. Percolation on hyperbolic lattices. *Phys. Rev. E*, **79**:011124, 2009.
- [103] I. Benjamini and O. Schramm. Percolation in the hyperbolic plane. *J. Amer. Math. Soc.*, **14**:487–507, 2000.

- [104] H. G. Othmer, S. R. Dunbar, and W. Alt. Models of dispersal in biological systems. *J. Math. Biol.*, **26**:263–298, 1988.
- [105] S. A. Langer and A. J. Liu. Sheared foam as a supercooled liquid? *Europhys. Lett.*, **49**(1):68, 2000.
- [106] M. L. Manning and A. J. Liu. Vibrational modes identify soft spots in a sheared disordered packing. *Phys. Rev. Lett.*, **107**:108302, Aug 2011.
- [107] D. B. Staple, R. Farhadifar, J. C. Roper, S. Eaton B. Aigouy, and J. F. Julicher. Mechanics and remodelling of cell packings in epithelia. *Eur. Phys. J. E*, **33**:117–127, 2010.
- [108] Reza Farhadifar, Jens-Christian Roper, Benoit Aigouy, Suzanne Eaton, and Frank Julicher. The influence of cell mechanics, cell-cell interactions, and proliferation on epithelial packing. *Current Biology*, 17(24):2095 – 2104, 2007.
- [109] L. Hufnagel, A. A. Teleman, H. Rouault, S. M. Cohen, and B. I. Shraiman. On the mechanism of wing size determination in fly development. *Proc. Natl. Acad. Sci. USA*, **104**(10):3835–3840, March 2007.
- [110] S. Hilgenfeldt, S. Erisken, and R. W. Carthew. Physical modeling of cell geometric order in an epithelial tissue. *Proc. Natl. Acad. Sci. USA*, **105**(3):907–911, Jan 14 2008.
- [111] M. L. Manning, R. A. Foty, M. S. Steinberg, and E.-M. Schoetz. Coaction of intercellular adhesion and cortical tension specifies tissue surface tension. *Proc. Natl. Acad. Sci. USA*, **107**(28):12517–12522, 07 2010.
- [112] S. Henkes, Y. Fily, and M. C. Marchetti. Active jamming: Self-propelled soft particles at high density. *Phys. Rev. E*, **84**:040301, Oct 2011.
- [113] L. Berthier. Nonequilibrium glassy dynamics of self-propelled hard disks, 2013.

- [114] M. Basan, T. Risler, J.-F. Joanny, X. Sastre-Garau, and J. Prost. Homeostatic competition drives tumor growth and metastasis nucleation. *HFSP J.*, **3**(4):265, Jan 1 2009.
- [115] E.-M. Schoetz, R. D. Burdine, F. Julicher, M. S. Steinberg, C.-P. Heisenberg, and R. A. Foty. Quantitative differences in tissue surface tension influence zebrafish germlayer positioning. *HFSP journal*, Vol.2 (1):1–56, 2008.
- [116] Kenneth A Brakke. The surface evolver. *Experimental mathematics*, 1(2):141–165, 1992.
- [117] S. E Cross, Y.-S. Jin, J. Tondre, R. Wong, J.-Y. Rao, and J. K. Gimzewski. Afn-based analysis of human metastatic cancer cells. *Nanotechnology*, **19**:384003, 2008.
- [118] J. C. M. Mombach, D. Robert, F. Graner, G. Gillet, G. L. Thomas, M. Idiart, and J. P. Rieu. Rounding of aggregates of biological cells: Experiments and simulations. *Physica A: Stat. Mech. App.*, **352**(2-4):525–534, 2005.
- [119] L Hufnagel, AA Teleman, H Rouault, SM Cohen, and BI Shraiman. On the mechanism of wing size determination in fly development. *Proceedings of the National Academy of Sciences*, **104**:3835–3840, 2007.
- [120] B. Alberts, A. Johnson, J. Lewis, M. raff, K. Roberts, and P. Walter. *Molecular Biology of the Cell*. Garland, New York, 5th edition, 2007.
- [121] D. Bray. *Cell Movements*. Garland, New York, 200o.
- [122] K. Wolf, S. Alexander, V. Schacht, L. M Coussens, U. H. von Andrian, J. van Rheenen, E. Deryugine, and P. Friedl. Collagen-based cell migration models in vitro and in vivo. *Seminars in Cell and Developmental Biology*, **20**:931–941, 2009.

- [123] A. D. Doyle, R. J. Petrie, M. Kutys, L. Matthew, and K. M. Yamada. Dimensions in cell migration. *Curr. Opin. Cell Biol.*, **25**:642–649, 2013.
- [124] A. Pathak and S. Kumar. Transforming potential and matrix stiffness co-regulate confinement sensitivity of tumor cell migration. *Integr. Biol.*, **5**:1067, 2013.
- [125] M. Mak, C. A. Reinhart-King, and D. Erickson. Microfabricated physical spatial gradients for investigating cell migration and invasion dynamics. *PLoS ONE*, DOI: 10.1371/journal.pone.0020825, 2011.
- [126] S. Tojkander, G. Gateva, and P. Lappalainen. Actin stress fibers: Assembly, dynamics and biological roles. *J. Cell Sci.*, **125**:1855–64, 2012.
- [127] K. Katoh. Isolation and contraction of the stress fiber. *Mol. Biol. Cell*, **9**:1919–38, 1998.
- [128] P. Kanchanawong, G. Shtengel, A. M. Pasapera, E. B. Ramko, M. W. Davidson, H. F. Hess, and C. M. Waterman. Nanoscale architecture of integrin-based cell adhesions. *Nature*, **468**:580, 2010.
- [129] F. Kong, A. J. Garcia, A. P. Mould, M. J. Humphries, and C. Zhu. Demonstration of catch bonds between an integrin and its ligand. *J Cell Biol.*, **185**:1275, 2009.
- [130] M. Dembo, D. C. Torney, K. Saxman, and D. Hammer. The reaction-limited kinetics of membrane-to-surface adhesion and detachment. *Proc. Royal Soc. London*, **234**:55, 1988.
- [131] G. Bell. Models for the specific adhesion of cells to cells. *Science*, **200**:618, 1978.

- [132] T. M. Svitkina and G. G. Borisy. Arp2/3 complex and actin depolymerizing factor/cofilin in dendritic organization and treadmilling of actin filament array in lamellipodia. *J. Cell Biol.*, **145**:1009, 1999.
- [133] A. Giri, S. Bajpai, N. Trenton, H. Jayatilaka, G. D. Longmore, and D. Wirtz. The arp2/3 complex mediates multigeneration dendritic protrusions for efficient 3-dimensional cancer cell migration. *FASEB J.*, **27**:4089, 2013.
- [134] M. Dembo and Y.-L. Wang. Stresses at the cell-to-substrate interface during locomotion of fibroblasts. *Biophys. J.*, **76**:2307, 1999.
- [135] M. A Smith, E. Blankman, M. L. Gardel, L. Luettjohann, C. M. Waterman, and M. C. Beckerle. A zyxin-mediated mechanism for actin stress fiber maintenance and repair. *Dev. Cell*, **14**:365, 2010.
- [136] P. Friedl, K. S. Zanker, and E. B. Brocker. Cell migration strategies in 3-d extracellular matrix: differences in morphology, cell matrix interactions, and integrin function. *Micro. Res. Tech.*, **43**:369–78, 1998.
- [137] B. Guo and W. H. Guilford. Mechanics of actomyosin bonds in different nucleotide states are tuned to muscle contraction. *Proc. Natl. Acad. Sci. USA*, **103**:9844, 2006.
- [138] Y. Chen, A. M. Pasapera, A. P. Koretsky, and C. M. Waterman. Orientation-specific responses to sustained uniaxial stretching in focal adhesion growth and turnover. *Proc. Natl. Acad. Sci. USA*, **110**:2352, 2013.
- [139] J. Colombelli. Mechanosensing in actin stress fibers revealed by a close correlation between force and protein localization. *J. Cell Sci.*, **122**:1665, 2009.
- [140] N. Y. Yao. Stress-enhanced gelation: A dynamic nonlinearity of elasticity. *Phys. Rev. Lett.*, **110**:018103, 2013.

- [141] M. Johnson and D. Segalman. A model for viscoelastic fluid behavior which allows non-affine deformation. *J. Non-Newt. Fl. Mech*, **2**:255-270, 1977.
- [142] S. Munster, L. M. Jawerth, B. A. Leslie, J. I. Weitz, B. Fabry, and D. A. Weitz. Strain history dependence of the nonlinear stress response of fibrin and collagen networks. *Proc. Natl. Acad. Sci. USA*, **110**:12197, 2013.
- [143] A. Besser, J. Colombelli, E. H. K. Stelzer, and U. S. Schwarz. Viscoelastic response of contractile filament bundles. *Phys. Rev. E*, **83**:051902, 2011.
- [144] S. Miyamoto, B. Z. Katz, L. B. Lafrenie, and K. M. Yamada. Fibronectin and integrins in cell adhesion, signaling, and morphogenesis. *Annals of the New York Academy of Sciences*, **857**:119-29, 1998.
- [145] J. C. Friedland, M. H. Lee, and D. Boettiger. Mechanically activated integrin switch controls alpha5beta1 function. *Science*, **323**:642, 2009.
- [146] T. Thorsen, M. Lenz, and M. L. Gardel. Thick filament length and isoform composition determine self-organized contractile units in actomyosin bundles. *Biophys. J.*, **104**:655, 2013.
- [147] R. Neiderman and T. D. Pollard. Human platelet myosin. ii. in vitro assembly and structure of myosin filaments. *J. Cell Biol*, **67**:72-92, 1975.
- [148] J. Howard. *Mechanics of Motor Proteins and the Cytoskeleton*. Sinauer Associates, New York, 2001.
- [149] M. Soncini. Mechanical response and conformational changes of alpha-actinin domains during unfolding: a molecular dynamics study. *Biomechan. Model Mechanobiol.*, **6**:399, 2007.
- [150] S. Deguchi, T. Ohashi, and M. Sato. Tensile properties of single stress fibers isolated from cultured smooth muscle cells. *J. Biomech.*, **39**:2603, 2006.

- [151] E. A. Novikova and C. Storm. Contractile fibers and catch-bond clusters: a biological force sensor. *Biophys. J*, **105**:1336, 2013.
- [152] S. I. Fraley, Y. Feng, A. Giri, G. D. Longmore, and D. Wirtz. Dimensional and temporal controls of three-dimensional cell migration by zyxin and binding partners. *Nat. Comm.*, **3**:719, 2012.
- [153] N. Fakhri. High-resolution mapping of intracellular fluctuations using carbon nanotubes. *Science*, **344**:1031, 2014.
- [154] E. Kloden, E. Platen, , and H. Schurz. *Numerical Solution of SDE through Computer Experiments*. Springer-Verlag, Berlin-Heidelberg, 1994.
- [155] P. Recho, T. Putelat, , and L. Truskinovsky. Contraction-driven cell motility. *Phys. Rev. Lett.*, **111**:108102, 2013.
- [156] K. V. Kumar, S. Ramaswamy, and M. Rao. Active elastic dimers: Self-propulsion and current reversal on a featureless track. *Phys. Rev. E*, **77**:020102, 2008.
- [157] R. Vadlamudi, L. Adam, B. Tseng, L. Costa, and R. Kumar. Transcriptional up-regulation of paxillin expression by heregulin in human breast cancer cells. *Cancer Res.*, **59**:2843, 1999.
- [158] B. A. Camley, Y. Zhao, B. Li, H. Levine, and W.-J. Rappel. Periodic migration in a physical model of cells on micropatterns. *Phys. Rev. Lett.*, **111**:158102, 2013.
- [159] S. B. Khatau, C. M. Hale, P. J. Stewart-Hutchinson, M. S. Patel, C. L. Stewart, P. C. Searson, D. Hodzic, and D. Wirtz. A perinuclear actin cap regulates nuclear shape. *Proc. Natl. Acad. Sci.*, **106**:19017, 2009.
- [160] S. B. Khatau, R. J. Bloom, S. Bajpai, D. Razafsky, S. Zang, A. Giri, P.-H. Wu, J. Marchand, A. Celedon, C. M. Hale, S. X. Sun, D. Hodzic, and D. Wirtz.

The distinct roles of the nucleus and nucleus-cytoskeleton connections in three-dimensional cell migration. *Sci. Reps.*, **2**:1038, 2012.

- [161] G. Duclos, S. Garcia, H. G. Yevick, and P. Silberzan. Perfect nematic order in confined monolayers of spindle-shaped cells. *Soft. Matt.*, **10**:2346, 2014.

Curriculum Vitae

Jorge Hernan Lopez

815 Comstock Av, Syracuse, New York, 13210

Cell: (315) 863-4712

Email: jhlopez@syr.edu

Education

- Ph.D., Physics, Syracuse University, 2014.

Area: Condensed Matter Theory

Thesis: “Aspects of Rigidity and Plasticity in Living and Nonliving Matter”

- Master, Physics, Syracuse University, 2010
- Master, Matematicas, Universidad Nacional de Colombia, 2007

Thesis: “Aplicaciones de los grupos de Lie a las ecuaciones diferenciales”

- Bachelor, Fisica, Universidad de Antioquia, 2003

Thesis: “Análisis numérico de las ecuaciones de Kukhtarev para el régimen de difusión y baja modulación en un cristal BSO”

Honours and Merits

Levinstein Fellowship, Syracuse University, June 2014

Member of Phi Beta Delta International Honor Society, 2011

Young researcher, Optics group, Universidad de Antioquia, 2003

Young researcher, Solid state group, Universidad de Antioquia, 2001

Participant in Final round in National Mathematics Olympiad, Colombia, 1996

Participant in Final round in National Physics Olympiad, Colombia, 1996

Publications

Jorge H. Lopez, L. Cao, and J. M. Schwarz. *Jamming graphs: A local approach to global mechanical rigidity*. Phys. Rev. E **88**, 062130. Dec. 2013; arXiv: 1306.4639

Dapeng Bi, J. H. Lopez, J. M. Schwarz, M. Lisa Manning. *Energy barriers and cell migration in densely packed tissues*. Soft Matter, 2014, **10**, 1885-1890; arXiv: 1308.3891

Aplicaciones del Efecto Fotorrefractivo. Universitas Cientifica de la Universidad Pontificia Bolivariana. ISSN 1692-0155.

Under Review

J. H. Lopez, Moumita Das, and J. M. Schwarz. *Active elastic dimers: Cells moving on rigid tracks*. 2014.

In Preparation

Dapeng Bi, J. H. Lopez, J. M. Schwarz, M. Lisa Manning. *Collective cell migration in tissues: the role of energy barriers to rearrangements*. 2014.

Jorge H. Lopez, and J. M. Schwarz. *Constraint percolation on hyperbolic lattices*. 2014.

Presentations

March Meeting, 2014. *A model for cell crawling in 3D*.

March Meeting, 2013. *On the local construction of jamming graphs*.

March Meeting, 2012. *Constraint percolation on hyperbolic lattices*.

XX Congreso nacional de Fisica de Colombia. Analisis Numerico de las ecuaciones de Kukhtarev.

Skills

Programming in languages: C, C++, Surface Evolver, Visual Molecular Dynamics (VMD), Python, Mathematica, Matlab.

Fluent in English and Spanish.

Teaching Experience

Teaching Assistantship in Syracuse University for the period 2009-2014 in the courses: Our Corner of the Universe (AST101), Stars, Galaxies & the Universe (AST104), Major Concepts of Physics (PHY101), General Physics I (PHY211), General Physics II (PHY212), General Physics II Laboratory (PHY222).

Partial time professor in Universidad Pontificia Bolivariana, Medellin, Colombia. In the period 2006-2008 for courses: Euclidean and Vectorial geometry, Introduction to calculus, Fundamentals of Electromagnetism, Geometry and Trigonometry.

Partial time professor in Universidad de Antioquia, Medellin, Colombia. In 2005 for Physics III and Introduction to Physics. In 2008-2009 for Physics II and Physics III.

Partial time professor in Universidad Nacional, Medellin, Colombia. In the period 2004-2006 for the courses: Mathematics I, Vectorial Geometry, Differential equations, and Lab for Physics I.

References

Jennifer Schwarz, Assistant Professor, Physics Department, Syracuse University.
<http://physics.syr.edu/~jschwarz/jmspeople.html>

Moumita Das, Assistant Professor, College of Science, Rochester Institute of Technology. <http://www.rit.edu/cos/moumita-das>

Dapeng (Max) Bi, Postdoctoral Researcher, Physics Department, Syracuse University. <https://dbi.expressions.syr.edu/>